Reconstruction of Coronary Arteries from X-ray Rotational Angiography

Serkan Çimen

The University Of Sheffield.

A thesis submitted in partial fulfilment of the requirements for the degree of

Doctor of Philosophy (PhD)

Dec, 2016

Reconstruction of Coronary Arteries from X-ray Rotational Angiography

Serkan Çimen

Department of Electronic and Electrical Engineering
The University of Sheffield

Supervisors:
Prof. Alejandro F. Frangi[1]
Prof. Julian P. Gunn[1]
Dr. Ali Gooya[1]

Examiners and Coordinator:
Prof. Andreas Maier[2]
Dr. Xianghua Xie[3]
Dr. Zeike A. Taylor[1]

[1] The University of Sheffield, UK
[2] Friedrich-Alexander-Universität Erlangen-Nürnberg, Germany
[3] Swansea University, UK

A thesis submitted in partial fulfilment of the requirements for the degree of

Doctor of Philosophy (PhD)

Dec, 2016

Abstract

Despite continuous progress in X-ray angiography systems, X-ray coronary angiography is fundamentally limited by its 2D representation of moving coronary arterial trees, which can negatively impact assessment of coronary artery disease and guidance of percutaneous coronary intervention. To provide clinicians with 3D/3D+time information of coronary arteries, methods computing reconstructions of coronary arteries from X-ray angiography are required. Because of several aspects (e.g. cardiac and respiratory motion, type of X-ray system), reconstruction from X-ray coronary angiography has led to vast amount of research and it still remains as a challenging and dynamic research area.

In the first part of this work, we review the state-of-the-art approaches on reconstruction of high-contrast coronary arteries from X-ray angiography. We mainly focus on the theoretical features in model-based (modelling) and tomographic reconstruction of coronary arteries, and discuss the evaluation strategies. We also discuss the potential role of reconstructions in clinical decision making and interventional guidance, and highlight areas for future research.

In the second part, we look into the coronary artery reconstruction problem from a probabilistic perspective, and propose new algorithms for model-based 3D/3D+time reconstruction of coronary arteries. First, we formulate a novel probabilistic model-based centreline reconstruction method based on a Gaussian mixture model. Second, we propose a novel model-based 3D+time coronary artery centreline reconstruction method. The novelty of the method stems from the fact that it employs a spatiotemporal statistical model of the ventricular epicardium to cope with the ill-posedness of the reconstruction problem. Lastly, we extend our probabilistic 3D reconstruction method by using Student's t-distributions, and incorporating spatial regularisation and sparsity priors in a Bayesian framework. Thanks to these improvements, the reconstruction algorithm can handle cardiac motion inconsistencies between X-ray images due to finite gating accuracy, and noisy or erroneously segmented parts in 2D centreline segmentations.

Acknowledgement

I would like to thank my supervisor, Prof. Alejandro F. Frangi, for giving me the opportunity to join his vibrant research group (CISTIB), and providing financial support. Throughout my PhD period, he has always ensured that I am working and collaborating with the correct people. I would also like to thank my second supervisor, Prof. Julian Gunn, for his kindness and support.

In the last two years of my Phd, I was fortunate enough to work with my co-supervisor, Dr. Ali Gooya. His arrival to CISTIB marks a turning point for the course of many PhD theses, including mine. I am grateful for his positive attitude and continuous support in almost any topic.

During my PhD, I had the chance to work closely with very talented colleagues, from whom I have learned a lot. In particular, I would like to thank all co-authors of the papers that was published or are in preparation, Dr. Corné Hoogendoorn, Dr. Michael Grass and Dr. Zeike Taylor, for their detailed reviews and constructive feedback. I also would like to express my sincere gratitude to all the colleagues in CISTIB for creating an enjoyable and supportive working environment. I would like to give special thanks to Nishant Ravikumar, Matthias Lange, Edward Cramphorn, Isaac Castro-Mateos and Rui Hua, for the stimulating discussions and friendly leisure time.

Finally, I thank my parents for their encouragements. And most of all, I owe tremendously to my wife who has endured all the difficulties with me during this journey, and supported me unconditionally.

The author of this thesis was a recipient of PhD scholarship (2012-2015) from the Department of Electronic and Electrical Engineering, The University of Sheffield, UK. This study was partially supported by Wellcome Trust Health Innovation Challenge Fund (grant HICF-R6-365), and by the Marie Curie Individual Fellowship (625745, A. Gooya).

Publications

Articles published in journals and conference proceedings

[1] **S. Çimen**, A. Gooya, N. Ravikumar, Z. A. Taylor, and A. F. Frangi, “Reconstruction of Coronary Artery Centrelines from X-Ray Angiography Using a Mixture of Students t-Distributions,” in *Proc. Med. Image Comput. Comput. Assist. Interv.*, S. Ourselin, L. Joskowicz, M. R. Sabuncu, G. Unal, and W. Wells, Eds., vol. 9902, 2016, pp. 291-299.

[2] **S. Çimen**, A. Gooya, M. Grass, and A. F. Frangi, “Reconstruction of Coronary Arteries from X-ray Angiography: A Review,” *Med. Image Anal.*, vol. 32, pp. 46-68, 2016.

[3] **S. Çimen**, A. Gooya, and A. F. Frangi, “Reconstruction of Coronary Artery Centrelines from X-ray Rotational Angiography using a Probabilistic Mixture Model,” in *Proc. SPIE*, vol. 9784, 2016, pp. 97843A-97843A-7.

[4] **S. Çimen**, C. Hoogendoorn, P. Morris, J. Gunn, and A. F. Frangi, “Reconstruction of Coronary Trees from 3DRA Using a 3D+t Statistical Cardiac Prior,” in *Proc. Med. Image Comput. Comput. Assist. Interv.*, P. Golland, N. Hata, C. Barillot, J. Hornegger, and R. Howe, Eds., vol. 8674, 2014, pp. 619-626.

[5] A. Suinesiaputra, P. Ablin, X. Albà, M. Alessandrini, J. Allen, W. Bai, **S. Çimen**, P. Claes, B. R. Cowan, J. Dhooge, N. Duchateau, J. Ehrhardt, A. F. Frangi, A. Gooya, V. Grau, K. Lekadir, A. Lu, A. Mukhopadhyay, I. Oksuz, N. Parajuli, X. Pennec, M. Pereañez, C. Pinto, P. Piras, M. M. Rohé, D. Rueckert, D. Säring, M. Sermesant, K. Siddiqi, M. Tabassian, L. Teresi, S. A. Tsaftaris, M. Wilms, A. A. Young, X. Zhang, P. Medrano-Gracia, “Statistical Shape Modelling of the Left Ventricle: Myocardial Infarct Classification Challenge,” *IEEE J. Biomed. Heal. Informatics*, 2017.

[6] N. Ravikumar, A. Gooya, **S. Çimen**, A. F. Frangi, and Z. A. Taylor, “A Multi-resolution t-Mixture Model Approach to Robust Group-Wise Alignment of Shapes,” in *Proc. Med. Image Comput. Comput. Assist. Interv.*, S. Ourselin, L. Joskowicz, M. R. Sabuncu, G. Unal, and W. Wells, Eds., vol. 9902, 2016, pp. 142–149.

[7] C. Pinto, **S. Çimen**, A. Gooya, K. Lekadir, and A. F. Frangi, “Joint Clustering and Component Analysis of Spatio-Temporal Shape Patterns in Myocardial Infarction,” in *Proc. Statistical Atlases and Computational Models of the Heart. Imaging and Modelling Challenges: STACOM 2015*, O. Camara, T. Mansi, M. Pop, K. Rhode, M. Sermesant, and A. Young, Eds., vol .9534, 2016, pp. 171-179.

Articles under review

[8] **S. Çimen**, M. Unberath, A. F. Frangi, and A. Maier, "CoronARe: A Coronary Artery Reconstruction Challenge," *(Submitted)*.

Contents

List of Figures

List of Tables

Chapter 1

Introduction

1.1 Coronary Angiography

Coronary artery disease (CAD), also known as coronary heart disease (CHD), is a serious illness, which is responsible for 1 of every 5 deaths in Europe [1] and 1 of every 6 deaths in US [2]. In addition to the severe mortality rates, the direct and indirect costs associated with CAD are major burdens on healthcare systems [1,2]. Early diagnosis of CAD, effective prognostic markers of treatment outcome, and the availability of minimally invasive treatment options for CAD have all motivated steady progress in diagnostic and interventional imaging modalities to quantify the anatomy and function of the coronary arteries.

Current clinical practice for assessing the presence and the extent of the CAD relies on medical imagery acquired through various diagnostic (cardiac computed tomographic angiography (CCTA) [3–5] and magnetic resonance angiography (MRA) [6]) and interventional (X-ray coronary angiography [7, 8]) imaging modalities. Other hybrid imaging modalities such as intravascular ultrasound (IVUS), optical coherence tomography (OCT) [9] can be used diagnostically. Apart from their diagnostic role, these imaging modalities also help clinicians to select between therapeutic options and plan interventional procedures. These modalities also differ in terms of invasiveness. CCTA and MRA are non-invasive modalities, whereas X-ray coronary angiography, OCT and IVUS requires minimally invasive intervention.

Invasive (catheter-based) X-ray coronary angiography is one of the most commonly utilised methods to assess CAD and is still considered the gold standard in clinical decision making and therapy guidance [5]. This imaging modality is based on the radiographic visualisation of the coronary vessels with injection of a radiopaque contrast material [10]. X-ray coronary angiography essentially provides anatomical information about the coronary arteries and the morphology of the stenoses. It can also provide limited functional information such as blood flow in the main coronary vessels and the existence of collateral flow [11].

1.2 Types of Coronary Angiography Systems

Thanks to the advances in C-arm based angiography systems in the cardiac catheterisation laboratory (cath-lab), various kinds of X-ray coronary angiography exists, namely single plane (standard/conventional), biplane, rotational and dual-axis rotational coronary angiography (DARCA).

Since X-ray coronary angiography creates 2D projection images of the complex 3D/3D+time (3D+t) anatomy of the coronary artery arteries, multiple images should be collected by placing X-ray source and detector in different positions to ease CAD assessment. Positioning is handled by C-Arm based angiography system (Fig. 1.1). C-arm is essentially a C-shaped device, which holds X-ray source and flat-panel detector (image intensifier in older systems). Depending on the setup, C-arm allows movement of X-ray source and the detector along several axes. In fact, the trajectory of the movement of C-arm is the fundamental design parameter that differs between different types of X-ray coronary angiography protocols.

Clinical decision making requires an appropriate number of angiography images which depends on the difficulty of the clinical case. On the other hand, several other factors should be taken into account for the design of an X-ray imaging protocol which may limit the total number of acquired angiography images: i) Contrast material may cause chemotoxic adverse reactions (such as contrast-induced nephropathy) directly related to the dose, molecular structure, and physiochemical characteristics [12, 13]. ii) Modern X-ray coronary angiography systems equipped with automatic exposure control units that try to balance the image quality and the X-ray tube voltage parameters. Although automatic exposure control effectively limits the exposure to X-ray radiation, further reduction is desired for increased safety. iii) Finally, the procedural time is also another important matter due to the high number of percutaneous coronary interventions (PCI) [2].

Standard X-ray angiography is the traditional way of X-ray coronary angiography, which consists of imaging the coronary arteries from a few fixed, operator chosen views. Therefore, the success rate of the diagnosis and the following treatment are solely dependent on the skills of the operator [11]. Although expert recommended views for standard X-ray angiography exist, they do not necessarily lead to satisfactory images due to the patient variability [11]. Even though standard X-ray angiography is currently the gold standard in interventional cardiology, it has some limitations in terms of contrast material use, procedural time and radiation exposure.

A biplane X-ray angiography system consists of two C-arms, which are generally configured to collect angiography images from orthogonal views. As a result, the biplane X-ray angiography system doubles the number of images that are acquired during a single contrast injection. However, operator dependency on the image acquisition quality persists.

Rotational X-ray angiography is an advanced scanning technique, which is devised to standardise and automatise the image acquisition [11]. It provides an operator independent, panoramic view of the coronary arteries by collecting a series of images during a predefined C-arm rotation [14]. The continuity in the collected images help the operator to mentally visualise the dynamic spatial structure of the coronary arterial tree.

Traditionally in rotational X-ray angiography, rotation of gantry starts from 55° to 60° right anterior oblique (RAO) and ends at 55° to 60° left anterior oblique (LAO) with some cranial (CRA) or caudal (CAU) angulation. Extended rotational X-ray angiography is a novel acquisition protocol in which the arc that goes from 120° LAO to 60° RAO where no angulation is introduced (Fig. 1.1) [15]. Extended rotational X-ray angiography facilitates the use of tomographic reconstruction based algorithms to reconstruct the contrast filled high contrast coronary arteries. However, it should be noted that extended rotational X-ray angiography is different from cardiac C-arm CBCT, which also provides tomographic reconstruction. Extended rotational X-ray angiography runs faster than cardiac C-arm CBCT and requires less images because it is used to reconstruct high contrast objects [16]. Nonetheless, extended rotational X-ray angiography capability is also integrated into the state-of-the-art C-arm CBCT devices. Extended rotational X-ray angiography has some specific issues because of the prolonged acquisition time, such as prolonged contrast injection [15] and motion due to breathing.

Dual-axis rotational coronary angiography (DARCA) is an improved form of rotational X-ray angiography, which further increases the patient safety and eases the acquisition of the angiography images. DARCA combines the acquisitions with CRA and CAU angulation into one single acquisition run [8]. Moreover, the trajectories for the rotation of C-arm are not randomly selected but optimised in DARCA (Fig. 1.1). The optimised trajectories allow to collect images with minimal vessel overlap and foreshortening and are consistent with the expert recommended views [17].

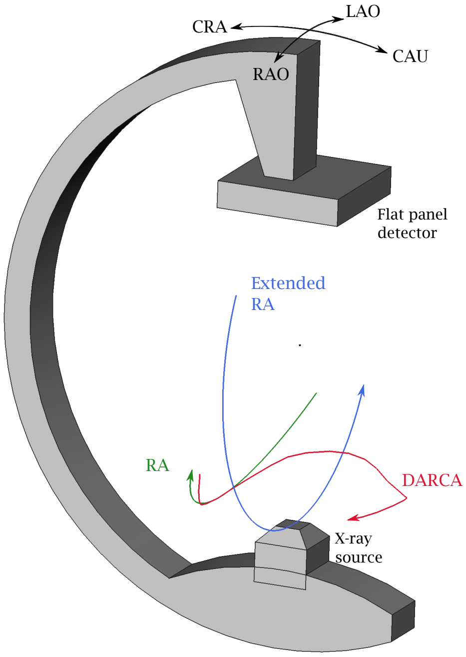

Figure 1.1: C-arm trajectories for different X-ray angiography types: Typical trajectories that X-ray source follows during rotational X-ray angiography, extended rotational X-ray angiography, and DARCA are shown by green, blue, red curves, respectively.

1.3 Necessity and Potential Uses of Coronary Artery Reconstruction

Despite the advent of 3D non-invasive imaging modalities (CCTA, MRA) to visualise the coronary arteries, 2D invasive X-ray coronary angiography is still considered the gold standard for the clinical decision making and therapy guidance due to several reasons [5]. The technology is widespread and trained staff is available. Moreover, X-ray coronary angiography still delivers highest spatial and temporal resolution. More importantly, it is an interventional imaging modality, which does not only provide diagnostic information but also guides the following therapeutic procedures [18].

Although X-ray coronary angiography has drastically evolved since its first introduction five decades ago, it is known to be fundamentally limited in some aspects [11, 19]. X-ray coronary angiography represents complex 3D/3D+t structure of the contrast filled coronary arteries by 2D X-ray projections or silhouette images, which can be degraded by imaging artifacts [11]. A considerable amount of 3D/3D+t information of the coronary arteries is lost due to the consequences of the projection operation. Specifically, the cumulative effect of suboptimal projection angles, vessel overlap, foreshortening, tortuosity and eccentricity may all lead to underestimation of stenoses severity and incorrect stent size selection [11].

In order to obviate the fundamental limitation of X-ray coronary angiography described above, a 3D/3D+t description of the coronary arterial tree may be reconstructed from the 2D projection images. This inverse problem of reconstruction is known to be ill-posed and it entails some additional challenges in the context of X-ray coronary angiography. These challenges include: intensity inhomogeneities due to blood flow inside the arteries, overlap of different structures (e.g. catheters, bones), and more importantly respiratory and cardiac motions [20]. Moreover, the diversity of the X-ray coronary angiography strategies inevitably leads to the diversity of the 3D/3D+t reconstruction algorithms, because different strategies necessitate special considerations for the reconstruction algorithms.

A 3D/3D+t reconstruction could i) ease diagnostic decision making, ii) assist pre-operative planning, iii) provide intra-operative guidance, and iv) supply virtual physiological indices.

Traditionally, the assessment of stenoses, the selection of the correct treatment for the patient, and the delivery of the treatment depend on the operator's interpretation of 2D projection images [18]. Lesion lengths, angles of bifurcations and vessel tortuosity may be misinterpreted in 2D projection images. In addition, subjective interpretation of 2D images could also lead to inter-observer and intra-observer variability. More importantly, misinterpretation could also lead to over/under estimation of lesion severity and incorrect selection of stent size [21,22]. Consequently, suboptimal selection of the stent dimensions could reduce the effectiveness due to poor lesion coverage [21], cause restenosis [23] or thrombosis [23,24] and increase the cost of the treatment [21]. In order to overcome these diagnostic problems and select an optimal stent dimension, computerised measurements of lesions (such as minimum luminal area, percentage area stenosis, minimum luminal diameter etc.), which are considered to be correlated with the degree of the stenosis, are utilised [25]. This procedure is generally known as quantitative coronary angiography (QCA). With the development of 3D coronary artery reconstruction algorithms, QCA can now performed in 3D reconstruction of the lesion of interest [26,27], which is shown to be in an agreement with ground truth measurements via guide-wire or IVUS measurements [28–31].

Image fusion is another emerging field in medical imaging. It aims to supply complementary information (anatomical/functional information, pre/post-operative information, device visibility, soft tissue visibility) from different imaging modalities. Specifically, X-ray coronary angiography could be supplemented by pre-operative 3D images from CCTA, cross-sectional morphology information from IVUS or OCT. Fusion of X-ray coronary angiography with pre-operative CCTA could bring the intervention planning visually into the cath-lab [32] and provide additional information especially in the patients with chronic total occlusions [33,34]. Although most of CCTA/X-ray coronary angiography fusion algorithms are formulated as 2D/3D registration [32,33], one recent study showed that the problem can be cast as a 3D/3D registration problem by the help of 3D reconstructions from biplane X-ray angiography [34]. Fusion of X-ray coronary angiography with IVUS or OCT is also desirable since these imaging modalities are known to provide cross-sectional morphological information about the stenosis and plaque characteristics [35]. This type of fusion employs 3D reconstruction of coronary artery centreline and complements it with the surface information from IVUS/OCT [35,36].

The search for the link between the coronary anatomy and its physiology has led to a remarkable amount of research carried out in the image based hemodynamics modelling field [37,38]. Large scale randomised clinical studies reveal that significance of a coronary stenosis could not be determined solely on anatomical information and conclude that anatomical information from any imaging modality should be coupled by intra-coronary physiological measurements [39]. Among those physiological measurements, a comprehensive investigation is devoted to fractional flow reserve (FFR) [40,41]. Recently, there is a strong interest in estimating virtual FFR values using the flow and pressure values obtained through CFD simulations inside 3D anatomical models of the coronary arteries [42,43]. Virtual FFR via non-invasive imaging (CCTA, MRA) could pave the way for a non-invasive diagnosis of moderate stenosis. On the other hand, it is also feasible to calculate virtual FFR from the 3D reconstruction obtained from invasive X-ray coronary angiography [44–46].

Although there is a plethora of research evidence that highlights the clinical potential of the aforementioned applications, a large amount of the research carried out over the last ten years is still not fulfill the clinical requirements and is unfortunately not available in clinical routine. There are, however, several methods that start appearing as part of clinical research (see, for instance [44,46–50]). One of the major limiting factors for their translation into the clinics is that 3D reconstruction still needs to be simultaneously robust, accurate and real-time and meeting these three constraints at once has proven really challenging. As methods become more involved to deal with accuracy, they tend to be computationally expensive and sensitive to various parameters. As techniques attempt to achieve speed, they become prone to inaccuracies and lack robustness. To date, most of the commercially available algorithms still rely on intensive off-line manual interactions. Over the last few years, while parallel efforts on addressing this requirement trilogy have continued, many researchers have also focused on extracting functional or physiological information from imaging in addition to anatomical information [50]. However, automated algorithms that could provide reconstructions in (near) real-time are still required as input to these methods so the quest for accurate, robust and efficient algorithms for coronary anatomy reconstruction continues.

1.4 Contributions and Outline

The aim of this thesis is to develop robust algorithms to reconstruct 3D coronary artery centrelines from X-ray rotational angiography, and to assess the performance of these algorithms in realistic settings.

To achieve the aforementioned objective, one needs to identify the limitations of the approaches in the literature. To this end, Chapter 2 presents an exhaustive review of the state-of-the-art approaches on reconstruction of high-contrast coronary arteries from X-ray angiography. This chapter mainly focuses on the theoretical aspects in model-based (modelling) and tomographic reconstruction of coronary arteries, and discusses the evaluation strategies.

Chapter 3 introduces some of the fundamental aspects of the reconstruction methods presented in the rest of the thesis.

Chapter 4 describes the first methodological contribution to reconstruct 3D coronary arteries from a set of retrospectively gated X-ray angiography images. Most of the existing model-based reconstruction algorithms are either based on forward-projection of a 3D deformable model onto X-ray angiography images or back-projection of 2D information extracted from X-ray angiography images to 3D space for further processing. All of these methods have their shortcomings such as dependency on accurate 2D centreline segmentations. In Chapter 4, the problem is approached from a novel perspective, and is formulated as a probabilistic reconstruction method based on a Gaussian mixture model representation of the point sets describing the coronary arteries. Specifically, it is assumed that the coronary arteries could be represented by a set of 3D points, whose spatial locations denote the Gaussian components in the mixture model. Additionally, an extra uniform distribution is incorporated in the mixture model to accommodate outliers (noise, over-segmentation etc.) in the 2D centreline segmentations. Treating the given 2D centreline segmentations as data points generated from mixture model, the 3D means, isotropic variance, and mixture weights of the Gaussian components are estimated by maximising a likelihood function. Results from a phantom study show that the proposed method is able to handle outliers in the 2D centreline segmentations, which indicates the potential of our formulation.

Chapter 5 investigates 3D+t reconstruction and describes a new method for finding 3D+t centreline points on coronary artery tree given tracked 2D+t centreline point locations in X-ray rotational angiography images. In order to address the ill-posedness of the reconstruction problem, a statistical bilinear model of the ventricular surface is used as a spatiotemporal constraint on the non-rigid structure of the coronary arteries. The 3D+t reconstruction problem is formulated as a 2D+t/3D+t Gaussian mixture model based registration between the tracked 2D arterial centreline point locations on the X-ray images and the landmarks of the statistical bilinear model. The spatiotemporal statistical model and additional information from multiple X-ray views enable reconstruction of artery segments, which otherwise may be difficult to reconstruct. The algorithm is validated using a software coronary artery phantom.

Finally, Chapter 6 extends the algorithmic framework of the first contribution. Specifically, 3D coronary artery centrelines to be reconstructed are represented by a mixture of Student's t-distributions, and the reconstruction is formulated as estimation of mixture model parameters given the 2D centreline segmentations from multiple X-ray images. Our probabilistic formulation enables us to introduce Bayesian spatial regularisation and sparsity priors over the parameters to cope with the ill-posedness of the reconstruction problem. Thanks to the prior information and the heavy tails of the t-distribution components, our formulation can handle cardiac motion inconsistencies between X-ray images due to finite gating accuracy, and noisy or erroneously segmented parts in 2D centreline segmentations. A comprehensive evaluation is performed using both synthetic and clinical angiography data. Compared to the state-of-the-art, the proposed method requires fewer X-ray images and significantly less user interaction, achieving comparable reconstruction error.

The content of this thesis is based on the following publications:

- Chapter 1 and Chapter 2:
  S. Çimen, A. Gooya, M. Grass, and A. F. Frangi, "Reconstruction of Coronary Arteries from X-ray Angiography: A Review," *Med. Image Anal.*, vol. 32, pp. 46-68, 2016.

- Chapter 4:
  S. Çimen, A. Gooya, and A. F. Frangi, "Reconstruction of Coronary Artery Centrelines from X-ray Rotational Angiography using a Probabilistic Mixture Model," in *Proc. SPIE*, vol. 9784, 2016, pp. 97843A-97843A-7.

- Chapter 5:
  S. Çimen, C. Hoogendoorn, P. Morris, J. Gunn, and A. F. Frangi, "Reconstruction of Coronary Trees from 3DRA Using a 3D+t Statistical Cardiac Prior," in *Proc. Med. Image Comput. Comput. Assist. Interv.*, P. Golland, N. Hata, C. Barillot, J. Hornegger, and R. Howe, Eds., vol. 8674, 2014, pp. 619-626.

- Chapter 6:
  S. Çimen, A. Gooya, N. Ravikumar, Z. A. Taylor, and A. F. Frangi, "Reconstruction of Coronary Artery Centrelines from X-Ray Angiography Using a Mixture of Students t-Distributions," in *Proc. Med. Image Comput. Comput. Assist. Interv.*, S. Ourselin, L. Joskowicz, M. R. Sabuncu, G. Unal, and W. Wells, Eds., vol. 9902, 2016, pp. 291-299.

Chapter 2

Reconstruction of Coronary Arteries from X-ray Angiography: A Review

2.1 Introduction

In this review chapter, we focus on the 3D/3D+t reconstruction of coronary arteries from invasive X-ray coronary angiography. The most recent reviews [18,51] about coronary artery reconstruction provide a good overview of the subject but are partial reviews of the topic. In this review, we follow the taxonomy proposed by [18,51], and divide the literature into two main categories, dealing with model-based methods (modelling) and tomographic reconstruction aspects. Model-based methods try to find a binary representation of the 3D/3D+t structure of the coronary arteries [18]. On the other hand, tomographic reconstruction methods aim to reconstruct the 3D/3D+t volume of attenuation coefficients [51]. Specifically, we distinguish between the tomographic reconstruction of high contrast arteries from rotational coronary angiography and low contrast cardiac reconstruction from C-arm cone-beam CT (CBCT). In this review, we merely focus on the papers about high contrast coronary artery reconstruction.

The goal of this review is to identify the trends and the developments in the area rather than explaining application specific details. Compared with the previous reviews, we provide a more comprehensive technical overview of 3D/3D+t reconstruction from X-ray coronary angiography, focusing on the recent developments in the model-based and tomographic reconstruction. With respect to model-based reconstruction methods, we cover multi-view reconstruction techniques and put a special emphasis on 3D+t reconstruction and vascular lumen reconstruction. In addition, we discuss the progress in motion estimation and optimisation techniques for tomographic reconstruction methods. We also discuss the methods on how to evaluate the performance of the reconstructions, and summarise available databases for validation and comparison purposes.

This review chapter is organised as follows. Section 2.2 details the model-based approaches (Section 2.2.2) and tomographic reconstruction approaches (Section 2.2.3) to the 3D/3D+t reconstruction of coronary arteries from X-ray coronary angiography. A summary of Section 2.2 is given in Tables 2.1 - 2.2. Section 2.3 discusses the methods of validation and comparison, and finally, Section 2.4 concludes the review.

2.2 Reconstruction of Coronary Arteries from X-ray Coronary Angiography

In recent years, a significant amount of work has been devoted to obtain a 3D/3D+t representation of the coronary tree from X-ray coronary angiography. Different types of X-ray coronary angiography systems, strategies to handle cardiac and respiratory motion, and additional requirements have resulted in the diversity of the coronary artery reconstruction methods. Nevertheless, the methods in the literature could be classified into two main groups, namely model-based reconstruction (modelling) (Section 2.2.2) and tomographic reconstruction (Section 2.2.3). The main distinction between two classes of reconstruction methods is the reconstruction output. While modelling generates a binary 3D/3D+t representation of the coronary arteries, tomographic reconstruction produces a volume representing the X-ray absorption of the coronary arteries. Despite the separation of reconstruction methods, there are some general aspects, which are applicable to both classes. These aspects are discussed in Section 2.2.1.

2.2.1 General Aspects of the Reconstruction Methods

2.2.1.1 X-ray Coronary Angiography Type

One fundamental aspect is the selection of X-ray coronary angiography type. Due to specific requirements of the reconstruction methods, all types of X-ray coronary angiography are not suitable for both types of reconstruction (Section 1.2). While all types of X-ray coronary angiography are suitable for modelling, only rotational X-ray angiography allows tomographic reconstruction.

2.2.1.2 Image Acquisition Geometry and Calibration

Another common aspect is the acquisition geometry. The acquisition geometry for reconstruction methods is commonly described using the tools from the computer vision, since the acquisition principle of X-ray is similar to the finite projective camera model [52]. The main difference is that the X-ray images are magnified. Three coordinate systems are defined for the acquisition geometry, namely, X-ray source (camera), X-ray detector (image) and patient (world) coordinate systems (Fig. 2.1). X-ray source coordinates are centred at X-ray source location (camera

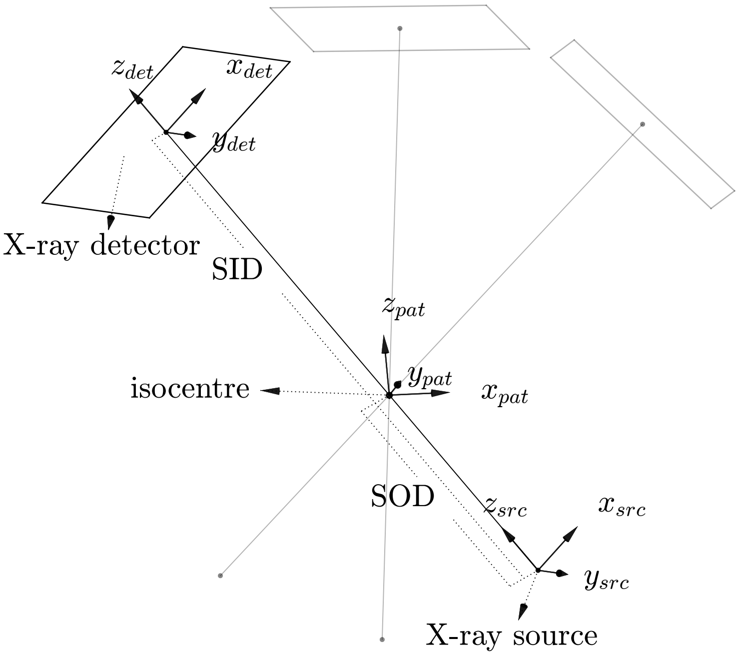

Figure 2.1: X-ray coronary angiography image acquisition geometry: Three coordinate systems, which are related to each other by a rigid transformation, are defined for X-ray detector, patient, and X-ray source. The origin of the patient coordinate system is typically assumed to coincide with the isocentre (centre of rotation of the gantry). Intrinsic and extrinsic parameters specify the mapping between patient and detector coordinates.

centre). Flat panel X-ray detector is modelled with a plane (image plane) perpendicular to one of the main axis of the X-ray source coordinate system. Distance between the X-ray source and X-ray detector is known as source to image distance (SID). The line from the X-ray source perpendicular to X-ray detector is known as principal line and it intersects X-ray detector at principal point. Image formation is determined by intrinsic parameters of the camera model, which are SID, coordinates of the principal point in the X-ray detector coordinate system, and sometimes skew parameter. These parameters form a matrix called camera calibration matrix, which is used to describe the mapping between points given in X-ray source coordinates and their 2D projection given in 2D X-ray detector coordinates. The centre of rotation of the gantry is called isocentre and considered to be the origin of the patient coordinate system. It is generally assumed to lie on the principal line. The relation between the X-ray source and patient coordinates is described by a rigid transformation. The parameters (rotation angles and source to object/patient distance (SOD)) for the rigid transformation are known as extrinsic parameters. Intrinsic and extrinsic parameters constitute camera projection matrix, which defines the mapping between patient and X-ray detector coordinate system[1]. The acquisition geometry enables us to define another important concept called projection line. A projection line for a point is the line that passes through the X-ray source and the projection of the point in the X-ray detector.

One minor point is the image distortion related to the X-ray detector. Older angiography systems are equipped with image intensifier that generates images with distortion due to its design. These distortions must be corrected either before applying the reconstruction method [53] or within the reconstruction method [54]. However, now the new angiography systems make use of flat panel detectors, which can create distortion free X-ray images [55].

It is necessary for both class of reconstruction methods to obtain the parameters describing the acquisition geometry. However, the way how the acquisition geometry obtained changes between different reconstruction strategies. Some methods rely on a prior calibration step to record the geometry parameters. During the image acquisition the X-ray gantry follows the recorded geometry to generate the X-ray coronary angiography images. In earlier, mechanically unstable C-arm systems, calibrations can be performed just before image acquisition [56]. However, in stable C-arm systems, the calibration is performed once in a while with regular intervals to ensure its stability [57–59]. The calibration is usually completed by using phantom objects [56–59]. Nevertheless, some methods opt for non-calibrated data because of the possible table translation during image acquisition or because of noise in the calibrated parameters. These methods either estimate geometry parameters before computing the reconstruction or jointly estimates the geometry parameters and the reconstruction. However, joint optimisation aggravates the problem by increasing the ill-posedness of it, and is not realistic. On the other hand, all of the tomographic coronary artery reconstruction methods assume calibrated geometry, while modelling based reconstruction can adopt calibrated and non-calibrated geometries (Section 2.2.2).

---

[1] Modern X-ray imaging systems store both extrinsic and intrinsic parameters.

2.2.1.3 Handling of Cardiac and Respiratory Motion

Another important aspect with regard to both classes of reconstruction is the respiratory and cardiac motion experienced by coronary arteries during image acquisition. Respiratory motion could be reduced during the acquisition by asking the patients to hold their breaths (see Tables 2.1 and 2.2). Considering there is no residual respiratory motion, retrospective gating strategies are commonly utilised to overcome cardiac motion. The main principle of retrospective gating is to select the subset of images that are at the same cardiac phase in order to eliminate the cardiac motion. The number of available cardiac cycles during the acquisition is important; high heart rates are preferable to low or normal cardiac phase in order to have sufficient number of images for reconstruction. Two different approaches are investigated for retrospective gating: ECG and surrogate based gating.

The most common way to achieve gating is to use ECG signal simultaneously acquired with the image acquisition. Specifically, this signal is used to assign cardiac phases to the collected X-ray images assuming a cyclic heart motion (Fig. 2.2). Typically, the phases of least motion, end-systole and end-diastole [60, 61], are employed for gating to obtain a higher 3D reconstruction quality.

Missing or unusable ECG (e.g. due to mislocation of electrodes), and irregular heartbeats pose further challenges for retrospective gating of images collected using a C-Arm system [62, 63]. In X-ray coronary angiography, motion phases can be assigned based on a surrogate function extracted from the intensity information in the X-ray images [64, 65]. To find such a surrogate function, several assumptions are made. First, it is assumed that there is no CRA/CAU angulation during acquisition and consequently axial direction of the patient is roughly aligned with vertical axis of the X-ray detector. Second, predominant motion in the axial direction is assumed to be caused by the cardiac motion. Under these assumptions, motion in the axial direction can be used as the surrogate function. Blondel *et al.* [64] determined the motion by estimating the shift between horizontal line integrals of subsequent X-ray images. Lehmann *et al.* [65] calculated centroid of the horizontal line integrals and use its motion to define the surrogate. From a different perspective, these methods find an optimal time point to compute the reconstruction.

A related problem is to select the optimal cardiac phase for the reconstruction,

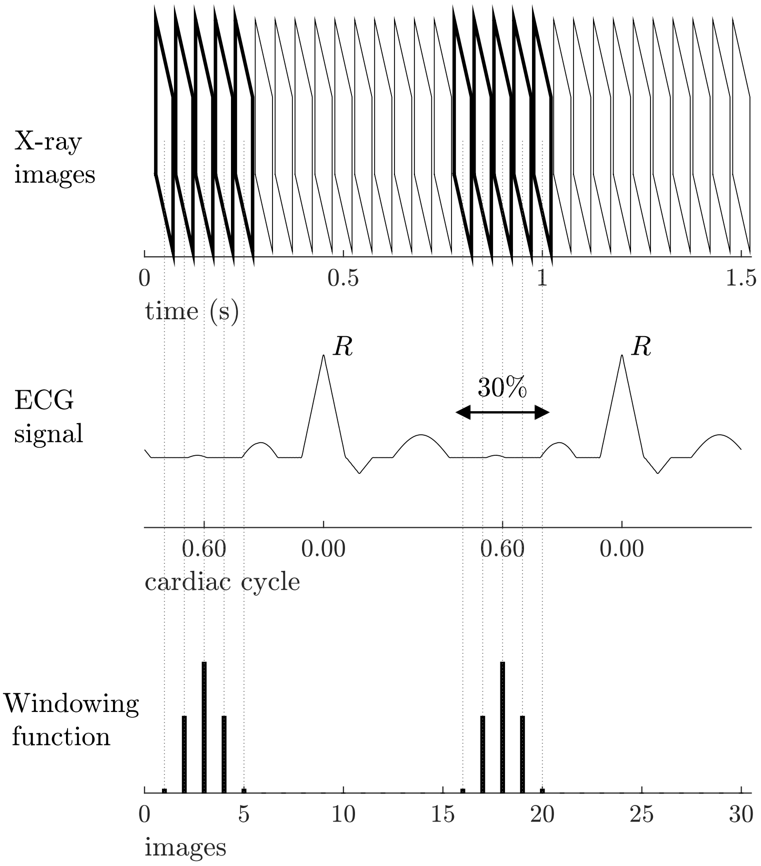

Figure 2.2: Retrospective ECG gating: A subset of images corresponding to the same cardiac phase are selected to discard the cardiac motion before reconstruction (top). Each image is assigned a cardiac phase using the ECG signal recorded simultaneously with the image acquisition (middle). A windowing function specifies a temporal slot and weighting for image selection (bottom).

given the gating signal. Because of the heart rate differences and other special conditions (e.g. arrhythmia) of the patients, the optimal cardiac phase for reconstruction is different between the patients [61]. Moreover, it is known that the reconstruction quality varies among different cardiac phases [66]. Apart from using aforementioned surrogate functions, several methods are devised to determine the optimal phase. The methods described in [67, 68] build a series of gated reconstructions and define a quality metric based on the histogram analysis of those reconstructions. The mean intensity value of the high contrast voxels are used as the quality metric. Hansis *et al.* [69] used minimum intensity projections of a back-projected distance map to determine a quality measure for the cardiac phases assigned via ECG signal.

The selection of images are generally conducted by a windowing function. A windowing function defines a temporal slot around the selected cardiac phase; the X-ray images inside that domain are selected for reconstruction. The shape of the windowing function introduces a weighting to X-ray images depending on temporal distance of X-ray image to the selected phase. Most commonly used windowing functions are nearest-neighbour [66,70] or power of cosine function [66,71,72]. The nearest-neighbour function selects the image that is closest to the selected cardiac phase. This gating function strictly eliminates the cardiac motion by selecting one image for each cardiac cycle. However, it severely undersamples available X-ray projection data and this can lead to artifacts in the reconstruction [66]. Instead of nearest-neighbour gating, bell-shaped functions are also used as the windowing function. One popular choice is cosine squared windowing function [66]. A more general family of cosine functions, namely power of cosines, are introduced in [71]. Specifically, the shape of the windowing function is controlled using a parameter describing the power of the cosine function. In addition, there are also some attempts to determine the optimal window length from X-ray images using value of the surrogate function [65]. Finally, one should note that cardiac motion type (e.g. twisting motion [73]) and magnitude could still lead to undersampling problems even using bell-shaped or surrogate based windowing functions.

2.2.2 Model-based Reconstruction

Model-based reconstruction (or modelling) methods try to build a 3D/3D+t binary model of coronary arteries, which consists of a 3D/3D+t centreline and, occasionally, the vessel surface. These methods are flexible tools for reconstruction, since they allow us to use images from all X-ray coronary angiography modalities or from calibrated and non-calibrated systems. However, the flexibility is usually accompanied by requirement of manual processing. Although these methods commonly use ECG gating to remove the motion of coronary arteries (Table 2.1), there are efficient ways to propagate the 3D reconstruction for one cardiac phase to the remaining phases to obtain 3D+t reconstruction.

Based on the overall design, modelling methods could be further divided into two groups, namely forward-projection based (Section 2.2.2.1) and back-projection based (Section 2.2.2.2) methods. Modelling methods could also differ in terms of ability to obtain 3D+t reconstruction (Section 2.2.2.3), multi-view modelling capability (Section 2.2.2.4) and vascular lumen reconstruction (Section 2.2.2.5).

2.2.2.1 Forward-projection Based Methods

Forward-projection based modelling methods for coronary artery reconstruction employ a 3D model, which adapts itself to the vessel structures in 2D X-ray projection images.

Deformable models are frequently employed in forward-projection based reconstruction. The deformable model evolves under the influence of an external energy, which is obtained from the 2D images and an internal energy, which is due to the smoothness and topology of the model itself. The most commonly used 3D deformable model for modelling of the coronary arteries are active contour model [74]. In the context of coronary reconstruction, each coronary artery branch is represented by one active contour model and these models are optimised individually. The main concern for active contour based reconstruction is the design of the external and internal energy terms.

Two-dimensional external energy terms are generally computed using the image information from the 2D projection images and used in various ways to update the location of the 3D landmark points describing the active contour. In order to calculate 2D external energy terms for each landmark point, common approaches are to compute the Gradient Vector Flow (GVF) [75], Generalised Gradient Vector Flow (GGVF) [76], and Potential Energy (PE) [77] from the 2D projection images and use the resulting 2D vector fields [54, 78–81]. Centrelines segmented from 2D projection images are used as the feature map input to GVF, GGVF and PE computation. Alternative to this approach, image intensity information can be directly used to compute the external energy term. The intensity values are locally minimum at the image pixels corresponding to the vessel axis, since X-rays passing through the vessel axis penetrate the thickest layer of contrast [82]. The direct [82] or normalised [83] sum of intensity values from different projection images are used to formulate the external energy term. In [83], authors also added the gradient of the intensity to the formulation to gain some robustness to noise on the 2D pixel values.

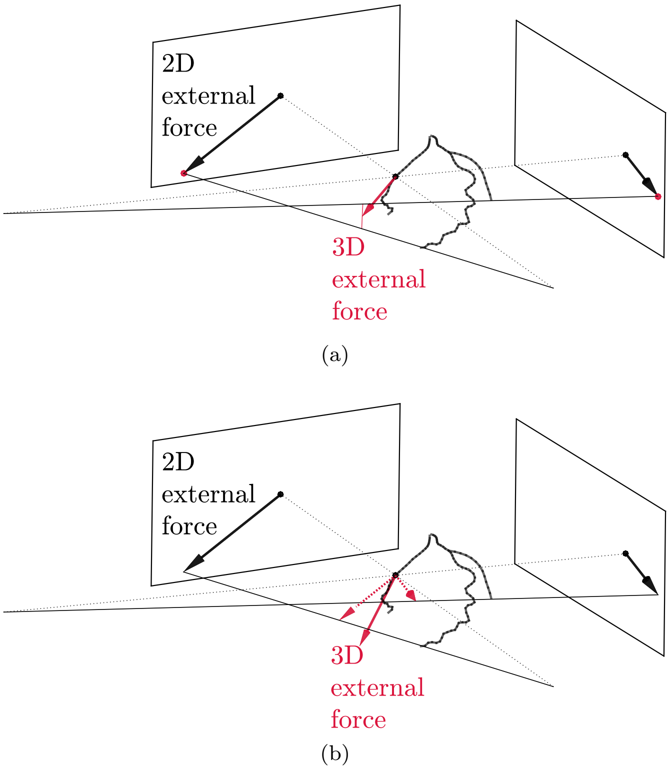

(a)

(b)

Figure 2.3: Computation of external force for active contour based reconstruction methods: (a) 3D external force can be computed using new 2D locations updated using 2D external forces. (b) Alternatively, 3D external force can be computed using back-projections of the 2D external forces.

In order to update the position of the 3D landmark points of the active contour, one strategy is to update the projections of the landmark in 2D [54, 78]. Specifically, the 3D landmarks for the current iteration of the active contour evolution are projected onto the 2D images. The 2D projections of landmarks are moved to new locations in 2D according to the external force. Because of the epipolar geometry, a new 3D position for the landmark must located at the intersection of the projection lines. However, updated 2D projections do not comply with the epipolar constraints, since they have been updated independently in the projection images. Therefore, the new 3D position of the landmark is found as the 3D position, which minimises the distance to all projection lines (Fig. 2.3a). Another strategy is to compose a 3D external force term using the 2D external force terms [79–81]. To this end, the 2D external forces are back-projected onto the world coordinate system by ignoring the out-of-plane component of the 3D external force. The back-projected external energy forces are added together to obtain the 3D external force (Fig. 2.3b). The main advantage of this strategy is to update the 3D landmark points without violating the epipolar constraints, which is proven to increase the accuracy and the convergence rate [80, 81]. Additionally, this strategy is easy to adapt to multi-view scenarios since the 3D external force is given by a simple vector addition operation [80].

As the internal energy, the elastic and bending energy from the original active contour model [74] are generally used. Zheng *et al.* [83] devised a new elastic term to avoid shrinkage problem of the open active contour model. This new term produces an additional penalty for the landmark pairs, which are not separated by the average distance between all pairs of neighbouring landmarks.

Initialisation of the active contour model in 3D is performed manually [54, 78–83]. Some corresponding points (including the start and end point) for a branch are selected from different views and rough reconstructions are obtained for these points. These points are used to generate a piece-wise linear active contour model to start with.

Although the literature on the forward-projection based modelling of coronary arteries revolves around parametric active contour models, there are some exceptions to this trend. As one notable example, Sarry *et al.* [84] used Fourier descriptors as the parametric deformable model. An analytical relationship between the 3D Fourier descriptor and its projection is derived. This relationship yields to an energy functional, which consists of intensity, epipolar constraint and smoothness terms. Another interesting example uses geometric active contours as the deformable model [85]. A 3D level set surface for the coronary artery is defined in a reference cardiac phase. It is assumed that this level set surface is mapped to a 2D projection image by rigid transform due to motion of the arteries followed by a projection operation. An energy minimisation framework is formulated to evolve the level set in the reference phase and to estimate the rigid transformation for all the projection images. Çimen *et al.* [86] used a statistical bilinear model of ventricular epicardium as spatiotemporal model, and estimated parameters of the bilinear model along with the arterial locations on the bilinear model.

Forward-projection based modelling methods do not require any correspondence between centrelines extracted from 2D X-ray images. Moreover, 2D segmentations are unnecessary for some of the methods, which work directly on the intensity values. These features provide serious advantages over most of back-projection based modelling methods in the literature. In addition to that, it is easy to adapt forward-projection modelling methods for reconstruction from multiple views. However, these methods rely on manual selection of corresponding points from projection images for each branch of the artery, which might be time consuming and prone to errors.

2.2.2.2 Back-projection Based Methods

Back-projection based modelling methods build the coronary artery tree from back-projection of 2D information extracted from projection images that are selected via ECG gating. These methods could be divided into two main groups: i) methods based on 2D feature matching, and ii) methods based on back-projection of vesselness responses.

The first group of back-projection based methods are the methods based on 2D feature matching. These methods start with a segmentation of artery centrelines and often several salient structures (e.g. start/end points, bifurcations) from the projection images. Correspondences are established between the centrelines from different views using epipolar geometry, and 3D points representing the coronary artery tree are reconstructed using the triangulation method [52] from the computer vision (Fig. 2.4a).

Two-dimensional feature matching based modelling methods are designed to work with the non-calibrated systems [64,87–92], although exceptions exist [20,93]. This is because the estimation of geometry parameters that relate the projection images used for reconstruction can be easily integrated into the method. One way is to estimate the geometry parameters before reconstruction commences. For this purpose, the salient points (e.g. start/end, flexion and bifurcation points) that are extracted during the segmentation step are exploited [87–89, 94]. A set of corresponding points are formed via manual establishment of correspondence. This set can be used to write constraint equations using the fundamental or essential matrix [87] or to formulate an energy function whose minimum is given by the optimal values for the geometry parameters [88, 89]. Generally, rotation and

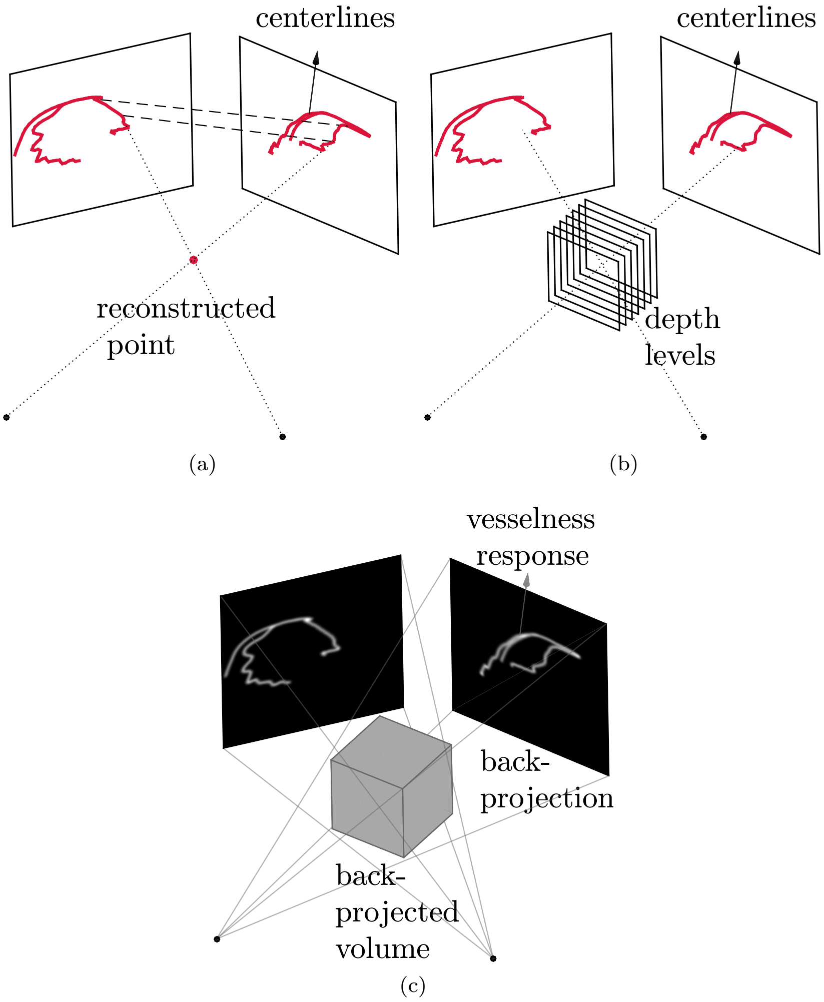

(a) (b) (c)

Figure 2.4: Summary of back-projection based methods: (a) Methods based on 2D feature matching establish correspondences of centrelines from different 2D views and compute reconstruction using triangulation. (b) Some of the 2D feature matching based methods divide the 3D space into parallel planes representing the depth levels. Each centreline point in the reference frame is assigned to one of the depth levels using the information from multiple X-ray images. (c) Methods based on back-projection of vesselness response compute a 3D volumetric vesselness response from 2D vesselness responses for further processing.

translation between the X-ray sources are considered to be the geometry parameters to optimise, and intrinsic parameters are assumed to be known. The energy function mainly consists of the reprojection error of points and the reprojection error of direction vectors [88, 89, 94]. Another popular way is to estimate geometry parameters jointly with the reconstruction. In this strategy, estimation of the geometry parameters and reconstruction, and the establishment of the correspondences are iteratively performed until a convergence criterion is met [64, 90–92]. These methods are advantageous because they are robust against outliers and provide a mechanism to estimate the intrinsic parameters as well. In [92], a total of 14 parameters are optimised including intrinsic (SID, principal point coordinates, skew) and extrinsic parameters (rotation, translation, table translation). For any approach to estimate the geometry parameters, initialisation is important. In most of the cases, the geometry parameter estimation starts from the values recorded by the X-ray system.

Correspondence establishment is the critical step for feature matching based methods, since the corresponding points are directly used to triangulate the 3D position. The simplistic approach is to use hard epipolar constraints to establish the correspondences [87–89, 94]. However, epipolar lines usually do not produce a single match and this necessitates more sophisticated approaches. One solution is the exploitation of dynamic programming algorithms. Yang *et al.* [92] used a method similar to dynamic time warping (DTW) [95] to find the correspondences. Dynamic programming can also be used to put soft epipolar constraints [64, 90]. Soft epipolar constraints allow for a point in the first view to match a point in the second view that is not strictly on the epipolar line but around it. To this end, an energy function is formulated for matching that consists of unary and binary terms. Unary terms penalise according to the distance to the epipolar line [90] or any feature that reflects correct correspondence (e.g. high tubularity value) [64]. On the other hand, binary terms ensure that the linked points in the first view are paired with points that are close to each other in the second view [64] or ensures that the deviation from epipolar lines varies smoothly [90]. In order to avoid point-to-point correspondences, a branch-to-branch correspondence establishment method is proposed in [20]. The projection lines formed by the 2D points in the projection images and corresponding X-ray source position form ray bundles for each view. Closest points on the ray bundle from first view with respect to the ray bundle from the second view establishes a correspondence. Another way to support the correspondence finding is to estimate some 3D features from 2D features and use the estimations to put a constraint on the correspondences. One particular example is the study in [91]. Given an initial correspondence, 3D curvature value for a point is estimated from the 2D curvature values from projection images. They compared estimated curvature and the curvature obtained from the reconstruction for the initial correspondence, and if the values are very different from each other the point correspondence is discarded. Although the authors used it for outlier removal, it is a promising strategy to put prior information on the 3D reconstruction.

One alternative strategy for 2D correspondence establishment is proposed in [96] and later adapted for dynamic reconstruction in [97]. The problem is formulated as a depth map estimation, inspired by multi-view stereo in the computer vision literature. To this end, the 3D space between X-ray source and detector is divided into parallel planes of equal depth increments (Fig. 2.4b). To obtain the reconstruction, all 2D centreline points in one reference view are assigned to a plane, i.e. assigned a depth value using an energy function minimisation. Liao *et al.* [96] proposed an energy function consisting of a reprojection error term and a term for smoothness of depths in 3D. The energy minimisation can be performed through efficient methods such as graph cuts or belief propagation [98].

Modelling methods based on 2D feature matching provide flexible and modular approaches to reconstruction. There is a wide selection of methods to choose from for segmentation, estimation of imaging geometry, and establishing the correspondences. More importantly, their ability to estimate the imaging geometry is indispensable for reconstruction from standard X-ray angiography, since table movements are common during image acquisition. Requirement of 2D segmentation is the main disadvantage of these methods. First, it hinders its use for multi-view reconstruction because segmentation of 2D projection images is generally a demanding (especially if there is overlap and foreshortening) and time consuming task. Second, one should select projection images at the same cardiac phase, with some angular difference (between 35-145 degrees [93]), without overlap and foreshortening, and with sufficient contrast. These conditions may not be satisfied easily and as a result the method may output suboptimal reconstructions.

The second group of back-projection based methods are the methods based on back-projection of vesselness responses. These methods compute vessel responses, which highlight coronary arteries in 2D projection images. These responses are back-projected given the imaging geometry to compute a volumetric vessel response in 3D. Segmentation methods are applied on the 3D vessel response to obtain the coronary artery reconstruction (Fig. 2.4c).

The first choice for these methods is the type of the 2D vessel response. Binary segmentation [99], tubularity response [100], and distance map to centreline [101] are used in the literature. Second choice is the back-projection operator. Different operators have been studied in the literature, namely multiplicative combination from all views [99], weighted multiplicative combination from all pairs of views [100] and maximum of 2D distances to centrelines [101]. Three-dimensional segmentations can be obtained from a variety of methods, although fast marching propagation [99,100] and minimal paths [101] are the only ones used so far. Owing to low number of projection images, 3D vessel responses are generally very noisy and robust methods for segmentations are required. Otherwise, post-processing steps might be required to prune the segmentation [99,100].

Modelling methods based on back-projection of vesselness response work with minimum level of interaction. Additionally, being inherently multi-view is a merit, however these methods might require extended rotational X-ray angiography images to increase the number of images available for reconstruction and to reduce the noise in the 3D vessel response function.

2.2.2.3 3D+time Model-based Reconstruction

3D+t reconstruction of coronary arterial tree could give the clinician a better assessment of the target lesion by providing information about motion and extent of deformation near the lesion [89]. Modelling methods could be extended such that they have the ability to generate 3D+t reconstructions of coronary arteries.

The most straightforward 3D+t reconstruction strategy to obtain 3D reconstructions for a number of cardiac phases separately [20,89,90,102]. This could be achieved by completely handling the reconstruction for each cardiac phase independent from each other [89,102]. To avoid complete independence of reconstruction at different cardiac phases, temporal constraints penalising the difference between neighbouring cardiac phases can be used [97]. The disadvantage of processing each cardiac phase individually is the requirement of segmentations for every cardiac phase, which may sometimes be infeasible. Another drawback of working on each cardiac phase separately is that the resulting 3D reconstructions are independent from each other and there is no notion of temporal correspondence. If the motion field for the coronary artery tree is needed, temporal correspondences should be sought [89,102]. This can be achieved by branch matching or tree matching algorithms. For example, Chen *et al.* [89] proposed a branch matching algorithm using a physics based principle to formulate matching energy. Jandt *et al.* [102] devised an energy formulation for iterative matching of tree structures.

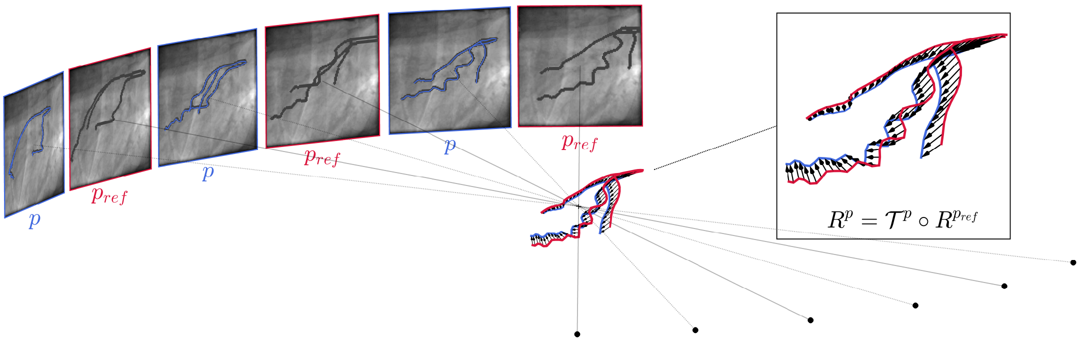

Figure 2.5: Propagation of initial 3D reconstruction by transformation optimisation: The transformation for cardiac phase p (T^p) is estimated such that the projection of deformed initial reconstruction is aligned with the vessel structures in 2D projection images at phase p. The initial reconstruction (R^{ref}) at the reference phase p^{ref} and deformed initial reconstruction (R^p) at phase p are shown in red and blue, respectively.

A popular strategy for 3D+t reconstruction is to propagate an initial 3D reconstruction from a reference cardiac phase to the rest of the phases [53,82–84,103,104]. Depending on the reconstruction methodology, there are two ways to accomplish this propagation. If it is a forward-projection based modelling method, the 3D deformable model representing the reconstruction for the reference cardiac phase is evolved such that its projection fits to the 2D projection images corresponding to the other cardiac phases. The easiest way is to use the 3D reconstruction as the initialisation at the next cardiac phase and to apply the same reconstruction strategy [84]. However, this strategy does not introduce any temporal constraints. To overcome this drawback, the deformable model energy for 3D reconstruction might be enriched with some additional terms that enforce temporal smoothness [82,83]. Four-dimensional propagation strategies for forward-projection based methods are generally designed to work with intensity values of 2D projection images in order to avoid the necessity of centreline segmentations for all the 2D images. On the other hand, back-projection based modelling method approaches 3D+t reconstruction as a temporal transformation estimation problem. Specifically, these methods parameterise a 3D/3D+t transformation, which is applied to the reference 3D reconstruction, such that the projections of the deformed reconstruction align with the 2D projection images (Fig. 2.5) [53, 64, 103–105]. A rigid or affine transformation for each cardiac phase is optimised in [104]. A set of hierarchical transformations with increasing degrees of freedom are proposed to model the motion of the arteries in [53, 103]. Specifically, rigid, affine and 3D B-spline transformations are optimised respectively for each time step. A strategy to reduce the number of transformation parameters by estimating a transformation separately for each coronary artery branch is followed in [103]. A 3D+t B-spline transformation model is used in [105]. Instead of directly estimating the parameters of the transform, a motion vector field is calculated using an energy minimisation. A second energy minimisation is performed to estimate the parameters of the transformation using the motion vector field. In [64], temporal dimension is added to the transformation via a 3D+t B-spline transformation. To estimate the parameters of the transformation, an energy measure describing the quality of fit is used to estimate the parameters of the transformations. The energy term consists of a term for the projection error, a term to constrain structural changes and a term to ensure smooth transformation. In order not to segment centrelines, the projection error term generally depend on intensity based features such as tubularity measure [53, 64, 103] or GVF [104]. The energy term controlling the smoothness of deformation can be defined using the transformed points [104] or using the parameters (e.g. control points for B-spline transformation) of the transformation [53,64,103,105]. Application specific temporal or structural constraints, such as cyclic deformation constraint [104] or length preservation constraints [53], are taken advantage of as additional energy terms.

2.2.2.4 Multi-view Model-based Reconstruction

X-ray rotational X-ray angiography and DARCA offer a sequence of projection images from different views, which provides additional information for model-based reconstruction. Many state-of-the-art modelling methods benefit from the additional information. These methods differ in the way they use multiple projection images.

There are various ways to incorporate multiple views. Cong *et al.* [80] combined back-projections of 2D external forces to compute a 3D external force for an active contour based reconstruction method. Blondel *et al.* [64] generated 3D reconstructions for every pair of multiple views and fused them together to find the final reconstruction. Liao *et al.* [96] showed that, for back-projection based modelling, it is possible to integrate the information from multiple images using an elegant energy formulation for the correspondence. To this end, the authors formulated the problem not as a correspondence establishment but as a depth assignment to centrelines extracted from one of the projections. Li *et al.* [101] and Jandt *et al.* [102] used modelling based on back-projection of vesselness response, which inherently supports multiple views. Finally, Keil *et al.* [85] combined a geometric active contour model with a transformation to utilise all the images in a rotational X-ray angiography sequence.

Multi-view modelling could bring some advantages to the reconstruction. First, reconstruction methods that rely on only two projection images discard a significant amount of acquired images. Multi-view reconstruction benefits from extra information from the additional images, which improves the accuracy of the reconstruction [80,96]. Second, two projection images are not enough for correspondence establishment between the projections if there is substantial amount of vessel overlap or foreshortening. In such cases, additional information from multiple views could assist the correspondence establishment [96]. Finally, multiple images provide additional diameter measurements, which could be used to improve surface reconstruction [80, 93, 94, 96, 102]. However, necessity of manual processing from user may hinder the adoption of multi-view modelling. Therefore, it is important to invest on methods with minimal user interaction.

2.2.2.5 Vascular Lumen Reconstruction

Assessment of stenosis severity or simulations from 3D reconstruction of arteries demand not only the reconstruction of centrelines but also the reconstruction of arterial lumen walls. Vessel surface reconstruction is performed after centreline reconstruction using the vessel diameter information from the projection images.

The basic approach to vessel surface reconstruction is to use vessel diameter information from only one view [20, 88, 89, 96]. These methods extract the 2D diameter value by searching the vessel boundary perpendicular to vessel axis from one projection image. The diameter value is scaled to remove the scaling effect due to projection and the scaled diameter is used to fit a circle cross section perpendicular to the 3D vessel axis (Fig. 2.6a). These cross sections are used to create the surface of the coronary artery tree. Movassaghi *et al.* [93] adapted this basic strategy to multi-view reconstruction. The scaled diameter values from multiple views put additional constraints on the shape of the vessel cross sections. Instead of limiting the cross sections to circles or ellipses, an interpolation scheme is proposed to accommodate various cross sections in [102]. To this end, the authors found the points that constrain the cross section and angularly interpolated new points describing the cross section. The interpolation is defined as a weighted linear combination and the weights are given based on a local foreshortening value and angular difference. Andriotis *et al.* [94] observed that the plane where 3D circular cross section lies might not be perpendicular to 3D vessel axis due to the rotational movement of X-ray source (Fig. 2.6b). They proposed a strategy to extract diameter information using the plane of 3D circular cross section. Yang *et al.* [92] proposed an ellipse fitting method for two views that respects non-coplanar circular cross sections in 3D. Later, Cong *et al.* [80] showed that this strategy can be incorporated into the multi-view reconstruction scenarios by using a least squares fitting.

Apart from reconstructing the vessel surface using the information available in the 2D angiography images, there is also a recent interest in fusing 3D centreline reconstructions with vessel surface extracted from IVUS or OCT images [35,106,107]. In this type of the vascular lumen reconstruction, 3D catheter path [108] or 3D vessel centreline [109] is generally assumed to be reconstructed using X-ray images from a biplane system using a back-projection based method. The problem of vascular reconstruction is formulated in three steps: i) segmentation of IVUS/OCT cross sections, ii) identification of the centreline locations corresponding to ECG gated IVUS/OCT cross sections, and iii) correction for the axial orientations of cross sections [108–112]. The spatial correspondence is established assuming an initial correspondence and a constant pull-back speed [108, 109]. The axial orientation correction is typically handled using local geometry around identified

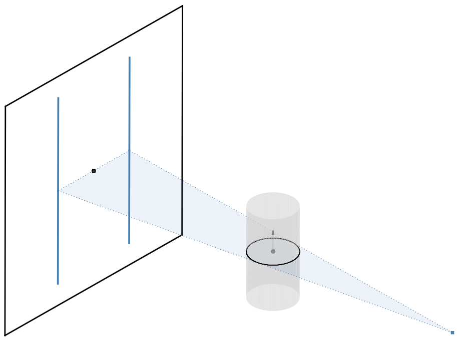

(a)

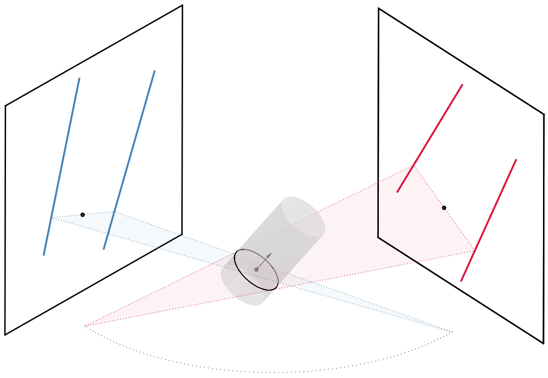

(b)

Figure 2.6: Effect of C-arm movement on the vessel surface reconstruction: (a) Projection plane (light blue triangular area) is often assumed to be perpendicular to vessel axis. As a result, projection plane and vessel cross section (black circle) are parallel to each other. (b) If the movement of the C-arm is taken into account, projection plane (light blue triangular area) and vessel cross section (black circle) are no longer parallel to each other. Furthermore, projection planes from different views (light blue and red triangular area) are non-coplanar.

centreline points [108–110, 112].

2.2.3 Tomographic Reconstruction

Tomographic reconstruction methods use X-ray coronary angiography images directly to produce a volume representing the coronary arteries. In contrast to binary representation of model-based reconstruction, tomographic reconstruction methods offer information about X-ray absorption coefficients. These methods can handle unusual anatomies (e.g. collaterals, tortuous branches) since they require less, if not none, prior information about the coronary arterial trees [113]. Because of the same reason, these methods can also provide more accurate vessel surface details [114]. In addition, tomographic reconstruction methods do not require any manual interaction.

Tomographic reconstruction methods need to fulfil specific requirements. All of the tomographic reconstruction methods assume that the X-ray imaging system is calibrated prior to the acquisition. Compared with modelling based reconstruction, these methods generally demand more X-ray images with a larger angular coverage. For this reason, extended rotational X-ray angiography acquisition is preferred as the acquisition protocol (Table 2.2). However, one should note that even extended rotational X-ray angiography does not satisfy Tuy-Smith data sufficiency condition [115, 116]. Moreover, as the coronary artery branches should be visible in the X-ray sequence, isocentring becomes crucial. Consistent contrast injection is also important to be able to exploit all the X-ray images. It is also important since these methods ignore the contrast agent propagation in their formulation and assume constant contrast distribution over time. Moreover, these methods typically have high computational demands compared with the modelling based reconstruction. However, thanks to the advances in parallel computing, dedicated GPU implementations can be used to overcome this difficulty (Table 2.3).

Similar to modelling methods, cardiac and respiratory motion are the most difficult challenges for the tomographic reconstruction. Typically, X-ray coronary angiography data are acquired during breath hold to minimise the respiratory motion. Depending on how they handle the cardiac motion, the tomographic reconstruction methods can be classified into three groups: i) gated (Section 2.2.3.2), ii) motion compensated (MC) (Section 2.2.3.3), and iii) gated and motion compensated methods (Section 2.2.3.4). The basic considerations and algorithms for tomographic reconstruction are briefly introduced in Section 2.2.3.1. These algorithms are generally adapted to the specific problem of high contrast moving object reconstruction and specialised algorithms are proposed. A detailed discussion of specialised algorithms for coronary artery reconstruction is provided in Section 2.2.3.5. Background removal strategies are discussed in Section 2.2.3.6. Finally, a brief discussion on 3D+t tomographic reconstruction is given in Section 2.2.3.7.

2.2.3.1 Preliminaries

One distinction between different methods is the type of the tomographic reconstruction approach. Both analytical and iterative tomographic reconstruction algorithms have been developed.

Analytical reconstruction algorithms consider a simplified system model and image (volume) model. Thus, they are best suited to the situations where approximate solutions are adequate. Yet, these methods are well-established and fast compared to iterative alternatives. Popular choice for analytical reconstruction of cone-beam geometries is Feldkamp-Davis-Kress (FDK) [117] algorithm.

Iterative reconstruction algorithms can integrate wide range of acquisition geometries (e.g. limited angular coverage), image model, forward model, noise model and prior information into the reconstruction [118]. The image model mainly deals with the representation of the volume to be reconstructed. The continuous volume is approximated by a linear combination of basis functions at discrete regular rectangular grid locations [119]. Among alternatives, voxel [120], Gaussian [121, 122], and blob-like (Kaiser-Bessel) [123–125] basis functions are utilised[2]. The forward model describes the contribution of the voxels along X-ray line (or X-ray beam) to the corresponding pixels [126]. Although forward model should be explicit to increase reproducibility of the method, it is not always reported. This is most probably due to the fact that most of the methods use the length of intersection between X-ray lines and voxel grid image model. Unlike most other work, Blondel *et al.* [120] used the volume of the voxel if the X-ray beam is passing through the voxel. The image model and forward model can be combined to form an underdetermined system of linear equations (forward projection equations), which relate projected pixels and voxels to be reconstructed by a forward projection matrix. The lack of measurement error modelling in the forward projection equations is addressed by appropriate noise models. In the context of coronary artery reconstruction, Poisson [123, 124] or Gaussian [125] noise models are employed. Finally, the spatial dependency between neighbouring voxels can be used to include any prior information about the volume.

Iterative reconstruction algorithms are classified into two groups, namely algebraic and statistical. This classification is made on the basis of whether they

---

[2] Unless otherwise noted, we assume that a voxel basis is used in the following discussion.

account for a noise model or not. Both group of methods have been used in the context of coronary artery reconstruction.

2.2.3.2 Gated Tomographic Reconstruction

As with the modelling methods, one simple way to reduce the effect of motion on the reconstruction is to apply gating, i.e. select a subset of images that correspond to the same motion state of the coronary artery tree (Section 2.2.1.3).

The initial attempts to tomographic reconstruction from X-ray rotational X-ray angiography have focused on the feasibility and optimisation of the acquisition protocols rather than the reconstruction method [70, 127]. Because of this reason, these studies utilise analytical FDK type reconstruction algorithms with nearest-neighbour gating. On the other hand, cosine squared windowing function is shown to improve the reconstruction if an optimal window size is chosen [66]. If the size of the window is increased, it possibly reduces the background artifacts but it leads to a blurred reconstruction due to motion [66]. These motion corrupted reconstructions are not satisfactory for clinical purposes, however they can be benefited as an initial coarse reconstruction for a motion compensated reconstruction [63, 71, 72, 128].

In recent years, the focus of gated reconstruction methods has shifted towards incorporation of prior information to cope with the undersampling due to gating. High contrast vessels occupy a small volume, therefore there must be a small number of voxels in the final reconstruction with nonzero voxel values [129,130], assuming background pixels are removed from the X-ray images (see Section 2.2.3.6). Since it is not possible to embed prior information into analytical reconstruction algorithms, iterative reconstruction algorithms with some kind of sparsity prior have been proposed. In [121, 130, 131], the forward projection equations are used as constraints and L1 norm of the reconstruction is minimised. Similarly, [132] minimised total variation (TV) norm of the reconstruction instead of L1 norm. Another way is to take a statistical approach and integrate the prior information in terms of a prior distribution model for the voxels. In particular, the voxel grid is considered a Markov Random Field (MRF) and the prior information is embedded using the clique potentials for the MRF. As the clique potentials, absolute value [123] and sign functions [124, 125] are used, which introduce TV-like and

L0-like priors, respectively. An interesting way to introduce the prior information is to use a 3D centreline model. The prior probability for each voxel is defined as a function of the distance from a reference 3D centreline model to that voxel [105].

2.2.3.3 Motion Compensated Tomographic Reconstruction

Since retrospective gating reduces the number of images available for the reconstruction, some reconstruction algorithms compensate for the effective motion instead of gating (Table 2.2). Essentially, the contributions from all X-ray images are brought to the same time point. Thus, all collected X-ray images are effectively used without introducing motion related artifacts. By means of a phantom coronary artery reconstruction experiment, Schäfer *et al.* [66] demonstrated that MC reconstruction can attain the quality of a static reconstruction from all projections, if the motion is known or estimated up to a certain accuracy. Therefore, the crucial part of every MC reconstruction algorithm is generally the motion estimation step.

MC methods require a representation of a motion field to model the mapping of the pixels or voxels from a reference time point to another time point. In general, the motion field is parameterised by a motion vector field or a geometric transformation. The temporal component of the motion field is commonly parameterised by cardiac phase assuming a periodic motion [64, 71, 105, 113, 119, 133]. However, the periodicity assumption is problematic for the cases where residual motion is strong or for the cases with arrhythmic heart motion [63]. Because of this reason, the temporal component is sometimes parameterised by acquisition time [63, 134, 135]. This strategy was shown to lead similar, if not superior, reconstructions.

Several types of geometric transformations have been investigated. A simplistic approach is to model the complex motion of the coronary arteries using 2D geometrical transformations acting on the X-ray images [113, 133]. Two-dimensional rigid [133] and 2D elastic [113] transformation are employed. Other studies use either 3D [71,105] or 3D+t [63,64,119,134,135] B-spline transformation. B-spline transformations offer spatial (and temporal if 3D+t) smoothness and achieve better results at the extent of an increase in the number of parameters to be estimated.

The parameters of the geometric transformation are estimated by an image registration method. For 2D transformations, an initial 3D reconstruction is obtained at a reference time and forward projected onto the projection images with a different time stamp. The parameter estimation problem is defined as estimating the registration between the features extracted from the projection images and the features extracted from forward projected images (Fig. 2.7a). 3D reconstructions of markers on the guide-wire [133] and ECG-gated tomographic reconstruction [113] are utilised to compute the forward projections. In some cases, the forward projected images are processed to extract some features (e.g. centrelines) for the registration [113]. For 3D and 3D+t B-spline transformations, various strategies are proposed. One option is to propagate a 3D modelling based reconstruction to the remaining projection images (Section 2.2.2.3) [64, 105]. Instead of a 3D modelling based reconstruction, a series of ECG-gated reconstructions can be obtained. These reconstructions are used to define an intensity based registration to estimate the parameters [71]. Other possibility is to estimate the motion parameters jointly with the reconstruction (Fig. 2.7b) [63, 119, 134, 135]. To achieve this goal, the parameters of the transformation are directly embedded into the analytical [63, 134, 135] or iterative [119] reconstruction formulations. An energy functional is derived from these formulations with the addition of appropriate regularisation term. The squared error between the projections of the reconstruction and X-ray images is used as the energy term in [119, 134]. Voxelwise multiplication of the reconstruction by a binarized reference 3D reconstruction is another alternative, which require a reference reconstruction [63, 135]. Starting from an initial set of parameters and reconstruction, parameters are updated by a gradient based optimisation and reconstruction is updated according to the reconstruction formula iteratively.

The compensation for the estimated motion is mainly performed in two ways. First, the X-ray projection images are deformed using the estimated geometric transformation [113, 133]. This is a trivial task if the estimated motion acts on pixels in 2D. On the other hand, if a 3D/3D+t motion field is estimated, it can be incorporated into the reconstruction formulation. Section 2.2.3.5 details how to achieve this for iterative [64, 105, 119, 120] or analytical [63, 66, 71, 134–136] formulations.

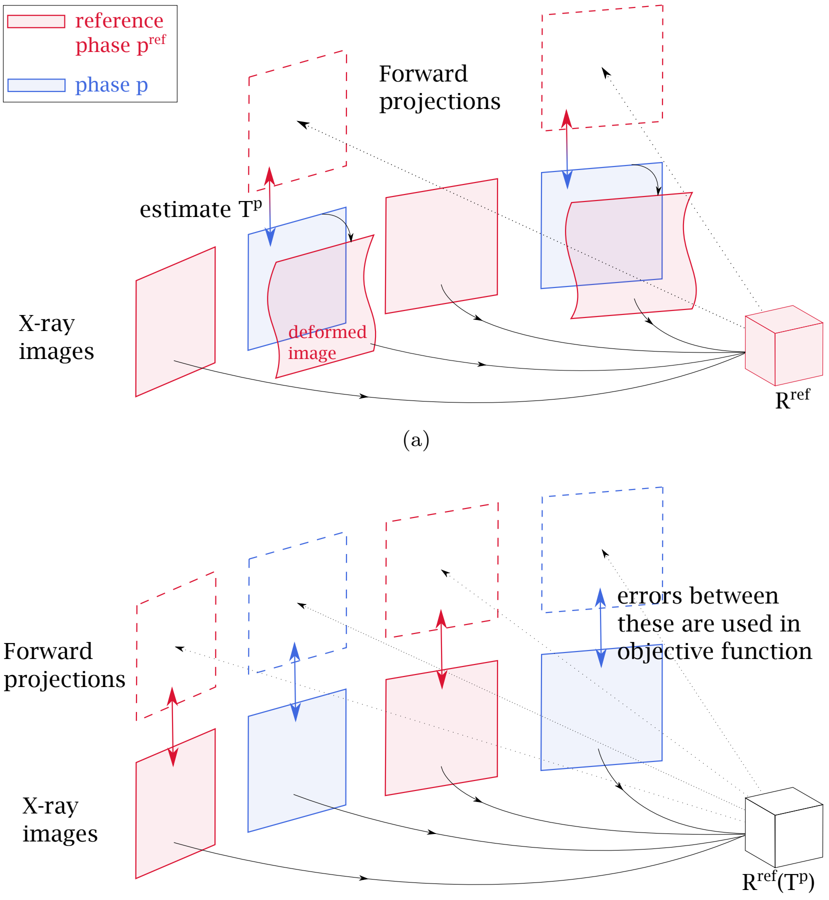

(a)

(b)

Figure 2.7: Motion estimation strategies for motion compensated (MC) reconstruction: The motion is parameterised by an appropriate geometric transformation, T^p, and the parameters of the transformation are estimated by a registration process. R^{ref} and R^p denote initial reconstructions at a reference cardiac phase p_{ref} and at an arbitrary cardiac phase p, respectively. (a) For 2D geometric transformation, the motion estimation can be formulated as a registration between the X-ray images and the forward projection of R^{ref}. The 2D images at phase p are deformed according to the estimated transformation, and utilised in the reconstruction process. (b) For 3D geometric transformation, one option is to compute R^{ref} and T^p jointly. This is generally achieved by embedding the T^p into the reconstruction formulation and iteratively estimating R^{ref} and T^p by minimising the error between the X-ray projections and forward projection of $R^{ref}(T^p)$.

2.2.3.4 Gated and Motion Compensated Tomographic Reconstruction

In gated tomographic reconstruction, the shape of the gating window is critical since it determines the trade-off between undersampling and motion artifacts [66].

It is inevitable, however, to observe motion artifacts with a finite gating window due to residual motion [122]. In some difficult circumstances, such as when the patient is unable to hold breath or in the presence of arrhythmic motion, motion artifacts are more severe [136]. To improve this aspect of ECG-gated reconstruction methods, motion compensation strategies are proposed [64, 72, 122, 128, 136, 137].

The gated MC methods typically parameterise the motion as a 2D geometric transformation [64, 72, 113, 128]. Two-dimensional elastic [113, 137], a multiscale scheme of 2D affine and 2D B-spline [72,128], and 2D translation [64] are employed. The estimation of parameters are carried out by intensity based [72,128] or feature based (e.g. centrelines) [113] registration between the forward projections of the ECG-gated reconstruction and X-ray images. The estimated transformation is applied on the projection images and these transformed images are used for the final MC reconstruction. In general, these methods compute the reconstruction and perform motion compensation in an iterative manner to reduce the effect of motion in the final reconstructions [128,137]. Starting with a small gating windows and gradually increasing the size of the window as iterations progress is shown to be a reasonable strategy to deal with the undersampling artifacts and motion at the same time [128].

As an alternative to 2D geometric transformation, Rohkohl *et al.* [136] employed 3D+t affine transformation to parameterise the residual motion. In particular, a set of temporal points are selected and assigned a 3D affine transform, from which the 3D affine transformation for the remaining time points are interpolated. The parameters of the affine transforms are estimated altogether and jointly with the gated reconstruction.

2.2.3.5 Specialised Tomographic Reconstruction Algorithms

The fundamental tomographic reconstruction algorithms discussed in Section 2.2.3.1 mainly deal with the reconstruction of conventional CT. These algorithms are generally unsuitable for high contrast non-stationary coronary artery reconstruction because these may cause artifacts due to sparse high contrast vessels or undersampling due to gating. Moreover, modifications to these algorithms are required if motion compensation is intended. As a result, several specialised tomographic reconstruction algorithms are adapted from these basic algorithms.

Analytical FDK reconstruction algorithm is modified such that it copes with the undersampling due to retrospective gating [71, 127]. A weighting factor is introduced to counteract the non-equidistant angular sampling [127]. Rohkohl *et al.* [71] observed actual low intensity voxels receive high contributions from some projection images, and this leads to streak artifacts. Thus, a novel weighting is devised to reduce the highest and lowest contributions for a voxel.

Some studies investigated the necessary modifications to FDK in order to convert it into a MC method. Schäfer *et al.* [66] demonstrated how to incorporate motion into an analytical FDK reconstruction formulation. Their new formulation suggests that the filtering and back-projection steps must take the estimated motion vector field into account. However, the formulation does not take into account the effect of the motion vector field on the filtering in their implementation. In [63, 135], the same MC-FDK formulation is used without ignoring the filtering step. This formulation is well-suited to the problems where motion and reconstruction are jointly estimated. Specifically, MC-FDK is inserted into an objective function and used multidimensional optimisation to find the motion parameters and the reconstruction iteratively.

Iterative algebraic reconstruction algorithms are reformulated such that they benefit from sparse structure of the coronary arteries. Instead of directly solving the forward projection equations, L1 norm of the reconstruction is minimised with the forward project equations used as constraints [121, 129, 130]. By introducing a quadratic perturbation term, the minimisation problem can be approximated and efficiently solved via an iterative scheme, which is akin to the conventional ART [130]. Intuitively, nonzero constraint of original ART is relaxed and the solution space is enriched by addition of new subspaces [121]. This effect is mainly due to a voxelwise thresholding in the new formulation. Therefore, the algorithm is called thresholded ART (TART). Hansis *et al.* [121] proposed simultaneous TART (START) technique following the similar changes to convert ART to SART. Recently, Liu *et al.* [131] combined START with a novel background removal technique (Section 2.2.3.6).

Incorporation of the motion into iterative algebraic reconstruction formulation is studied in [120]. The authors showed that the forward projection matrix can be represented such that it depends on the estimated motion vector field. Their formulation states that the entries of the forward projection matrix are given by the volume of the intersection of the X-ray beam with the deformed voxel. After calculation of the forward projection matrix, any iterative algebraic technique can be utilised for the reconstruction. A similar formulation with a generic image model and X-ray lines are presented in [119]. Calculation of forward projection matrix is computationally expensive and approximations are made [119, 120].

Other methods based on joint estimation-reconstruction or iterative statistical reconstruction algorithms generally employ well-known energy minimisation algorithms. These algorithms are used without any modifications, however we mention these algorithms in this section for completeness. Alternatives for energy minimisation include gradient descent [119], stochastic gradient descent [134,136], L-BFGS-B [63, 135], separable paraboloidal surrogates (SPS) [124, 125, 138], and block sequential regularised expectation maximisation (BSREM) [123, 139].

2.2.3.6 Background Removal

X-ray coronary angiography not only includes coronary arteries but also background structures such as spine, ribs or diaphragm. These background structures may cause truncation errors because they are not visible in all projection images due to field of view [64]. In addition, the background structures may hinder the use of sparsity as a prior information [121]. As a result, most of the tomographic reconstruction methods require background removal from X-ray images as a preprocessing or an intermediate step.

Simple image processing techniques are commonly utilised for background removal. The most popular choice is to apply a top-hat filter [140] to suppress the background [113,119,121,122,131,136]. A good suppression can be achieved, however the size of the filter may effect the results [131]. On the other hand, some segmentation based background removal algorithms are proposed [64, 72, 123–125]. These methods first segment the coronary arteries from X-ray images and remove corresponding pixels. These pixels are filled with intensity value estimates from neighbouring background structures to obtain a background image. Hysteresis thresholding of tubularity image [64, 123], thresholding of top-hat filtered image [72, 124], and level set based segmentation [125] are employed. To fill the removed pixels, morphological closure [64,123] and image inpainting [125] are used.

Some reconstruction methods perform background subtraction during the reconstruction. In [63,135], a thresholded reference reconstruction is integrated into reconstruction formulation to reduce the effect of the background structures on the optimisation. On the other hand, [131] proposed to segment intermediate reconstruction of the iterative reconstruction algorithm and used forward projections of the segmentation to suppress background structures on the X-ray images.

The background is generally suppressed or subtracted from the X-ray projection images. This strategy is problematic for iterative statistical reconstruction algorithms since the distribution of the subtraction image does not follow the original assumption [123]. In such cases, integration of background estimation into statistical model improves the reconstruction quality [123].

2.2.3.7 3D+time Tomographic Reconstruction

The simplest way to obtain 3D+t tomographic reconstruction is to reconstruct for a number of time points independently [127,137]. However, it may be impossible to attain the same level of accuracy in different time points due to several factors (e.g. residual motion related to gating window size). In addition, the motion of the arteries can not be studied quantitatively [141]. To overcome these limitations, [141] proposed a strategy to exploit the motion estimated for a MC reconstruction method. Because the parameterisation of the motion is from arbitrary time points to a reference time points, an energy minimisation is proposed to inverse the estimated motion vector field. Inverse motion vector field is used to transform the best-quality reconstruction to the other time points. Unlike this strategy, the methods that perform joint reconstruction and motion estimation can directly deliver the 3D+t reconstruction result [119].

2.3 Evaluation Methods for Coronary Artery Reconstructions

Comparison between different types of the coronary artery reconstruction methods is difficult to achieve due to diversity of the acquisition protocols, specific requirements for the method (e.g. ECG, calibration, user interaction), and especially the lack of standard dataset and performance metrics. Nevertheless, common evaluation types (Section 2.3.1), phantom datasets (Section 2.3.2) and evaluation metrics

(Section 2.3.3) can be identified from the relevant literature to provide insight into the efforts towards a standardised quantitative comparison.

2.3.1 Evaluation Type

Three main groups of evaluation types can be distinguished: qualitative results, quantitative with phantom experiments, and quantitative with experiments on clinical patient data (Table 2.3).

The methods with qualitative evaluation visually compare the results with the results from other methods to provide evidence of the feasibility of the method. These methods are rare in the literature, especially within the journal publications. Further assessment of these methods are required to determine their strengths and weaknesses. Quantitative evaluations are performed by experiments employing either phantom data or clinical patient data.

2.3.2 Phantom Datasets

The ground truth required for the validation is not directly available for the reconstruction problem. One way to address this issue is to utilise physical and software phantoms where the ground truth is known.

Physical phantoms are advantageous in terms of exposing the reconstruction methods to the practical limitations of image acquisition. However, they tend to be limited to simple motion models, since it is hard to imitate the complex combination of cardiac and respiratory motion. In addition, ground truth information must be extracted from a stationary reconstruction of the phantom usually based on manual or semi-automatic image segmentation.

Several physical phantoms with different levels of complexity have been used. Wire [78, 87] and guide-wire [88] phantoms are primitive examples. A 3D-printed static bifurcation and stenosis phantom is used in [92]. The ground truth is determined from the geometric description of the object. In [93], a stenotic coronary artery phantom is used. A static coronary artery phantom with realistic topology is used in [96]. The phantom is scanned with multislice CT (MSCT) and segmented to find the ground truth centrelines. Shechter *et al.* [53] used contrast filled tubes over a compliant latex balloon to mimic the motion. The motion is controlled with mechanical inflation of the balloon. The ground-truth is obtained by segmenting a gated multislice MR of the object and identifying the temporal correspondences between ground-truth and X-ray acquisition. A similar artificial heart and coronary phantom is proposed in [63, 135]. The authors placed tubular structures filled with contrast over an elastic material filled with water. The cardiac motion is controlled with a pump that pushes water in an out, and the respiratory motion is controlled with specialised hardware. Jandt *et al.* [102] used a commercially available complex chest phantom [142].

Software phantoms offer flexible environments for the reconstruction experiments. These phantoms can simultaneously take into account several factors such as the complex topology of vessels, cardiac and heart motions. However, imaging geometry and physics of image acquisition are often simplified.

Lorenz *et al.* [143] built a software phantom from a mean model of the coronary artery trees adapted from the clinical information provided in [144]. The motion of the arteries are included using affine transformations between cardiac phases [66]. Yang *et al.* [145, 146] built a phantom from MSCT data to obtain a more realistic results. They segmented the coronary arteries from MSCT and set the segmented voxel values to a high value to simulate contrast injection. Another possibility is to exploit the coronary artery anatomical model in the 3D+t XCAT phantom [147]. Fung *et al.* [148] generated more complete anatomical model for XCAT, based on morphometric and physiological rules. Rohkohl *et al.* [149] used XCAT phantom to generate realistic X-ray rotational angiography images. In fact, this work constitutes the first attempt to define a standardised quantitative comparison platform. The projection images and relevant additional information are publicly available. Any voxelized reconstruction result can be submitted to the platform for evaluation and ranking.

2.3.3 Evaluation Metrics

The reconstruction results are quantitatively assessed via evaluation metrics measuring the similarity of the reconstruction and the ground truth. Depending on the reconstruction method and the ground truth information various evaluation metrics have been proposed.

Evaluation metrics for model-based reconstruction methods are based on ground truth centreline. To emphasise robustness of the method against foreshortening, the difference between the length of the ground truth and reconstructed centreline is typically preferred for the experiments with wire phantom [78,88,89]. Angles of specific bifurcations are also used to define an error measure [89,94]. Apart from these metrics, the most common metrics are 2D reprojection error and 3D space error. The 2D reprojection error is used to quantitatively evaluate the performance in the experiments using clinical X-ray angiography images. It is defined using the Euclidean distance between the manually segmented ground truth centrelines from the X-ray images and forward projection of the reconstructed arteries onto the 2D detector plane. However, it is demonstrated in [80] that 2D reprojection error does not correlate well with the 3D space error. Therefore, the 2D reprojection error must be calculated from projection angles that are not included in the reconstruction or favourably supported by appropriate 3D evaluation metric. The 3D space error is used in the experiments where the 3D ground truth is available and is generally considered most conclusive centreline based metric. It is simply defined using the 3D Euclidean distance between the reconstruction and the ground truth.

Surface or attenuation coefficient based metrics are proposed for tomographic reconstruction methods. Mean radius error [135] or mean relative radius error [113,121,131] are calculated from the planes whose normal is the ground truth centreline. Another metric is defined as the fraction of the energy (integral of voxel values) located inside the ground truth surface [113]. Similar to this metric, RMS error or MSE of voxel values over whole volume or near coronary artery centrelines are employed [66,121,123,124,137]. These attenuation value metrics are reasonable indicators of the contrast and artifact in the resulting reconstruction. Another way of assessing the image artifacts is to employ a noise estimator [72]. One popular choice for assessment is to compare a thresholded reconstruction with the binary ground truth. Recall rate [105] or Dice coefficient [125] are utilised. In [149], a set of thresholds are used to convert reconstruction into binary volumes and the maximum Dice coefficient is assigned as the quality metric. This metric can work with modelling based reconstructions if the voxelization of the reconstruction is supplied.

There is also some interest in eliminating necessity of having a ground truth. For this purpose, sharpness metric is adapted in [72,150]. The centreline is semi-automatically extracted from the reconstructed image and intensity profiles perpendicular to the centrelines are computed. The metric is defined as the inverse of the average distance between the point of 80% and 20% decrease along the intensity profiles. An implementation of this metric is available as a part of a multi-modality 3D coronary artery reconstruction evaluation software [150].

2.4 Discussion and Conclusion

During the last decade, healthcare has witnessed tremendous advances in the coronary artery imaging technologies. Three main directions of development efforts can be distinguished: i) development of non-invasive diagnostic imaging technologies, such as MRA and CCTA, ii) development of non-invasive interventional technologies, such as C-arm CBCT, and iii) development of invasive interventional technologies, such as IVUS, OCT and X-ray coronary angiography. In the current situation, there is a competition between some of these imaging techniques to determine the most effective areas of use for particular imaging technology. However, it is clear that no single imaging technique can overthrow the others, since they all have different advantages and limitations. Therefore, it is crucial to identify the potential of the each imaging modality and to dedicate imaging and clinical research to each of those to improve all technologies simultaneously.

Advances in the non-invasive imaging modalities do not necessarily result in a decline of the invasive technologies. However, several aspects of clinical decision making, which now depends on X-ray coronary angiography and reconstructions obtained from it, can be effectively handled by a more appropriate imaging modality. The main competitor of X-ray coronary angiography is CCTA. It is anticipated that the CCTA will be the dominant imaging modality for the selection of patients for PCI and the intervention planning due to its non-invasiveness. However, several important factors must be considered before adoption of this technology, such as patient radiation dose, practice guidelines and financial issues [5]. In this regard, X-ray coronary angiography is an established imaging modality, and it is expected to remain as the main imaging modality for the guidance during the interventions. In order to fully exploit X-ray coronary angiography capabilities, 3D/3D+t reconstruction from X-ray coronary angiography should make its way to the intervention room.

Reconstruction from X-ray coronary angiography can facilitate PCI in several ways. In fact, 3D/3D+t reconstructions are progressively being integrated into

PCI. Optimal view selection using reconstructions is a remarkable example of these integration efforts. Optimal views obtained without additional radiation or contrast can help with the stent positioning [22, 151]. In a similar fashion, tomographic reconstructions can be used to simulate intracoronary images to provide further guidance for stent positioning [114]. Furthermore, live overlay of the reconstruction on the fluoroscopy images can provide navigational guidance and possibly lead to a reduction in the contrast material use [51]. In the near future, dynamic reconstructions and holographic imaging can provide a truly 3D display for the understanding of the spatial structure of the coronary arteries.

Fusion of different imaging modalities to exploit supplementary information is another promising direction for the future of X-ray coronary angiography. In this context, reconstructions from X-ray coronary angiography can be utilised instead of raw images. Extracted information from diagnostic CCTA scans can be overlaid with reconstructions to bring the pre-operative planning into the cath-lab [34]. Fusion of reconstructions with IVUS or OCT can provide useful information concerning the morphological information about the stenosis and wall characteristics [35]. Moreover, combination of TEE with 3D+t reconstructions can supply valuable soft-tissue information [152]. Most importantly, information from functional imaging techniques must be fused with the anatomical information of the reconstructions. This is one of the directions that requires a special attention in the future.

An intriguing direction for the future research is the investigation of the tomosynthesis capability of the existing X-ray coronary angiography systems for high-contrast vascular structure reconstruction [153]. In fact, this can be considered the natural next step for tomographic coronary artery reconstruction from extended rotational X-ray angiography. Successful results can lead to reduction in the radiation dose and may result in the change of the acquisition protocol, analogous to the transition from conventional to (dual-axis) rotational angiography.

Novel and robust clinical tools are required to strengthen X-ray coronary angiography's position inside cath-lab. Improvements on virtual FFR estimation [43–46] or virtual stenting [154] could make these technologies available for intraoperative decision making. Real-time simulation of deployment of stent deployment and computation of the resulting hemodynamic changes by the help of 3D/3D+t reconstructions can be set as the next targets for clinical tool development.

To achieve these ambitious goals, several aspects of the current reconstruction methods must be reconsidered. First, the manual interaction required for most of the modelling based reconstructions hinders clinical translation of these methods for real-time processing (Table 2.1). Almost automated methods are essential to make reconstruction technology as an irreplaceable part of cath-lab. Second, the time requirement of the methods should be reduced to the order of seconds by the help of modern parallel computing opportunities (Table 2.3). The recent progress on this direction is encouraging and shows the feasibility of online processing inside cath-lab [22]. Third, 3D+t reconstruction methods with reasonable time requirements should be devised to fully exploit the capabilities of X-ray coronary angiography. Finally, a grand challenge could be organised to be able to overcome the lack of comparability in 3D/3D+t reconstruction research. Initial endeavour to generate a publicly available database for comparison [149] is a notable step toward this direction. A broader quantitative evaluation should involve validation by appropriate metrics capable of providing 3D/3D+t errors on three possible levels, namely, software phantom, physical phantom and clinical images.

Table 2.1: Overview of Model-based Coronary Artery Reconstruction Methods from X-ray Angiography: See list of abbreviations at the bottom.

	Reference	Type	ECG	Breath -hold	Additional Input	Calibration	3D Reconstruction	Multi-view	Lumen surface	4D
TOP-DOWN	[84]	BA	-	+	CLs (2)	+	Fourier deformable model with PEE	-	-	+
	[78]	BA	+	+	CLs (2)	+	ACM with PEE	-	-	-
	[83]	SA	N/A	N/A	Corresponding 2D points (2)	Opt. of ext. params	Calibration opt. followed by ACM with PEE and temporal energy	-	-	+
	[80]	SA	+	N/A	CLs (2-5)	+	ACM with BPEE	+ (2-5)	+ (2-5)	-
	[81]	SA	+	N/A	CLs (2)	Opt. of ext. & int. params	ACM with BPEE & calibration opt. iteratively	-	+ (N/A)	-
BOTTOM-UP	[88]	SA	+	N/A	CLs (2)	Opt. of ext. params	Calibration opt. followed by epipolar matching + triangulation	-	+(1)	-
	[87]	BA	-	N/A	CLs (2)	Opt. of ext. params	Calibration opt. followed by epipolar matching + triangulation	-	-	-
	[89]	SA	+	N/A	CLs (2)	Opt. of ext. params	Calibration opt. followed by epipolar matching + triangulation	-	+(1)	+
	[53]	BA	-	+	CLs (2)	+	Used [90]	-	-	+
	[93]	RA	+	+	CLs (Multi, N/A)	+	Epipolar matching + triangulation	-	+ (Multi, N/A)	-
	[94]	SA	+	N/A	Corresponding 2D points (2)	Opt. of ext. params	Calibration opt. followed by epipolar matching + triangulation	-	+ (8)	-
	[91]	BA	-	-	CLs (2)	-	Reliable point matching & bundle adjustme, iteratively	-	-	-
	[100]	RA	+	+	-	+	Segment from backprojected vesselness response	+ (5-9)	-	-
	[102]	RA	+	+	-	+	Used [100]	+ (5-9)	+ (5-9)	+
	[92]	SA	+	N/A	CLs (2)	-	Epipolar matching & bundle adjustment, iteratively	-	+(2)	-
	[96]	RA	+	+	CLs (4-5)	+	Graph-cut based sparse stereo	+ (4-5)	+(1)	-
	[97]	SA	+	N/A	CLs (3)	+	Graph-cut based sparse stereo	+ (3)	-	+

List of abbreviations:
ACM = active contour model; BA = Biplane X-ray angiography; BPEE = back-projective (3D) external energy; CL = Centreline; ECG = Electrocardiogram; ext. = extrinsic; int. = intrinsic; Opt. = Optimization; param = parameter; PEE = projective (2D) external energy; RA = Rotational X-ray angiography; SA = Standard X-ray angiography; (#) = Number of X-ray images to reconstruct; N/A = not available

Table 2.2: Overview of Tomographic Coronary Artery Reconstruction Methods from X-ray Angiography: See list of abbreviations at the bottom.

	Reference	ECG	Breath -hold	Acquisition protocol	Motion Compensation			Reconstruction
					Motion Model	How obtained	How applied	
GATED	[130]	N/A	N/A	N/A	-	-	-	TART
	[121]	+	+	180°, 7.2 s, N/A, 30 fps	-	-	-	START
	[131]	+	N/A	180°, N/A , N/A , N/A	-	-	-	START with BR
GATED & MC	[72]	+	+	N/A, 5 s, (133), N/A	2D affine and 2D B-spline	Registration between projection of initial reconstruction and projection images	Apply deformations to projection images	Artifact reduced FDK
	[137]	+	+	180°, 7.2 s, N/A, 30 fps	2D elastic warping	Registration between projection of initial reconstruction and projection images	Apply deformations to projection images	START
MC	[120]	N/A	-	120°, N/A, (100), N/A	N/A	N/A	Incorporate MVF into ART formulation	Additive Art
	[64]	-	-	200°, 5 s, N/A, 30 fps	4D B-spline	Propagation of 3D centerline construction	Incorporate MVF into ART formulation	Additive Art
	[66]	+	+	240°, 8 s, (200), N/A	N/A	N/A	Incorporate MVF into FDK	MC FDK
	[121]	+	+	180°, 7.2 s, N/A, 30 fps	2D elastic warping	Registration between projection of initial reconstruction and projection images	Apply deformations to projection images	FDK
	[135]	+	-	200°, N/A, (133), N/A	4D B-spline	Jointly with the reconstruction	Incorporate into FDK formulation	Gradient based energy minimization

List of abbreviations:
ART = Algebraic reconstruction technique; BR = Background removal; FDK = Feldkamp-Davis-Kress algorithm; fps = frame per second; MC = Motion compensated; MVF = Motion vector field; START = Simultaneous thresholded algebraic reconstruction technique; TART = Thresholded algebraic reconstruction technique; (#) = Number of X-ray images; N/A = not available.

Table 2.3: Overview of Evaluation Types for Coronary Artery Reconstruction from X-ray Angiography Methods: See list of abbreviations at the bottom.

	Reference	Hardware	Time/Additional Info	Type	No	Std. of Reference	Metric
Qualitative	[120]	N/A	60 min	Pat	1	N/A	N/A
	[130]	N/A	N/A	s - Pat	N/A - N/A	AT - AT	N/A - N/A
	[64]	N/A	40 min / 256^3	s - Pat	1 - 2	AT - AT	N/A - N/A
Quantitative: synthetic or physical phantom data	[87]	N/A	8-9 min	p - Pat	2 - 2	AT - AT	Inter/Intra var. - Inter/Intra var.
	[78]	N/A	N/A	s - p - Pat	1 - 1 - 5	GT, AT - N/A - N/A	Length - N/A - N/A
	[93]	N/A	N/A	p - A	2 - 1	GT - N/A	3D rprj - N/A
	[94]	N/A	N/A	s	10	GT	3D rprj, Angle
	[102]	N/A	N/A	s - p - A - Pat	1 - 1 - 1 - 2	GT - GT - N/A - N/A	3D rprj - Radius - N/A - N/A
	[66]	3.2GHz AMD Opteron, 8GB	7-80.7 min / 256^3-512^3	s	1	GT	Voxel err. near CL
	[113]	2.8GHz AMD Opteron, N/A	5.4-57.9 min / 0-60% gating window	s - Pat	1 - 15	GT - N/A	Radius, Energy inside GT - N/A
	[121]	N/A	N/A	s - Pat	1 - 3	GT - N/A	Radius, Energy inside GT, Stenosis degree - N/A
	[137]	N/A	N/A	s - Pat	1 - 4	GT - AT	RRE, Total voxel err., Voxel err. near CL - N/A
	[135]	NVIDIA Quadro FX 5800	3 min / 256^3	s - p - Pat	1 - 1 - 3	GT - GT - AT	Radius - Radius - N/A
	[72]	2.53GHz Intel Xeon E5540, 16GB NVIDIA Quadro FX 5800 GPU	N/A	s - Pat	1 - 6	GT; AT - AT	MMO; N/A - Noise level, VS
	[131]	Intel i5-3210	218-350 s / $\sim 256^3$	s	1	GT; AT	MMO, RRE; N/A
Quantitative: real patient data	[88]	Indigo2 R10000, 128MB	< 10 min	p - Pat	1 - 40	GT - GT	Length - 2D rprj
	[84]	1.2GHz AMD Athlon, 256MB	5 s	Pat	14	GT	2D rprj
	[89]	Indigo2	1.0 min	s - p - Pat	N/A - N/A - 40	GT - GT - GT	Curvature, Torsion - Length, Angle - 2D rprj
	[53]	0.75-1GHz Intel Pentium III	155 min / per cardiac phase	p - Pat	1 - 5	GT - GT	3D rprj - 2D rprj
	[91]	N/A	N/A	s - Pat	2 - 2	GT - GT	2D, 3D rprj - 2D rprj
	[92]	3.2GHz Pentium IV, 1GB	4.1-9.6 s	p - Pat	1 - 5	GT - GT	3D rprj, Radius - 2D rprj
	[100]	AMD Opteron 2220	4 s	s - Pat	1 - 17	GT - ES(6)	3D rprj - N/A
	[83]	AMD Athlon X2 4000+, 1GB	0.21 min / per cardiac phase	Pat	5	GT	2D rprj
	[96]	2.13GHz Intel Pentium M	12 s	p - A - Pat	1 - 1 - 11	GT - GT - GT	2D, 3D rprj - 2D rprj - 2D rprj
	[80]	Intel i7-2600, 16G	N/A	s - Pat	1 - 6	GT - GT	2D, 3D rprj - 2D rprj
	[81]	Intel i7-2600, 16G	N/A	s - Pat	6 - 8	GT - GT	2D, 3D rprj - 2D rprj
	[97]	3.4GHz Intel i7-3770, 8GB NVIDIA GTX-780 GPU	3 s	s - Pat	1 - 7	GT - GT	2D rprj - 2D rprj

List of abbreviations:
A = Animal data; AT = Alternative technique; err. = error; ES(#) = Expert score, # experts; GT = Ground truth; MMO = Maximum mean overlap; p = Physical phantom; Pat = Patient data; RRE = relative radius error; s = Software phantom; VS = Vessel sharpness; 2D rprj = 2D reprojection error; 3D rprj = 3D reprojection error; N/A = not applicable/available.

Chapter 3

Preliminaries

This short chapter covers the fundamental aspects of the reconstruction methods presented in Chapters 4-6, namely X-ray acquisition geometry/calibration, and handling of cardiac/respiratory motion.

3.1 X-ray Acquisition Geometry and Calibration

Acquisition geometry for X-ray angiography is typically described by three distinct coordinate systems, namely the X-ray source, the X-ray detector, and the patient. A projection function, $\Theta : \mathbb{R}^3 \to \mathbb{R}^2$, defines the projective mapping between patient and X-ray detector coordinate systems. This function can be defined using projective camera models that are common in computer vision [52]. Particularly, the perspective and weak-perspective camera models can be employed.

For the perspective model, the projection of a point in the patient coordinate system is given by the intersection of a line passing through this point and the X-ray source location. The projection function is defined as

$$\Theta(\boldsymbol{y}) = \begin{bmatrix} \boldsymbol{q}_1^T[\boldsymbol{y}\ 1]^T / \boldsymbol{q}_3^T[\boldsymbol{y}\ 1]^T \\ \boldsymbol{q}_2^T[\boldsymbol{y}\ 1]^T / \boldsymbol{q}_3^T[\boldsymbol{y}\ 1]^T \end{bmatrix}, \tag{3.1}$$

where $\boldsymbol{y} \in \mathbb{R}^3$ is a 3D point, and $\{\boldsymbol{q}_i^T\}_{i=1}^3$ are the rows of the projection matrix $\boldsymbol{Q} \in \mathbb{R}^{3\times4}$. Perspective projection is a nonlinear transformation, since the scaling factor depends on object's distance from the X-ray detector.

The weak-perspective model is known to be a reasonable approximation to the perspective model when the depth of the object is small compared to distance from camera, and the field of view is small [52], both of which are valid assumptions for X-ray angiography. The projection function is given as

$$\Theta(\boldsymbol{y}) = \begin{bmatrix} \boldsymbol{q}_1^T\boldsymbol{y} \\ \boldsymbol{q}_2^T\boldsymbol{y} \end{bmatrix} \tag{3.2}$$

where $\{\boldsymbol{q}_i^T\}_{i=1}^2$ are the rows of projection matrix $\boldsymbol{Q} \in \mathbb{R}^{2\times3}$.

Modern X-ray angiography systems give access to calibration information for specific angiography protocols (such as rotational angiography), from which the projection matrices can be obtained. The methods presented in this thesis (Chapter 4-6) assume that the X-ray angiography images are collected using a calibrated rotational angiography system, thus the projection matrices are readily available. Moreover, the Jacobian matrix of the projection function, $\frac{\partial \Theta(\boldsymbol{y})}{\partial \boldsymbol{y}} \in \mathbb{R}^{2\times 3}$, is required for the reconstruction formulations in Chapter 4 and 6. The Jacobian matrix for the perspective projection model depends on the point to be projected and given as

$$\frac{\partial \Theta(\boldsymbol{y})}{\partial \boldsymbol{y}} = \frac{1}{\boldsymbol{q}_3^T[\boldsymbol{y}\ 1]^T} \begin{bmatrix} (q_{11}\boldsymbol{q}_3^T - q_{31}\boldsymbol{q}_1^T)[\boldsymbol{y}\ 1]^T, & (q_{21}\boldsymbol{q}_3^T - q_{31}\boldsymbol{q}_2^T)[\boldsymbol{y}\ 1]^T \\ (q_{12}\boldsymbol{q}_3^T - q_{32}\boldsymbol{q}_1^T)[\boldsymbol{y}\ 1]^T, & (q_{22}\boldsymbol{q}_3^T - q_{32}\boldsymbol{q}_2^T)[\boldsymbol{y}\ 1]^T \\ (q_{13}\boldsymbol{q}_3^T - q_{33}\boldsymbol{q}_1^T)[\boldsymbol{y}\ 1]^T, & (q_{23}\boldsymbol{q}_3^T - q_{33}\boldsymbol{q}_3^T)[\boldsymbol{y}\ 1]^T \end{bmatrix}^T , \tag{3.3}$$

On the other hand, the Jacobian matrix simply equals to the projection matrix for the weak-perspective projection, $\frac{\partial \Theta(\boldsymbol{y})}{\partial \boldsymbol{y}} = \boldsymbol{Q}$.

In Chapter 4 and 6, we take advantage of both camera models by firstly computing an approximate reconstruction using weak-perspective camera model, and then refining it with a perspective camera model. The linearity of the weak-perspective camera model enables us to obtain closed-form solutions for 3D reconstruction, whereas the perspective camera model requires numerical optimisation. In Chapter 5, only the perspective camera model is used to model the X-ray acquisition geometry.

3.2 Handling of Cardiac and Respiratory Motion

One important aspect for a coronary artery reconstruction method is handling of respiratory and cardiac motion. Throughout this thesis, it is assumed that X-ray images are acquired during breath-hold, thus the breathing motion is significantly reduced. On the other hand, retrospective gating strategies are commonly employed to eliminate cardiac motion in the X-ray images.

In this thesis, retrospective ECG gating is utilised for the reconstruction methods proposed in Chapter 4 and 6. Every X-ray image is thus assigned a cardiac phase using the ECG signal recorded synchronously with image acquisition. Following this assignment, a subset of images, which are close to a reference cardiac time, are selected along with a windowing function to determine a weight for each of the selected images. The end-diastolic or end-systolic cardiac phases are selected as the reference due to minimal motion in these phases [60, 61].

In Chapter 4, a square windowing function which assigns the same weight to all gated images is used. This function selects a subset consisting of 8-9 images out of approximately 130 images. To further reduce the influence of cardiac motion, a nearest neighbour window function is used in In Chapter 6, i.e. only those images that are closest to the reference cardiac phase (3-5 images) are selected.

Chapter 4

Reconstruction of Coronary Artery Centrelines from X-ray Rotational Angiography Using a Gaussian Mixture Model

4.1 Introduction

Although X-ray coronary angiography is considered as the gold standard for the clinical decision making and therapy guidance, it is fundamentally limited, since it can only produce 2D X-ray projection images of moving coronary arteries. It is crucial to provide quantitative 3D/3D+t information to clinicians to improve pre-operative planning and inter-operative guidance. However, reconstruction of coronary arteries remains a highly challenging task due to ill-posedness, intensity inhomogeneity, overlap, foreshortening, and cardiac/respiratory motion [11].

During the last decade, a vast amount of research has been devoted to obtain 3D coronary artery reconstructions from 2D X-ray angiography images. Among these efforts, model-based reconstruction algorithms (modelling) try to generate a 3D model of the coronary arteries, which consists of 3D centreline of the arteries, and, occasionally, vascular lumen. However, most of these methods generally require clean centreline segmentations from 2D X-ray images, which are typically obtained using a manual segmentation tool [78,80,81,89,92]. On the other hand, 2D segmentation of coronary artery centrelines from X-ray angiography images remains as a challenging task due to inhomogeneous intensities, and complex coronary artery topologies with overlap and foreshortening [155]. This shortcoming limits adoption of model based reconstruction methods in the clinical routine. As a solution, a 3D coronary artery reconstruction method should provide some robustness against possible sources of error in the 2D centreline segmentations, such as outliers due to other structures which are also visible in X-ray images.

In this chapter, we propose a novel probabilistic formulation for reconstruction of coronary artery centrelines from Rotational Angiography (RA) based on a Mixture Model (MM) representation of point sets describing the coronary arteries. The main contribution of this chapter is to provide a novel perspective and formulation for model based reconstruction of coronary arteries from RA. Our formulation offers robustness against the outliers in 2D centreline segmentations by employing an additional uniform MM component to model the outliers.

4.2 Literature on Mixture Model-based Point Set Representation

In computer vision, a popular way to represent shapes is to use ordered point sets that are sampled from original shape of the object of interest. However, this basic representation might be problematic for applications operating on these point sets, especially when outliers are present in the point set representations. Iterative Closest Point (ICP) algorithm [156] is a typical example for these kind of shortcomings. To overcome these issue, probabilistic representation of the point sets has been studied in the last decade.

The main idea behind the probabilistic representation of point sets is to consider each point as a probability distribution, whose spatial location corresponds to the mean of the corresponding distribution. In this way, the point set can be represented as a finite mixture model, and the applications involving point sets can be formulated in a probabilistic manner.

The probabilistic point set representation has mainly been studied in the context of point set registration. Chui *et al.* [157, 158] proposed a registration framework capable of handling rigid and non-rigid transformation by representing one point set as a finite mixture model, and finding the best fit to the other point set. Coherent Point Drift (CPD) [159] follows a similar idea but imposes motion coherence [160] on the points to regularise the non-rigid registration. Horaud *et al.* [161] proposed a probabilistic point set based registration method for articulated object that can handle missing data. Another approach is to represent the both point sets as finite mixture models, and minimise the dissimilarity between these distributions to estimate the registration. Different types of dissimilarity measures are used including $L2$ distance [162], Havrda–Charvat–Tsallis divergence [163, 164].

All of the aforementioned registration methods use Gaussian distribution for their point set representations. However, this distribution is known to be sensitive to the outliers in the data [165]. To address this problem, the registration methods often augment their finite mixture model by an additional distribution component to accommodate the outliers [157, 159]. As an alternative, Gaussian distributions can be replaced by robust distributions. To this end, Wang *et al.* [166] proposed to use asymmetrical Gaussian distributions. Ravikumar *et al.* [167] developed a group-wise registration algorithm which uses robust Student's t-distributions.

In medical image analysis, the probabilistic point set representation is utilised for two main applications, namely joint correspondence matching and registration for statistical shape models, and fusion of information from imaging modalities for intra-operative guidance.

Gaussian mixture model based representation has been employed to formulate group-wise rigid [168, 169] and non-rigid [170] registration methods for statistical shape analysis. These methods jointly update the registrations of shapes to a mean shape and the correspondences between the shapes and the mean shape. Recently, Ravikumar *et al.* [167] proposed a rigid group-wise registration strategy using Student's t-mixture models, which provides additional robustness in the presence of shapes with outliers due to segmentation errors.

To fuse the information from CTA images with the coronary artery reconstructions from biplane angiography, Dibildox *et al.* [34] proposed a multi-stage 3D/3D registration approach. The initial rigid registration between point sets are computed using a probabilistic point set representation, and then it is refined by incorporating orientation and bifurcation information. Baka *et al.* [171] enriched the conventional probabilistic point set representation by orientation information. This representation is used to formulate a 2D/3D registration between coronary artery segmentations from CTA images and X-ray coronary angiography for providing intra-operative guidance.

In this and the following chapters, we propose novel methods for coronary artery reconstruction from X-ray rotational angiography images, taking advantage of probabilistic point set representation. Unlike the aforementioned registration methods, which start with a 3D probabilistic point set representation and register it with other 2D/3D point sets, we tackle the reconstruction problem. Specifically, our problem is to estimate the 3D/3D+t probabilistic point set representation of coronary arteries given 2D/2D+t point sets from different views.

4.3 Methods

In this section, we discuss the Gaussian mixture model-based 3D reconstruction method in detail. The reconstruction formulation presented in this section follows the assumptions regarding the X-ray acquisition geometry and retrospective ECG gating explained in Chapter 3.

The main idea of our reconstruction method is to represent 3D coronary artery centrelines as a probabilistic mixture model (MM), which is composed of Gaussian distribution components and an additional uniform distribution. Specifically, our method assumes that the coronary artery centrelines can be described by a set of 3D points. Spatial locations of these 3D points are considered as the means of the Gaussian components to represent the coronary artery centrelines as a MM. In addition, 2D centreline segmentations from retrospectively gated X-ray projection images are assumed to be obtained by a semi-automatic or automatic segmentation method. Intuitively, the MM describes a probability distribution in 3D space, and the points of the 2D centreline segmentations are treated as projections of samples generated from that probability distribution. To accommodate any outlier points in the 2D centreline segmentations, an additional uniform distribution is added to the MM. The configuration is illustrated in Fig. 4.1.

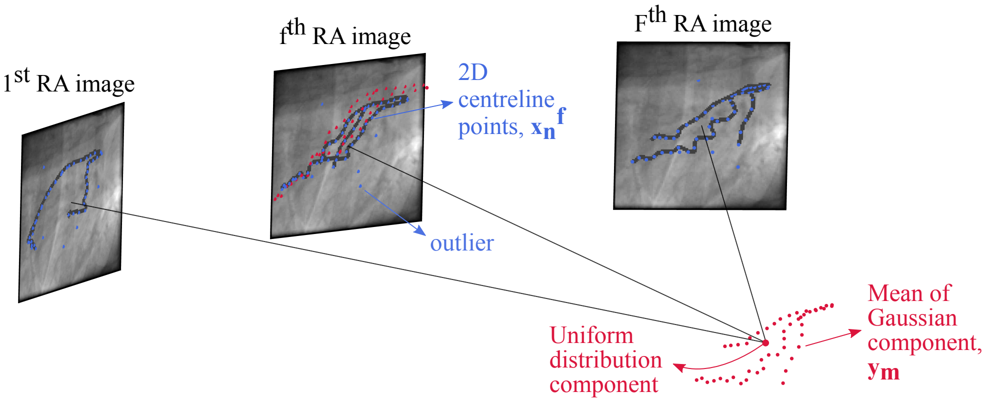

Figure 4.1: Illustration of the reconstruction process: 2D centreline points (blue points on RA images) are segmented from retrospectively gated X-ray RA images. Coronary artery centrelines are described by a set of 3D points (red points in 3D space), whose spatial locations are considered as means of Gaussian components of the MM. The goal of reconstruction is to find the means of Gaussian components that "best" explain the 2D centreline points. The projections of MM components onto RA images (red points on middle RA image) are used to define the likelihood function.

The reconstruction is formulated as maximum-likelihood (ML) estimation of means, isotropic variance, and mixture weights of the components of the MM. The ML solution is computed using Expectation-Maximization (EM) algorithm. Closed form solutions are derived for isotropic variance of the Gaussian components and the mixture weights of all components. As to means of Gaussian components, a closed form solution can be derived if weak-perspective camera model is utilised to describe the acquisition geometry. Numerical optimisation is used when perspective camera model is preferred. Our method takes advantage of both models, initiating from weak-perspective model and, upon convergence, switching to perspective model for refinement.

Two-dimensional centrelines are segmented from F retrospectively gated RA images, and denoted as $\mathbb{X} = \{\boldsymbol{\mathcal{X}}^f\}_{f=1}^{F}$. $\boldsymbol{\mathcal{X}}^f = \{\boldsymbol{x}_n^f \in \mathbb{R}^2\}_{n=1}^{N^f}$ is the set of segmented centreline points for fth RA image, where N^f is the number of 2D centreline segmentation points for fth RA image, and $\boldsymbol{x}_n^f$ is arbitrary single 2D centreline point in fth RA image. Similarly, let $\boldsymbol{\mathcal{Y}} = \{\boldsymbol{y}_m \in \mathbb{R}^3\}_{m=1}^{M}$ denote the set of M 3D points corresponding to the means of the Gaussian components. In addition to the Gaussian components, a uniform distribution is added to the mixture model to allow for outliers in the 2D centreline segmentations (Fig. 4.1).

The goal is to maximise a likelihood function which is given as, $\ln P(\mathbb{X}, \mathbb{Z} | \boldsymbol{\mathcal{Y}}, \boldsymbol{\mathcal{Q}})$, where $\boldsymbol{\mathcal{Q}}$ denote the parameters of the components of MM, namely, isotropic variance of Gaussian components, and mixture weights for all components. $\mathbb{Z} = \{\boldsymbol{\mathcal{Z}}^f\}_{f=1}^{F}$ is the set of latent variables. $\boldsymbol{\mathcal{Z}}^f = \{\boldsymbol{z}_n^f \in \mathbb{R}^{M+1}\}_{n=1}^{N^f}$ is the set of latent variables for the centreline points in fth RA image, where $\boldsymbol{z}_n^f \in \mathbb{R}^{M+1}$ is a binary vector, which has only one non-zero entry. These vectors denote the cluster labels of the 2D centreline points, i.e. if mth component of $\boldsymbol{z}_n^f$ is one, it means that the nth 2D centreline point in fth RA image is generated by the mth component of the mixture model.

If we assume independence of the 2D centreline points in different RA images, and the independence of each 2D centreline point in each RA image, we can write the total probability

$$P(\mathbb{X}, \mathbb{Z} | \boldsymbol{\mathcal{Y}}, \boldsymbol{\mathcal{Q}}) = \prod_{f=1}^{F} P(\boldsymbol{\mathcal{X}}^f, \boldsymbol{\mathcal{Z}}^f | \boldsymbol{\mathcal{Y}}, \boldsymbol{\mathcal{Q}}) = \prod_{f=1}^{F} \prod_{n=1}^{N^f} \prod_{m=1}^{M+1} \left[\pi_m P_m^f\right]^{z_{nm}^f}, \tag{4.1}$$

where π_m denote the mixture weights for the mth mixture component ($\sum_m^{M+1} \pi_m = 1$), and P_m^f is the corresponding probability distribution. Because we have different distributions for Gaussian and uniform components, P_m^f is written as

$$P_m^f = \begin{cases} \mathcal{N}(\boldsymbol{x}_n^f | \Theta^f(\boldsymbol{y}_m), \sigma^2) & \text{if } m = 1 \dots M, \\ 1/\kappa & \text{if } m = M+1, \end{cases} \tag{4.2}$$

where $\Theta^f : \mathbb{R}^3 \rightarrow \mathbb{R}^2$ is the projection function, σ^2 is the isotropic variance of Gaussian components, and κ is the parameter determining the amplitude of the uniform distribution component, which is a free parameter of our formulation. Although, the coronary arteries have a dominant direction, Gaussian distribution with isotropic variance is chosen for three main reasons. First, the estimation of the 3D covariance matrix from 2D projections require computing projection of this matrix in every update iterations and it can be computationally expensive. Second, it will increase the flexibility of the model, making it prone to overfitting. Third, using isotropic covariance forces the model to place Gaussian components at regular intervals to be able to model all the data. This is beneficial when the complete tree is sought from reconstructed point sets.

The goal of the reconstruction is to estimate $\boldsymbol{\mathcal{Y}}$, which can be rewritten as maximising log-likelihood function with respect to the mixture model parameters;

$$\boldsymbol{\mathcal{Y}}^*, \boldsymbol{\mathcal{Q}}^* = \underset{\boldsymbol{\mathcal{Y}}, \boldsymbol{\mathcal{Q}}}{\operatorname{argmax}} \ln P(\mathbb{X} | \boldsymbol{\mathcal{Y}}, \boldsymbol{\mathcal{Q}}). \tag{4.3}$$

The ML estimation of the mixture model parameters can be found using expectation-maximization (EM) algorithm [172]. EM algorithm is an iterative algorithm, which iterates between E and M steps until convergence. Specifically, a lower bound of the function in Eq. (4.3) is maximised with respect to $\boldsymbol{\mathcal{Y}}$ and $\boldsymbol{\mathcal{Q}}$ as

$$\begin{aligned} \boldsymbol{\mathcal{Y}}^*, \boldsymbol{\mathcal{Q}}^* &= \underset{\boldsymbol{\mathcal{Y}}, \boldsymbol{\mathcal{Q}}}{\operatorname{argmax}} \sum_{\mathbb{Z}} P(\mathbb{Z} | \mathbb{X}, \hat{\boldsymbol{\mathcal{Y}}}, \hat{\boldsymbol{\mathcal{Q}}}) lnP(\mathbb{X}, \mathbb{Z} | \boldsymbol{\mathcal{Y}}, \boldsymbol{\mathcal{Q}}) \\ &= \underset{\boldsymbol{\mathcal{Y}}, \boldsymbol{\mathcal{Q}}}{\operatorname{argmax}} E_{\mathbb{Z}} \{ \ln P(\mathbb{X}, \mathbb{Z} | \boldsymbol{\mathcal{Y}}, \boldsymbol{\mathcal{Q}}) | \mathbb{X}, \hat{\boldsymbol{\mathcal{Y}}}, \hat{\boldsymbol{\mathcal{Q}}} \} \end{aligned} \tag{4.4}$$

where $(\hat{\cdot})$ identifies the mixture model parameters from the previous iteration of the EM algorithm, and $E\{\cdot\}$ denotes the expectation. In the E-step of the algorithm, posterior probabilities of latent variables are computed as

$$\begin{aligned}
\gamma^f_{nm} &= E_{z^f_{nm}}\{z^f_{nm} | \boldsymbol{x}^f_n, \hat{\boldsymbol{\mathcal{Y}}}, \hat{\boldsymbol{\mathcal{Q}}}\} \\
&= \frac{\sum_{\boldsymbol{z}^f_n} z^f_{nm} \prod_{j'}^{M+1} \left[\hat{\pi}_{j'} P^f_{j'}\right]^{\boldsymbol{z}^f_{nj'}}}{\sum_{\boldsymbol{z}^f_n} \prod_{k'}^{M+1} \left[\hat{\pi}_{k'} P^f_{k'}\right]^{\boldsymbol{z}^f_{nk'}}}. \\
&= \frac{\hat{\pi}_m P^f_m}{\sum_{m=1}^{M+1} \hat{\pi}_m P^f_m} \qquad (4.5)
\end{aligned}$$

In the M-step, the lower bound is maximised with respect to $\boldsymbol{\mathcal{Y}}$ and $\boldsymbol{\mathcal{Q}}$. Given the posteriors in Eq. (4.5), the lower bound can be written as

$$E_{\mathbb{Z}}\{\ln P(\mathbb{X}, \mathbb{Z} | \boldsymbol{\mathcal{Y}}, \boldsymbol{\mathcal{Q}}) | \mathbb{X}, \hat{\boldsymbol{\mathcal{Y}}}, \hat{\boldsymbol{\mathcal{Q}}}\} = E_{\mathbb{Z}}\{\sum_{f=1}^{F} \sum_{n=1}^{N^f} \sum_{m=1}^{M+1} z^f_{nm} \ln\left(\pi_m P^f_m\right)\} \approx \qquad (4.6)$$

$$\sum_{f=1}^{F} \sum_{n=1}^{N^f} \sum_{m=1}^{M} \gamma^f_{nm} \ln\left(\pi_m \mathcal{N}(\boldsymbol{x}^f_n | \Theta^f(\boldsymbol{y}_m), \sigma^2)\right) + \sum_{f=1}^{F} \sum_{n=1}^{N_f} \gamma^f_{n(M+1)} \ln\left(\frac{\pi_{(M+1)}}{\kappa}\right).$$

Maximising Eq. (4.6) with respect to π_m boils down to solving the following equation:

$$\frac{\partial}{\partial \pi_m}\left[E_{z^f_{nm}}\{z^f_{nm} | \boldsymbol{x}^f_n, \hat{\boldsymbol{\mathcal{Y}}}, \hat{\boldsymbol{\mathcal{Q}}}\} + \lambda\left(\sum_{m=1}^{M+1} \pi_m = 1\right)\right], \qquad (4.7)$$

where λ is the Lagrange multiplier for the constraint $\sum_{m=1}^{M+1} \pi_m = 1$. The solution can be written as

$$\pi_m = \frac{\sum_{f=1}^{F} \sum_{n=1}^{N^f} \gamma^f_{nm}}{\sum_{f=1}^{F} N^f}. \qquad (4.8)$$

Similarly, taking derivative of Eq. (4.6) with respect to σ^2, and setting it to zero, update equation can be written as

$$\sigma^2 = \frac{\frac{1}{2} \sum_{f=1}^{F} \sum_{n=1}^{N^f} \sum_{m=1}^{M} \gamma^f_{nm} \|\boldsymbol{x}^f_n - \Theta^f(\boldsymbol{y}_m)\|^2}{\sum_{f=1}^{F} N^f - \sum_{f=1}^{F} \sum_{n=1}^{N^f} \gamma^f_{n(M+1)}}. \qquad (4.9)$$

Finally, $\boldsymbol{\mathcal{Y}}$, i.e. reconstruction is estimated. Taking partial derivative of Eq. (4.6) with respect to $\boldsymbol{y}_m$, and equating it to zero, we obtain

$$\sum_{f=1}^{F}\sum_{n=1}^{N_f}\gamma_{nm}^{f}\left(\boldsymbol{x}_n^f-\Theta^f(\boldsymbol{y}_m)\right)^T\frac{\partial\Theta^f(\boldsymbol{y}_m)}{\partial\boldsymbol{y}_m}=0. \tag{4.10}$$

For weak-perspective camera model, the Jacobian matrix, $\partial\Theta^f(\boldsymbol{y}_m)/\partial\boldsymbol{y}_m$, is equal to the projection matrix, $\boldsymbol{Q}$. As a result, closed form solution for $\boldsymbol{y}_m$ can be obtained as

$$\left(\sum_{f=1}^{F}\sum_{n=1}^{N^f}\gamma_{nm}^{f}(\boldsymbol{Q}^f)^T\boldsymbol{Q}^f\right)\boldsymbol{y}_m=\sum_{f=1}^{F}\sum_{n=1}^{N^f}\gamma_{nm}^{f}(\boldsymbol{Q}^f)^T\boldsymbol{x}_n^f. \tag{4.11}$$

In the case of perspective camera model, there is no closed form solution for $\boldsymbol{y}_m$, since the Jacobian matrix is a function of the point to be optimised (Section 3.1). Therefore, a numerical optimisation is carried out in the M-step. Any gradient based optimiser can be used as analytical gradient is available (Eq. 4.11). In this thesis, conjugate gradient method is used as the gradient based optimiser. Our method takes advantage of both camera models, initiating from weak-perspective model and, upon convergence, switching to perspective model for refinement.

4.4 Results and Discussion

To quantitatively assess our method, synthetic angiography data and corresponding centreline segmentations at end-diastole were generated using left coronary artery geometry of 4D XCAT phantom [147]. To this end, B-spline curves describing the projection of coronary artery centrelines were sampled 1.0 mm to generate the synthetic centreline segmentations (Fig. 4.2a). This synthetic data was employed to test i) the influence of the number of Gaussian components (M), ii) the effect of number of RA images, and iii) the robustness in the presence of outliers in centreline segmentations.

Our method requires initial values of the mixture model parameters. We set equal mixture weights, i.e. π_m was set to $1/(M+1)$. To initialise the means of the Gaussian components, we selected M points on a regular grid in spherical coordinates placed at the origin of the patient coordinate system (Fig. 4.2b). By adjusting the radial sampling rate, we were able to change the number of Gaussian

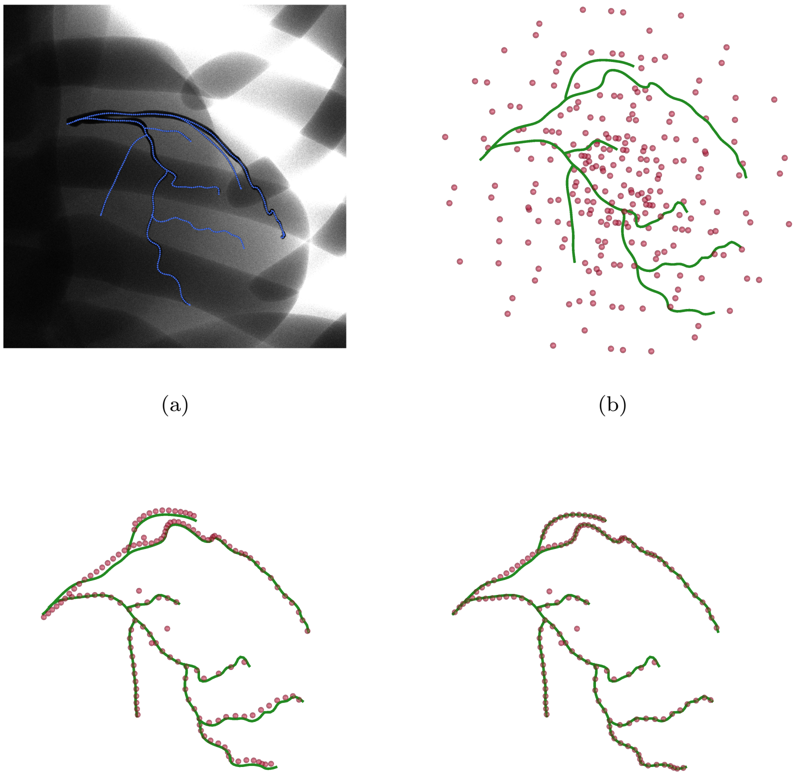

(a) (b)

(c) (d)

Figure 4.2: Progress of the proposed algorithm at different steps: (a) An example of a single gated frame from the synthetic phantom, where the centrelines are shown in blue. (b) Initialisation is conducted with points inside a sphere located at the centre of the patient coordinate system. (c) The reconstruction at convergence with weak-perspective camera model, and (d) the reconstruction at convergence with perspective camera model are shown. The red points correspond to the estimated means of the Gaussian components, whereas the ground truth centrelines are shown in green.

components in the probabilistic model, M. This is an important parameter, since a large M can cause overfitting of the probabilistic model. For all of the phantom experiments M was empirically set to 336, which corresponds to a regular sampling grid at every 30° in azimuth/inclination axis with four regular layers in radial axis (Fig. 4.2b).

Random outlier points were added to the synthetic centreline segmentation fol-

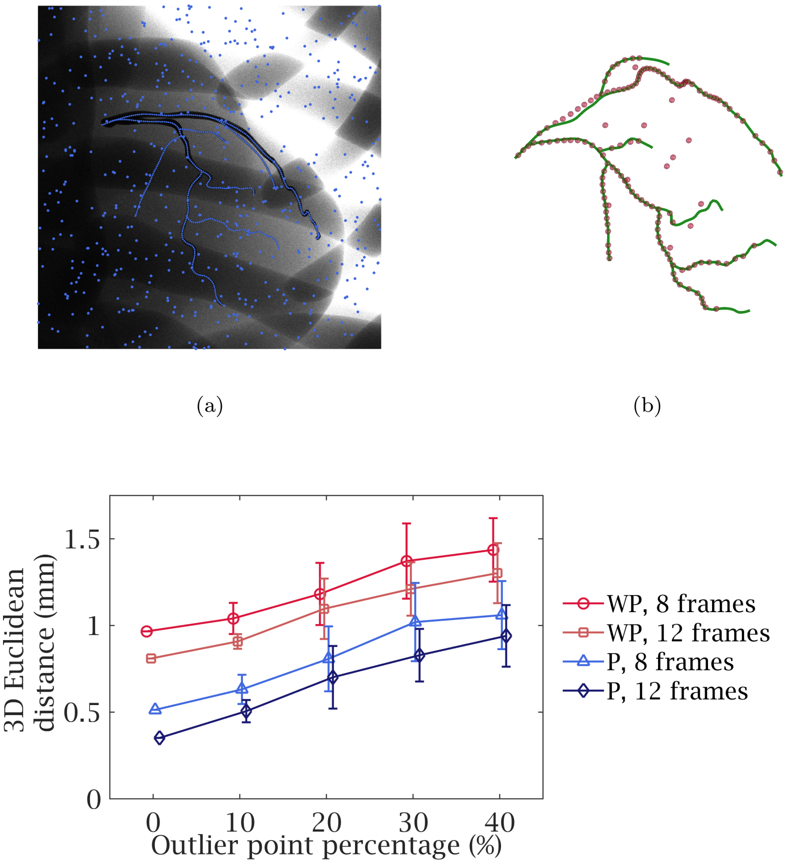

(a)

(b)

(c)

Figure 4.3: Results of the outlier experiment: (a) An example of a single gated frame from the synthetic phantom with outliers (cf. Fig. 4.2a). (b) The reconstruction at convergence with perspective camera model at 40% outlier level (cf. Fig. 4.2d at 0% outlier level). (c) Results of the experiments averaged over 10 runs with different outlier levels (0% to 40%), camera models (weak-perspective, WP or perspective, P) and number of gated frames (8 or 12 frames).

lowing a uniform distribution and were used as input to our algorithm (Fig. 4.3a). Number of additional outliers points was specified as 0% to 40% of the number of inlier points with 10% increments. The reconstruction experiments were repeated ten times in each outlier level to increase generality. Moreover, influence of number of retrospectively gated RA images was also investigated in our experiments. The averages of mean Euclidean distances from the reconstructed points to the closest ground truth centreline point were reported. The results of the outlier experiment are shown in Fig. 4.3. The results indicate that the resulting reconstructions do not deteriorate severely even with a high number of outlier points in 2D segmentations.

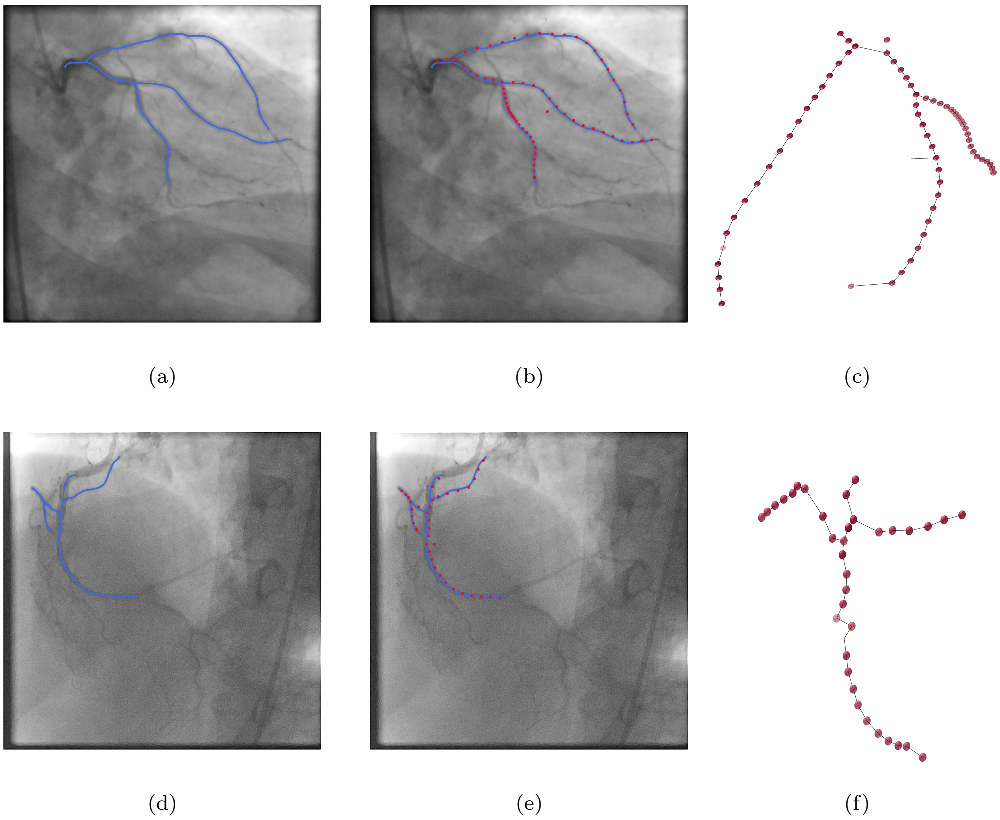
(a) (b) (c)

(d) (e) (f)

Figure 4.4: Results of the experiments with clinical RA data are shown for LCA (first row) and RCA (second row). (a)-(d) Segmented centreline points are shown in blue. (b)-(e) Reconstruction result projected onto the RA image is shown by red points. (c)-(f) The reconstruction at convergence with perspective camera model. The opacity of the points reflect the importance of the component in MM.

To assess the performance of the proposed method in real X-ray RA data, two reconstructions were computed from one LCA and one RCA study. The centrelines from RA images (8 and 9 images for RCA and LCA, respectively), which are temporally close to end-diastole, were segmented using a semi-automatic segmentation tool [173] (Fig. 4.4a and 4.4d). As a post-processing step, reconstructed points are connected to each other by computing minimum spanning arborescence using Edmond's algorithm [174]. Because the ground truth is not available, only qualitative reconstruction results were shown in 3D (Fig. 4.4c and Fig. 4.4d), and in 2D by projecting reconstruction onto RA image (Fig. 4.4a and 4.4b).

The preliminary reconstruction results in real RA data revealed some reconstruction problems near coronary ostium and LCX bifurcation. Incorporation of smoothness prior can lead to better reconstructions in those areas.

In addition, the influence of number of Gaussian components in the probabilistic model, M, is more evident in the real X-ray RA experiments (Fig. 4.5). Because of the residual motion due to imperfect ECG gating or respiratory motion, the X-ray images do not correspond to the same motion state. As a result, some of the mixture components are positioned in 3D space to model the effect of the residual motion, i.e. our mixture model overfits to the data points. In order to alleviate these problem, the number of model points could be reduced by incorporating sparsity priors [169].

Incorporation of both smoothness and sparsity priors, and their influence on the reconstruction results are discussed in Chapter 6.

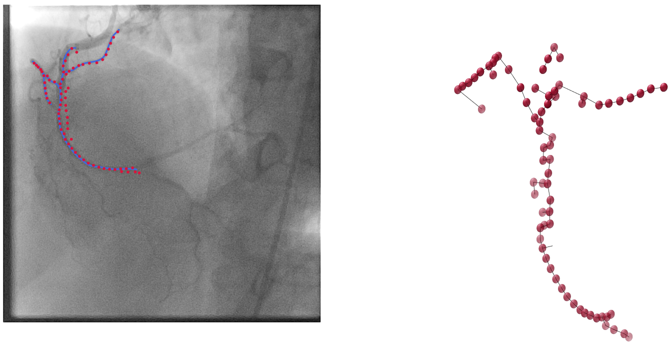

(a) (b)

Figure 4.5: Overfitting due to number of Gaussian components, M: Reconstruction results for RCA is shown after the number of Gaussian components in the mixture model is increased to M=84. (cf. Fig. 4.4e and 4.4f with M=42).

4.5 Conclusion

We propose a method for 3D reconstruction of coronary arteries from X-ray RA with a novel probabilistic perspective. The 3D points describing the coronary centrelines are considered to form a probabilistic MM, from which the 2D centreline points are generated. In our initial experiments, promising reconstruction results are obtained.

The suitability of the proposed MM based representation of the coronary artery centrelines for the reconstruction problem is further investigated in the following two chapters. In Chapter 5, a 3D+t reconstruction formulation is proposed using a similar MM based representation. In Chapter 6, other aspects of the proposed reconstruction method, namely more appropriate component distribution, incorporation of sparsity [169] and spatial smoothness, are discussed.

Chapter 5

Reconstruction of Coronary Artery Centrelines from Rotational Angiography Using a 3D+t Statistical Cardiac Prior

5.1 Introduction

Coronary artery disease (CAD) is a serious condition, responsible for almost 1.8 million deaths in the Europe alone [1]. Current clinical practice for interpretation and assessment of the disease still relies on the anatomical information derived from coronary angiography [175]. However, a considerable amount of 3D information of the coronary arteries is lost during 2D projection. It is also hard to study dynamic variation of coronary arteries through 2D projection images [89]. Therefore, providing a clinician with a quantitative 3D+t description of the arterial tree is of utmost importance to aid the diagnosis of CAD and improve therapy planning and catheter-based interventions.

In recent years, a vast amount of research has been carried out to obtain a 3D/3D+t representation of the coronary tree from medical imagery. Among these methods, a class of methods try to build a 3D symbolic model of coronary arteries, which consists of a 3D centreline and, occasionally, the vessel diameter. Most of the modelling based reconstruction methods uses ECG gating to select two or more (4-5) projections from over a hundred images [96, 100]. Consequently, a considerable amount of acquired information is discarded by these methods. Additionally, obtaining 3D+t reconstruction via ECG-gated reconstruction methods is a tedious task. This is mainly because 3D reconstructions for different cardiac phases must be generated separately. However, not all the segments of the coronary arterial tree are visible in all the rotational angiographic views.

In this chapter, we propose a novel method to reconstruct 3D+t points of coronary arterial trees from rotational X-ray angiography (RA), which generally constitutes the initial step in a coronary artery reconstruction workflow. Our method uses all the images collected during the angiographic study and outputs the 3D+t points of the coronary arteries by utilising a spatiotemporal model of the epicardial surface. Similar to the previous chapter, the method employs a mixture model based representation which implicitly represents coronary arteries using the spatiotemporal statistical model. Thanks to this representation, the reconstruction is formulated as a 2D+t/3D+t Gaussian mixture model based registration between the given 2D artery centreline and the projections of the 3D points of the spatiotemporal model. We validated our method with a software phantom of the left coronary artery tree and a spatiotemporal model of the left ventricular epicardium.

5.2 Methods

Our method assumes that the coronary arteries are attached to and move together with the ventricular epicardium. Therefore, a statistical model of the epicardial surface could implicitly describe the non-rigid structure of coronary arteries if the arterial locations on the model are known. Our method employs a bilinear model of the left ventricle (Section 5.2.1) as the statistical model.

Given 2D points tracked over sequence of X-ray images, we formulate an energy that consists of two terms: namely, a distance and a regularisation term. This energy defines a 2D+t/3D+t Gaussian mixture model (GMM) based registration between the given 2D points tracked over the sequence and the projections of the 3D bilinear model points. By minimising this energy, we find the bilinear model parameters that best describe the observed 2D points. In order to iteratively minimise the energy and estimate the correspondences between 2D coronary artery points obtained from X-ray images and 3D points on the bilinear model of the left ventricle, we adopted an EM-like method, which combines EM with a deterministic annealing scheme [157] (Section 5.2.2).

5.2.1 Construction of a Bilinear Ventricle Model

A spatiotemporal model of the coronary arterial tree could be employed to regularise the ill-posed reconstruction problem. However, building a spatiotemporal model for the coronary arteries is not straightforward due to topological variations of the structure of interest. To address this problem, our method assumes that the coronary arteries lie on the surface of ventricular epicardium and move together with it. Therefore, a spatiotemporal model of the coronary arteries can be implicitly represented by a spatiotemporal model of the ventricular epicardium and arterial locations on this ventricular model. Fortunately, the construction of a spatiotemporal model of the heart has been exhaustively studied in the literature [33, 176–178].

A bilinear statistical model [179] is a natural candidate to model observations, which possess variations due to two independent factors. Inter-patient shape variability and beating motion of the heart can be considered as two independent factors that generate the spatiotemporal structure of the ventricular epicardium. In our work, a bilinear model is used as the spatiotemporal model of the ventricle. In fact, it was shown in [178] that a bilinear model can provide a compact way to model the shape of the human heart by separating inter-subject from temporal variations (Fig. 5.1).

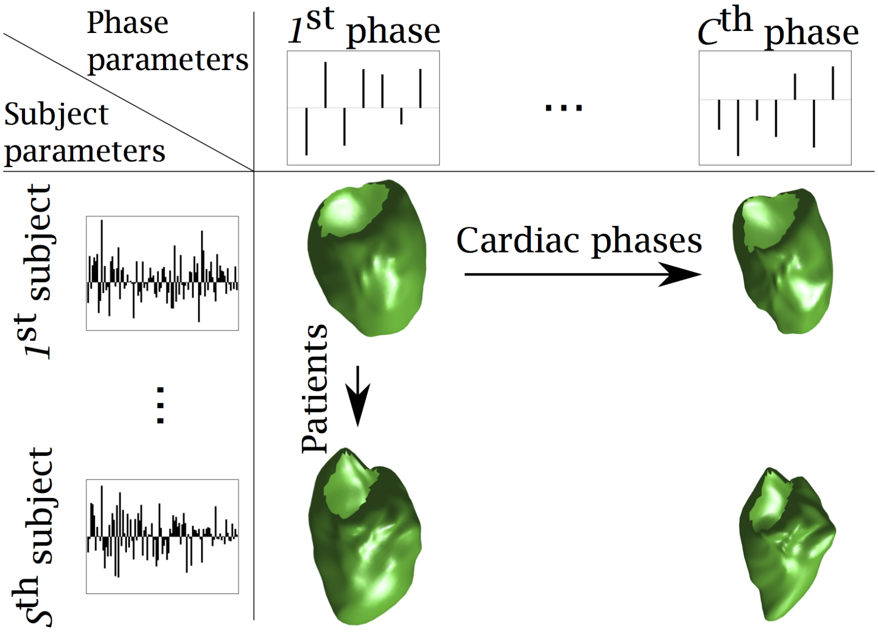

Figure 5.1: Bilinear model is a statistical model with two sets of parameters to define two variations of the data. In our case, the variations are defined as subject and cardiac phase variations, and controlled by subject ($\boldsymbol{a}^s$) and phase ($\boldsymbol{b}^c$) parameters.

A bilinear model is a two-factor model whose outputs are linear in either factor when the other is kept constant [179]. Suppose an output of a bilinear model, $\boldsymbol{y}^{sc}$, is a K dimensional vector. Each element of $\boldsymbol{y}^{sc}$ is written as:

$$y_k^{sc} = \sum_i^I \sum_j^J w_{ijk} a_i^s b_j^c = \boldsymbol{a}^{sT} \boldsymbol{W}_k \boldsymbol{b}^c, \tag{5.1}$$

where $\boldsymbol{a}^s$, $\boldsymbol{b}^c$ denote bilinear model parameters of s^{th} subject ($s \in 1 \cdots S$) and c^{th} phase ($c \in 1 \cdots C$), which are I and J dimensional vectors, respectively. $\boldsymbol{W}_k$ is an $I \times J$ matrix determining the interaction of two factors. $\boldsymbol{W}_k$, for $k = 1 \ldots K$, forms 3-dimensional matrix $\boldsymbol{W}$, which defines a mapping from the subject and phase spaces into observation space. In the training phase, the interaction between subject and phase factors are learned by fitting a bilinear model to training observations. During testing, the same model is adapted to an observation by keeping the common ingredient between the training and test cases. In our case, the interaction matrix, $\boldsymbol{W}$, is learned from a training set of ventricular epicardium shapes and bilinear model parameters for subject, $\widehat{\boldsymbol{a}}$ and for cardiac phases $\widehat{\boldsymbol{B}} = [\widehat{\boldsymbol{b}}^1 \cdots \widehat{\boldsymbol{b}}^C]$ are sought.

Let $\boldsymbol{Y}$ denote the observation matrix consisted of deviations from the mean shape which is computed by taking average of the shapes for all styles and contents. Instead of writing $\boldsymbol{Y}$ as a three dimensional array, SC K-dimensional vectors are stacked into a single $(SK) \times C$ matrix in order to exploit standard matrix algorithms [179],

$$\boldsymbol{Y} = \begin{bmatrix} \boldsymbol{y}^{11} & \ldots & \boldsymbol{y}^{1C} \\ \vdots & \ddots & \\ \boldsymbol{y}^{S1} & & \boldsymbol{y}^{SC} \end{bmatrix}. \tag{5.2}$$

To utilize $\boldsymbol{Y}$ in fitting, we also need to define *vector transpose* operation [179]. We assume that any $AK \times B$ matrix $\boldsymbol{X}$ is constructed by stacking AB K-dimensional vectors. Vector transpose $\boldsymbol{X}^{VT}$ is defined to be $BK \times A$ matrix consisting of same K-dimensional vectors stacked B down and A across. Therefore, we can write $KC \times S$ matrix $\boldsymbol{Y}^{VT}$ as

$$\boldsymbol{Y}^{VT} = \begin{bmatrix} \boldsymbol{y}^{11} & \ldots & \boldsymbol{y}^{1S} \\ \vdots & \ddots & \\ \boldsymbol{y}^{C1} & & \boldsymbol{y}^{CS} \end{bmatrix}. \tag{5.3}$$

We can also define $IK \times J$ stacked weight matrix $\boldsymbol{W}$ which consists of the IJ K-dimensional basis functions $\boldsymbol{w}_{ij}$ as

$$\boldsymbol{W} = \begin{bmatrix} \boldsymbol{w}_{11} & \ldots & \boldsymbol{w}_{1J} \\ \vdots & \ddots & \\ \boldsymbol{w}_{I1} & & \boldsymbol{w}_{IJ} \end{bmatrix}. \tag{5.4}$$

Finally, we could write our model in two different forms

$$\begin{aligned} \boldsymbol{Y} &= [\boldsymbol{W}^{VT}\boldsymbol{A}]^{VT}\boldsymbol{B}, \\ \boldsymbol{Y}^{VT} &= [\boldsymbol{W}\boldsymbol{B}]^{VT}\boldsymbol{A}, \end{aligned} \tag{5.5}$$

where $\boldsymbol{A}$ is a $I \times S$ matrix and $\boldsymbol{B}$ is a $J \times C$ consisting of stacked style and content parameters

$$\begin{aligned} \boldsymbol{A} &= [\boldsymbol{a}^1 \dots \boldsymbol{a}^S], \\ \boldsymbol{B} &= [\boldsymbol{b}^1 \dots \boldsymbol{b}^C]. \end{aligned} \tag{5.6}$$

In order to train bilinear model using observations, an iterative procedure is followed. For an initial estimate of $\boldsymbol{B}$ (must be an orthogonal matrix) and given observation matrix $\boldsymbol{Y}$, $[\boldsymbol{Y}\boldsymbol{B}^T]^{VT} = \boldsymbol{W}^{VT}\boldsymbol{A}$ (Eq. 5.5). We compute singular value decomposition (SVD) of $[\boldsymbol{Y}\boldsymbol{B}^T]^{VT} = \boldsymbol{U}\boldsymbol{D}\boldsymbol{V}^T$ and update our estimate of $\boldsymbol{A}$ to be the first I rows of $\boldsymbol{V}^T$. Given estimate of $\boldsymbol{A}$ which is orthogonal, $[\boldsymbol{Y}^{VT}\boldsymbol{A}^T]^{VT} = \boldsymbol{W}\boldsymbol{B}$. Similarly, by computing SVD of $[\boldsymbol{Y}^{VT}\boldsymbol{A}^T]^{VT}$, we can estimate our update of $\boldsymbol{B}$ to be the first J rows of $\boldsymbol{V}^T$. Convergence in this iterative procedure is guaranteed [179]. Upon convergence, we can compute $\boldsymbol{W} = [[\boldsymbol{Y}\boldsymbol{B}^T]^{VT}\boldsymbol{A}^T]^{VT}$ to obtain the basis vector. If observation data is evenly distributed across styles and content classes, the parameter values will minimize total squared error [179].

The bilinear model of the ventricle surface is capable of capturing inter-subject and temporal variations of its landmark points. However, it does not contain any information regarding the arterial locations. To obviate this shortcoming, the probability of corresponding to an arterial location, p_n, is defined for each landmark point.

Coronary arteries from an atlas of the human heart [180] are used to assign p_n for every landmark of the bilinear model. In [180], a mean volume is obtained via group-wise registration of training CT images. Coronary arteries, ventricles and other structures of the heart are segmented from the mean volume and represented as surface meshes to construct the atlas of the heart. Furthermore, the segmentations from the mean volume are propagated to each training shape by using the estimated inverse transformations to obtain surface representation with implicit correspondences. In our work, these surface meshes are employed as the training data for the bilinear model training. Therefore, an implicit correspondence between the atlas of the heart and the bilinear model landmarks is established. As a result, it is feasible to determine p_n values directly using the atlas of the heart.

In order to assign p_n values, points on the epicardial surface of the atlas that are closest to the centrelines of the coronary arteries are determined. Using these closest points, a signed distance function is computed on the atlas and p_n values are assigned as:

$$p_n = \frac{\exp^{-(d_n/\zeta)^2}}{\sum_{n=1}^{N} \exp^{-(d_n/\zeta)^2}}, \tag{5.7}$$

where d_n is the distance of nth landmark to the nearest point and ζ is a constant (Fig. 5.2). A large ζ value provides flexibility to compensate for the anatomical variability of coronary arterial trees.

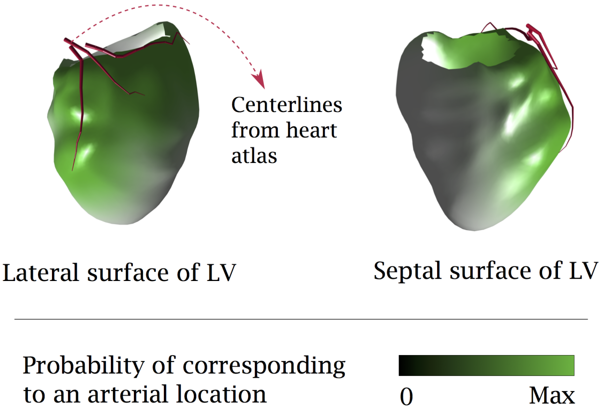

Figure 5.2: Probability of corresponding to an arterial location: A probability value is assigned to each landmark point of the bilinear model using the distance between the landmark point and the closest coronary artery point. The coronary artery points are obtained from the atlas of the heart [180]. This figure shows the probability values of every landmark point on surface of the bilinear model.

5.2.2 Reconstruction Energy Formulation and Minimisation

Our method assumes that we are given M 2D centreline points ($M \ll N$) tracked over sequence of F RA images. The 2D centreline points are considered to be the projections of the unknown 3D coronary centreline points that lie on the surface of the bilinear model of the ventricular epicardium. The corresponding ECG signal is used to assign each X-ray image to a cardiac phase in a canonical cycle. From the time-stamped point set we estimate i) the bilinear model parameters, $\widehat{\boldsymbol{a}}$ and $\widehat{\boldsymbol{B}}$, ii) the rotation matrix and the translation vector between the bilinear model and the X-ray coordinate systems, $\widehat{\boldsymbol{R}}$ and $\widehat{\boldsymbol{t}}$, and iii) the correspondences between the 2D points on the X-ray images and the 3D points on the bilinear model, denoted by a $M \times N$ correspondence matrix $\widehat{\boldsymbol{G}}$ (Fig. 5.3). The problem is formulated as a maximum a posteriori (MAP) estimation of these unknowns.

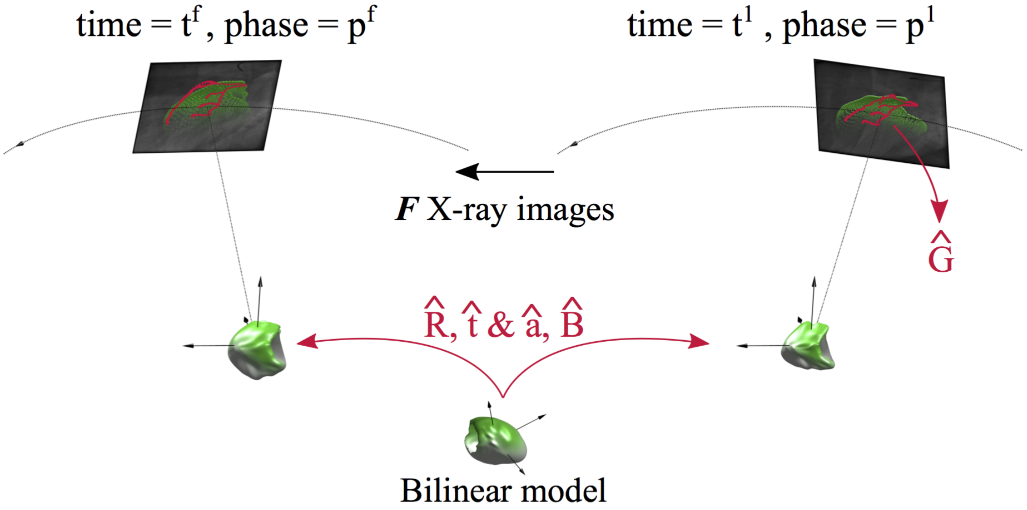

(a)

Figure 5.3: The overview of the method: From the time-stamped and tracked 2D centreline point set (red points on the X-ray images) we estimate i) the bilinear model parameters, $\widehat{\boldsymbol{a}}$ and $\widehat{\boldsymbol{B}}$, ii) the rotation matrix and the translation vector between the bilinear model and the X-ray coordinate systems, $\widehat{\boldsymbol{R}}$ and $\widehat{\boldsymbol{t}}$, and iii) the correspondences between the 2D points on the X-ray images and the 3D points on the bilinear model, $\widehat{\boldsymbol{G}}$. The MAP estimation of these parameters are formulated using 2D centreline point set and the forward-projection of bilinear model landmark points, which are shown by red and green points on the X-ray images, respectively.

5.2.2.1 Notation

Suppose $\mathbb{X} = \{\boldsymbol{\mathcal{X}}_m\}_{m=1}^{M}$ denote M centreline points over F frames, and $\boldsymbol{\mathcal{X}}_m = \{\boldsymbol{x}_m^f\}_{f=1}^{F}$ denote F 2D points for one particular corresponding location on the artery centreline over the sequence. In other words, $\boldsymbol{\mathcal{X}}_m$ is the 2D trajectory of mth centreline point. Similarly, $\widehat{\mathbb{X}} = \{\widehat{\boldsymbol{\mathcal{X}}}_n\}_{n=1}^{N}$ denote N landmark points over F frames describing the projection of 3D+t bilinear model, and $\widehat{\boldsymbol{\mathcal{X}}}_n = \{\widehat{\boldsymbol{x}}_n^f\}_{f=1}^{F}$

denote F 2D points for one particular landmark of the bilinear model over the sequence, projected onto the 2D views. Furthermore, $\widehat{\boldsymbol{\mathcal{Y}}}_n = \{\widehat{\boldsymbol{y}}_n^f\}_{f=1}^F$ denote F 3D points for one particular landmark of the bilinear model over the sequence.

The description of the X-ray acquisition geometry employed in this work are detailed in Chapter 3. Following the description, the projection operation is written as:

$$\begin{bmatrix} \widehat{\boldsymbol{x}}_n^f \\ 1 \end{bmatrix} \simeq \begin{bmatrix} \widehat{\boldsymbol{y}}_n^f \\ 1 \end{bmatrix} = \boldsymbol{Q}^f \begin{bmatrix} \widehat{\boldsymbol{R}}[\overline{\boldsymbol{W}}^{VT}\widehat{\boldsymbol{a}}]^{VT}\widehat{\boldsymbol{b}} + \widehat{\boldsymbol{t}} \\ 1 \end{bmatrix}, \tag{5.8}$$

where $\overline{\boldsymbol{W}}$ is a $3I \times J$ matrix made of the rows of $\boldsymbol{W}$, which corresponds to one of the landmark point.

5.2.2.2 Temporal Alignment

In Eq. (5.8), $\widehat{\boldsymbol{b}}$ is the column of $\widehat{\boldsymbol{B}}$ corresponding to the phase of fth X-ray image. Due to heart rate differences, there might be a temporal misalignment between the cardiac phases of the bilinear model and the cardiac phases assigned to X-ray images in the RA sequence. To overcome this problem, a piecewise linear function is proposed. This function maps the systolic and diastolic cardiac phases assigned to X-ray images to the corresponding cardiac phases of the bilinear model using two linear functions (Fig. 5.4). This temporal alignment function is represented by a single parameter (end-systolic phase for the patient) since the end-systolic phase for the bilinear model is known. This single parameter is not estimated, but manually obtained by the help of the cardiac phases assigned using ECG and visual inspection of the coronary angiography images.

Another issue may arise since the bilinear model is defined at discrete time points. Mapped cardiac phases assigned to X-ray images may not coincide with the discrete cardiac phases of the bilinear model training set. In such cases, $\widehat{\boldsymbol{y}}_n^f$ is interpolated from the cardiac phase parameter vectors of two neighbouring discrete time points.

5.2.2.3 MAP Formulation

The reconstruction problem is formulated as a 2D+t/3D+t registration between the given 2D points tracked over the sequence and the projections of the bilinear model points. Assuming that the projections of the points in the bilinear model of

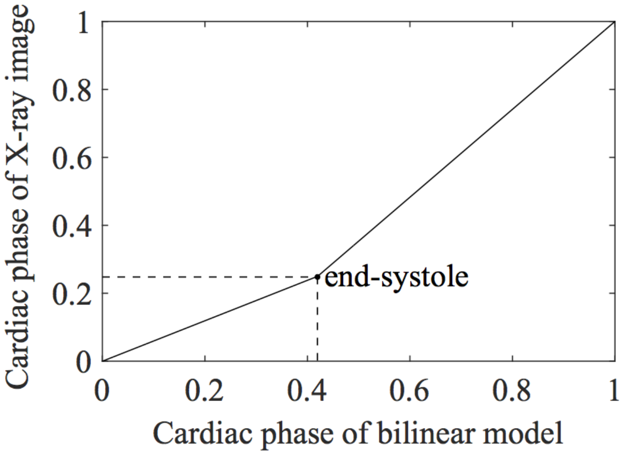

Figure 5.4: Temporal alignment between the cardiac phases of the patient and of the bilinear model is done with a piecewise linear function.

the ventricle specify Gaussian cluster centres, the distribution of ventricle points could be represented by a Gaussian mixture model (GMM). This GMM can be fitted to the given 2D points to find the reconstruction. Specifically, we find $\widehat{\boldsymbol{a}}$, $\widehat{\boldsymbol{B}}$, $\widehat{\boldsymbol{R}}$, $\widehat{\boldsymbol{t}}$ and $\boldsymbol{G}$ by minimising a log-posterior energy function. The minus log-posterior energy can be written as weighted sum of a distance and a regularisation term [157]:

$$E = E_{data} + E_{reg}, \tag{5.9}$$

where

$$E_{data} = -\log p(\mathbb{X}|\widehat{\boldsymbol{a}}, \widehat{\boldsymbol{B}}, \widehat{\boldsymbol{R}}, \widehat{\boldsymbol{t}}), \tag{5.10}$$

and

$$E_{reg} = -\log p(\widehat{\boldsymbol{a}}) - \log p(\widehat{\boldsymbol{B}}). \tag{5.11}$$

The final form of E_{data} is reduced to a weighted sum of squared distances between 2D observations and 2D projections of the bilinear model landmark estimates:

$$E_{data} = \sum_{f}^{F} \sum_{n}^{N} \sum_{m}^{M} \widehat{G}_{mn} \|\boldsymbol{x}_m^f - \widehat{\boldsymbol{x}}_n^f\|^2, \tag{5.12}$$

where $\widehat{G}_{mn}$ is the entry at mth row and nth column of $\widehat{\boldsymbol{G}}$ matrix, and denote the posterior probability. It is written as:

$$\widehat{G}_{mn} = \frac{p_n \exp\left(-\frac{\sum_{f=1}^{F} \|\boldsymbol{x}_{\boldsymbol{m}}^{\boldsymbol{f}} - \widehat{\boldsymbol{x}}_{\boldsymbol{n}}^{\boldsymbol{f}}\|^2}{2\tau F}\right)}{c + \sum_{n=1}^{N} p_n \exp\left(-\frac{\sum_{1}^{F} \|\boldsymbol{x}_{\boldsymbol{m}}^{\boldsymbol{f}} - \widehat{\boldsymbol{x}}_{\boldsymbol{n}}^{\boldsymbol{f}}\|^2}{2\tau F}\right)}, \tag{5.13}$$

where $c = ((w)/(1-w))(\sqrt{2\pi\tau}/M)$ is a constant term.

The regularisation term is defined as the negative log-likelihood of the prior distribution of bilinear model parameters. To this end, the bilinear model parameters, which are learned for the training ventricular surfaces are used to perform kernel density estimations of the components of the parameter vector $\widehat{\boldsymbol{a}}$ and matrix $\widehat{\boldsymbol{B}}$. During the training of the bilinear model, S I-dimensional subject parameter vector, $\boldsymbol{a}^s$ and C J-dimensional phase parameter vector, $\boldsymbol{b}^c$, are learned as by-product. Assuming that the scalar components of $\widehat{\boldsymbol{a}}$ and matrix $\widehat{\boldsymbol{B}}$ are independent, the prior probabilities can be written using the kernel density estimations:

$$p(\widehat{\boldsymbol{a}}) = \prod_{i=1}^{I} \frac{1}{hS} \sum_{s=1}^{S} \Phi\left(\frac{\widehat{a}_i - a_i^s}{h}\right) \tag{5.14}$$

$$p(\widehat{\boldsymbol{B}}) = \prod_{j=1}^{J} \prod_{c=1}^{C} \frac{1}{hC} \sum_{\bar{c}=1}^{C} \Phi\left(\frac{\widehat{B}_{jc} - b_j^{\bar{c}}}{h}\right) \tag{5.15}$$

where Φ denotes a Gaussian kernel and h is the bandwidth of the kernel which is estimated using Silverman's rule of thumb [181]. Since our method optimises for subject and phase parameters separately, the regularisation term is written as:

$$E_{reg} = \begin{cases} -\sum_{i=1}^{I} \log\left(\frac{1}{hS} \sum_{s=1}^{S} \Phi\left(\frac{\widehat{a}_i - a_i^s}{h}\right)\right), & \text{if minimising for } \widehat{\boldsymbol{a}}, \widehat{\boldsymbol{R}}, \widehat{\boldsymbol{t}}, \\ -\sum_{j=1}^{J} \sum_{c=1}^{C} \log\left(\frac{1}{hC} \sum_{\bar{c}=1}^{C} \Phi\left(\frac{\widehat{B}_{jc} - b_j^{\bar{c}}}{h}\right)\right), & \text{if minimising for } \widehat{\boldsymbol{B}}. \end{cases} \tag{5.16}$$

5.2.2.4 Optimisation

A simplified EM-like method [157] is adopted to find the bilinear model parameters, transformation and correspondences by an alternating scheme. There are three main differences to the standard EM method.

As the first difference, some parameters are assumed to be deterministic during iterations. The mixture weights and the covariances of the Gaussian components are estimated in a standard EM formulation. This provides additional flexibility for the model, and can lead to overfitting. To avoid overfitting, the simplified EM-like method combines the EM algorithm with a deterministic annealing scheme. Specifically, instead of estimating the covariances of the Gaussian components, an annealing parameter, τ, is used to decrease the isotropic variance of the Gaussian clusters in every iteration. In addition, the mixture weights are fixed in our method and obtained as described in Section 5.2.1.

Another difference is that the annealing parameter also acts on the regularisation energy term to control the level of the regularisation. The intuition is to keep the regularisation high to avoid local minima when the estimation is far away from the optimum and gradually relax as the estimation comes closer to the global minimum. In addition to that, a second weighting is necessary for the regularisation energy to balance the influence of it. Thus, the energy to be minimised can be rewritten as:

$$E = E_{data} + \tau \lambda_r E_{reg} \tag{5.17}$$

where λ_r determines the weighting between two energy terms and τ is the annealing parameter.

The third difference is the outlier removal step as in [182]. The projected bilinear model points and the corresponding Gaussian clusters are discarded if the sum of the posterior probabilities for all the M observed points are smaller than a threshold, β. In other words, the Gaussian cluster is not considered if there is no corresponding 2D point. This step effectively reduces number of Gaussian clusters during parameter estimation. This outlier removal step is important since $M \ll N$.

The algorithm can be simply described as follows: In the E step, we update the entries of the correspondence matrix $\widehat{\boldsymbol{G}}$. In the M step, the total energy in Eq. (5.17) is minimised to estimate the parameters. The overall algorithm is presented in Algorithm 1.

Algorithm 1

3D+t Coronary artery centreline reconstruction algorithm

```
Input:
  $\mathbb{X} = \{\boldsymbol{\mathcal{X}}_m\}_{m=1}^{M}$: 2D points tracked over X-ray sequence
  $\{\boldsymbol{Q}^f\}_{f=1}^{F}$: Projection matrices
  $\boldsymbol{R_{ini}}$, $\boldsymbol{t_{ini}}$: Initial transformation
  $\boldsymbol{a_{ini}}, \boldsymbol{B_{ini}}$: Initial parameters for the bilinear ventricle model
  $\tau_{ini}$, $\tau_{up}$ and $\tau_{fin}$: Annealing parameters
  $\lambda_r$, $\beta$ and $\zeta$: Other parameters
Output:
  $\widehat{\boldsymbol{a}}, \widehat{\boldsymbol{B}}$: Estimates for bilinear model parameters
  $\widehat{\boldsymbol{R}}, \widehat{\boldsymbol{t}}$: Global transformation
  $\widehat{\boldsymbol{G}}$: Correspondence matrix

$\widehat{\boldsymbol{R}} \leftarrow \boldsymbol{R_{ini}}$, $\widehat{\boldsymbol{t}} \leftarrow \boldsymbol{t_{ini}}$, $\widehat{\boldsymbol{a}} \leftarrow \boldsymbol{a_{ini}}$, $\widehat{\boldsymbol{B}} \leftarrow \boldsymbol{B_{ini}}$ and $\tau \leftarrow \tau_{ini}$
repeat
    Compute $\widehat{\boldsymbol{G}}$ (Eq. (5.13))
    if $\sum_{m=1}^{M} \widehat{G}_{mn} < \beta$ then
        Discard $\widehat{\boldsymbol{x}}_n^f$, and its Gaussian cluster
    end if
    Update $\widehat{\boldsymbol{R}}$, $\widehat{\boldsymbol{t}}$, and $\widehat{\boldsymbol{a}}$ by minimising $E_{tot}$ (Eq. (5.17))
    Update $\widehat{\boldsymbol{B}}$ by minimising $E_{tot}$ (Eq.( 5.17))
    $\tau \leftarrow \tau_{up} \times \tau$
until $\tau < \tau_{fin}$
```

5.3 Experiments

Training surface meshes describing the left ventricular epicardium ($N = 2044$) are obtained using an atlas based segmentation algorithm [180] from 134 retrospectively ECG-gated multi-slice CT images. The proximal parts of the left coronary artery tree are also extracted from the cardiac atlas utilised for segmentation (Fig. 5.2). The surface meshes are temporally aligned as in [178] to compensate for heart rate differences between patients. Procrustes alignment [183] is performed to align training surfaces spatially. During Procrustes alignment, we opted for rigid transformations without scaling and incorporated the scaling effects into our statistical model.

In order to quantitatively evaluate our algorithm, we generated synthetic rotational angiography data using the single left coronary artery geometry of the 4D XCAT phantom [147]. The cardiac cycle was set to be 1000ms, with no respiratory motion present. X-ray imaging parameters, including projection matrices, number of images (117) and frame rate (30 fps) were derived from a clinical dataset. Since we have the 3D+t ground truth information for the centrelines, we created a total of 208 corresponding coronary artery points (one centre point for each longitudinal knot of non-uniform rational B-spline surface [147]) and projected these to generate the 2D observation points in 117 projection images.

We used the phantom data to evaluate the algorithm's robustness to missing data and noise. In the first experiment (`Experiment 1`), we randomly removed 0% to 50% of 2D observation points which describe the projected 2D trajectory of each tracked coronary artery point along the sequence of projection images. In the second experiment (`Experiment 2`), we removed the 2D observation points according to a sampling scheme that mimics the sparsity associated to missing detail in the detection of centreline points in the 2D views. To this end, we selected a set of points, $\mathcal{P}_1$, which consisted of a starting point, bifurcations and end points. Similarly, we defined $\mathcal{P}_2$ as the set of points, which are the midpoints of the segments described by the points in the set $\mathcal{P}_1$ and defined $\mathcal{P}_3$ as the set of points, which are the midpoints of the segments described by the points in the set $\mathcal{P}_1$ and $\mathcal{P}_2$. We applied our reconstruction algorithm given the points in the sets $\mathcal{P}_1$ (9.13% of all points), $\mathcal{P}_1 \cup \mathcal{P}_1$ (16.35% of all points) and $\mathcal{P}_1 \cup \mathcal{P}_2 \cup \mathcal{P}_3$ (28.37% of all points). We also evaluated the performance under uncertain measurements by adding zero mean Gaussian noise (σ 0.25 to 1.25 mm) to the 2D points (`Experiment 3`). In all of the experiments, the reconstruction errors were measured as the root-mean-square errors in 3D between the reconstructed points and the true 3D positions.

The parameters of the algorithm are set empirically. The annealing parameters, τ_{ini}, τ_{fin} and τ_{up} were set to 500, 3 and 0.95, respectively [157]. The threshold for rejecting projected bilinear point, β, was set to 0.05 and the weighting, λ, of the regularisation term was set to 2.5×10^5. Finally, the weight, w, was set to 1.0×10^{-8} since we assume that there are no outliers in 2D observations.

5.4 Results and Discussion

The results show that the 3D+t reconstruction performance of our algorithm stays stable even under 1.25 mm 2D observation noise, which is approximately 6-7 times of the pixel resolution of the rotational angiography (Fig. 5.5b).

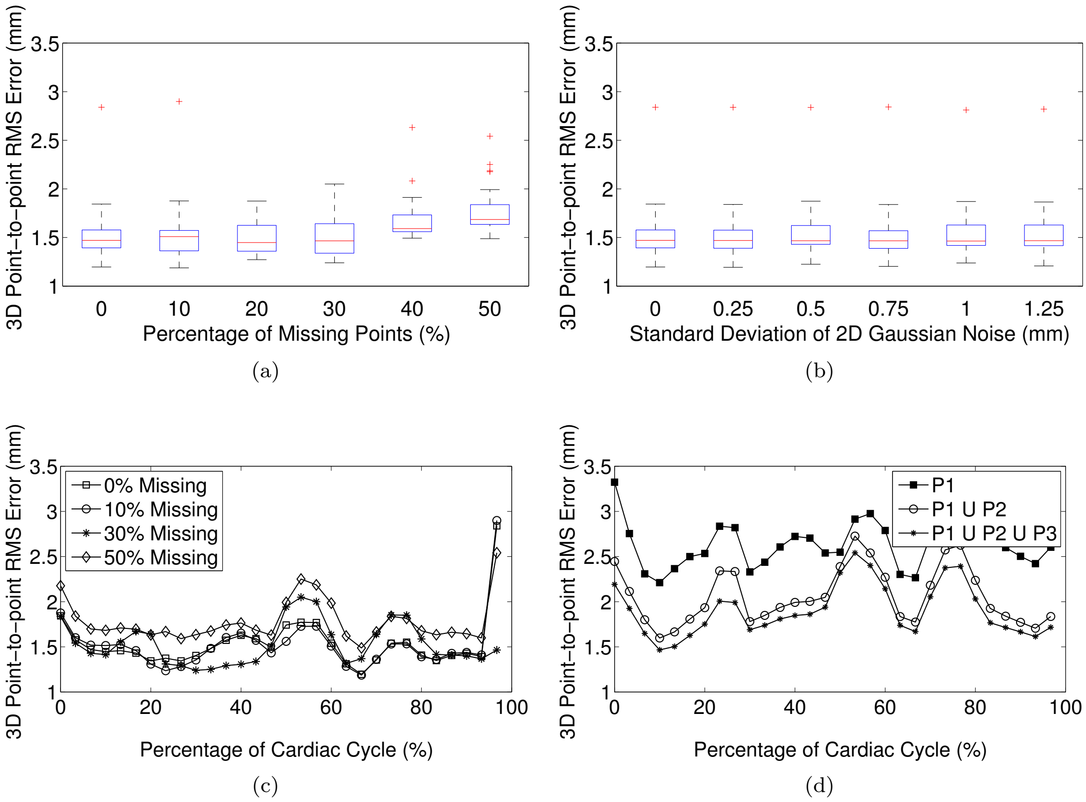

(a) (b)

(c) (d)

Figure 5.5: Quantitative 3D+t reconstruction results on phantom data: (a) Results of the `Experiment 1`, (b) results of the `Experiment 3`, (c) results of the `Experiment 1` for all cardiac phases, (d) results of the `Experiment 2` for all cardiac phases. See text for the details of the experiments.

Although there are some outliers, the results indicate that the proposed method is able to handle missing data (Fig. 5.5a). In particular, the qualitative results shows that the 3D reconstruction of missing data points are recovered satisfactorily. The method is not able to accurately reconstruct the points near the LAD-LCX branching. It is possible that this region could not be modelled solely by the left ventricular epicardium.

The accuracy of the algorithm quickly increases with addition of a small number of points to the base set, $\mathcal{P}_1$ and continue to increase as more 2D observations points are added (Fig. 5.5d).

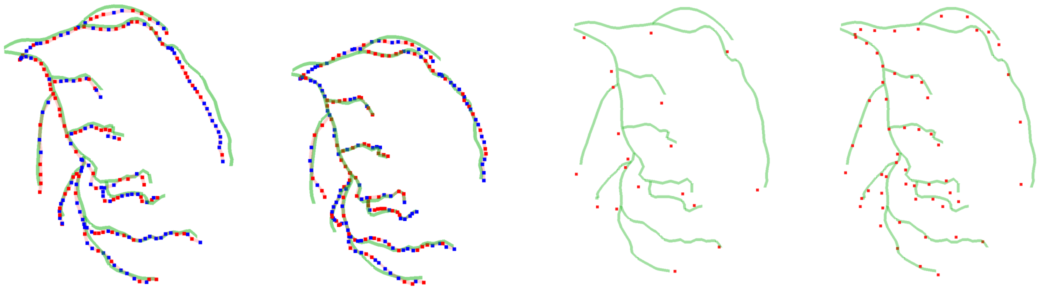
(a) (b)

Figure 5.6: Qualitative 3D+t reconstruction results on phantom data: (a) Results of the `Experiment 1` for end-diastolic and end-systolic phases, (b) results of the `Experiment 2` for $\mathcal{P}_1$ and $\mathcal{P}_1 \cup \mathcal{P}_2 \cup \mathcal{P}_3$. The ground truth centreline of the coronary artery tree is shown in green. Reconstructed points are given in red if 2D observation is available in the corresponding image and in blue if the 2D observation is removed.

From one point of view, our method resembles non-rigid structure from motion methods (NRSFM) in the computer vision literature. The fundamental difference of our method is that we do not directly impose a constraint on the non-rigid structure as it is done in NRSFM methods. In other words, although our attention is on the non-rigid structure of the arteries, we impose a constraint on the surface that the non-rigid structure is attached to. This difference comes with the price of having to estimate the correspondence between the 2D observations and landmarks of the bilinear model. In addition to that, some recent work discussed the bilinear structure of NRSFM [184] but does not fully describe how to reconstruct 3D structure out of 2D observations. In this work, we proposed a 2D+t/3D+t registration strategy to bridge this gap.

On the other hand, our method is similar to 2D+t/3D registration methods [33, 182] in the literature. However, these methods require an ECG gated CT image. Specifically, 3D coronary arterial trees extracted from the CT image is registered onto the X-ray angiography images. In our work, estimation of 3D+t structure of the coronary arteries is embedded into the registration framework.

The overall model (bilinear model, transformation and correspondences) presented in this chapter is a highly flexible model, thus prone to overfitting. In our initial experiments, we only utilised the deterministic annealing based EM method to fix some of the model parameters to circumvent the problem of overfitting. However, we observed that the model was still too flexible, and the resulting ventricular surfaces may show unrealistic deformations. To address this issue, two important measures were taken. First, the probabilities of corresponding an arterial location for each landmark point are defined and incorporated into the formulation to reduce the space of feasible correspondences. Second, we introduced a regularization term for bilinear model, which penalises the unrealistic deformations of the ventricular shape. In our experience, both of these regularisation efforts are equally important to prevent overfitting.

The 3D reconstruction errors shown in Fig. 5.5 are higher than the errors we obtain with the methods presented in Chapters 4 and 6. The reason for this difference can be explained by the representation accuracy of the motion model. In particular, we are making the assumption that it is possible to model myocardial/coronary motion with the apparent cardiac motion. A similar approach was taken in [33], where the coronary motion was modelled as a regression problem given the surface model of the heart. In that paper, the authors fit their motion model, and compared with the real motion of coronary arteries. The average error was approximately 1 mm, which is close to the error we achieved in our experiments. Therefore, one can argue that a more appropriate spatiotemporal model with a more realistic motion model is necessary to further reduce the error.

5.5 Conclusion

In this chapter, we present a method to reconstruct the 3D+t points of the coronary tree from rotational angiography images. The regularisation is achieved by constraining the motion and the shape of the coronary arteries by a spatiotemporal model of the epicardial surface of the ventricle. Although it is not discussed in this chapter, the reconstructed 3D+t points could be converted to 3D+t centrelines by a linking procedure [96] or 3D+t vascular surface [92] by incorporating the radius information.

Our method assumes that the angiography images are collected during a breath hold. To overcome this drawback, a respiratory motion model [171] could be incorporated into the energy minimisation formulation at the expense of estimating more parameters.

Currently, we assume that the 2D points tracked over the sequence of X-ray images are provided. However, automatic methods to determine the point correspondences must be explored.

Chapter 6

Bayesian Reconstruction of Coronary Artery Centrelines from X-ray Rotational Angiography Using a Mixture of Student's t-distributions

6.1 Introduction

Coronary artery disease (CAD) is a serious illness, which is the cause of 20% and 25.3% of all deaths in Europe and the US, respectively [185, 186]. Current clinical assessment of CAD is carried out using various diagnostic (CCTA, MRA) and interventional (X-ray angiography, IVUS, OCT) medical imaging techniques. Among those, invasive X-ray coronary angiography is still one of the most commonly available diagnostic imaging technique.

Despite continuous development of the X-ray angiography systems, X-ray coronary angiography is still inherently limited, since it can only provide 2D X-ray images of the moving coronary arteries. As a consequence, assessment of CAD still relies on direct analysis of 2D X-ray coronary angiography images. To overcome this shortcoming, 3D representations of coronary arteries can be reconstructed from X-ray angiography images. These 3D representations can be exploited to aid clinical decision making [26, 27], to guide subsequent interventions [21, 22], and to obtain estimation of clinically relevant physiological indices [44, 46]. However, because of several factors such as intensity inhomogeneity due to contrast material distribution, artery overlap/foreshortening, and cardiac/respiratory motion [11], the ill-posed problem of 3D reconstruction remains a challenging task.

Numerous methods for reconstruction of coronary arteries from X-ray angiography have been developed in the last decade [187]. Among those, model-based reconstruction (modelling) methods seek to generate a 3D representation of coronary arteries, which consists of a centreline, and, occasionally, artery surfaces. These methods typically select a subset of the acquired X-ray images via retrospective gating strategies, and use available 2D information in the selected images to compute 3D reconstructions. Depending on the the way the 2D information is used, modelling methods can be classified into two groups, namely back-projection and forward-projection based methods.

Back-projection based modelling methods extract 2D information from two or more X-ray angiography images, and collect them back in the 3D space to build the coronary artery tree. One way to achieve this is to take advantage of stereo or multi-view stereo approaches from computer vision literature [87–92, 96]. To this end, the centrelines of the arteries are segmented from 2D views, and correspondences between 2D centreline points from different views are established. Finally, 3D centreline points are reconstructed using triangulation [52], or more dedicated energy optimisation methods [187]. Correspondences are established on the space of candidate tuples of 2D centreline points, segmented from 2D X-ray images. As a consequence, these methods typically opt for computing the reconstruction from stereo views in order to keep the number of candidate tuples low. In addition to this drawback, they require accurate 2D artery centreline segmentations, which is typically obtained using manual or semi-automatic segmentation methods.

Another approach is to compute 2D vesselness responses [188, 189] to highlight coronary artery structures in different views, and back-project those responses into 3D space for further processing [99–101]. This process generates a 3D vesselness response, which can be segmented to find coronary artery reconstructions. Intuitively, these methods utilise 2D vesselness responses to eliminate the necessity of accurate artery segmentations from 2D X-ray images. These methods may require a large number of projection images at the same cardiac phase, especially in the presence of residual motion due to breathing or finite retrospective gating accuracy [100].

On the other hand, forward-projection based modelling methods use a 3D model of coronary arteries that adapts itself to the 2D information extracted from X-ray images. One popular 3D model is based on the active contours [74]. Each coronary branch is represented by an active contour, which evolves using a combination of external forces computed from 2D X-ray images [78, 80, 81, 83, 92, 190]. These methods are formulated to take advantage of the information from multiple X-ray images. This aspect is especially important for reconstruction, since it has been shown that the accuracy of the reconstruction depends on the angular separation of the selected X-ray images for reconstruction from two views [80, 93]. However, it is not always possible to select two views with adequate angular separation and minimal overlap/foreshortening. In addition, some of these methods require good initialisation of the active contours, which necessitates manual identification of some corresponding points from the X-ray images.

Most of the aforementioned modelling methods require clean and accurate 2D artery segmentations from X-ray images. However, segmentation of coronary arteries from X-ray images remains a challenging task due to inhomogeneous intensity, and artery overlap/foreshortening [155], and is thus prone to errors. In particular, the 2D segmentations from some of the X-ray views may include extra coronary artery branches, which are not visible in the rest of the X-ray images due to wash-in and wash-out of the contrast material. Moreover, 2D segmentations can be noisy or include erroneously segmented parts, which can go unnoticed during manual corrections. Therefore, reconstruction methods should be devised to be robust to these imperfections.

This chapter investigates extensions to the probabilistic mixture model based framework introduced in Chapter 4 in order to improve the robustness against imperfect segmentations, residual motion and overfitting. Particularly, the extra mixture model component accommodating the outliers is removed, and the mixture model components are replaced by Student's t-distributions which are inherently robust to the outlier points. Moreover, prior information regarding the structure of the coronary arteries is introduced in the formulation in terms of prior distributions to prevent overfitting of the mixture model and to increase the robustness in the presence of residual motion, which is explained in Section 4.4.

Similar to Chapter 4, we propose a novel forward-projection based method to reconstruct coronary artery centrelines from X-ray rotational angiography images. We employ a probabilistic mixture of Student's t-distributions to model the centrelines of the coronary arteries. Specifically, we describe these centrelines by a 3D point set, where the spatial locations of the points correspond to the means of the Student's t-distribution components. Taking advantage of this representation, we formulate the reconstruction problem as the problem of estimating the mixture model parameters, given the 2D delineations of coronary artery centrelines from retrospectively gated X-ray images. As a key aspect, the heavy tails of t-distributions makes the proposed algorithm more robust towards inaccuracies in the extracted 2D centrelines as well as gating intervals. Moreover, the probabilistic clustering allows establishing indirect correspondences between the projections, eliminating the need for exact point bindings.

In most modelling methods in the literature, a subset of images of the same cardiac phase are selected using ECG gating. However, the selected images are not exactly at the same cardiac motion state due to finite gating accuracy. Our probabilistic formulation handles residual motion, and generates an average model of the 3D coronary artery centrelines that achieves the minimum reconstruction error at the desired cardiac phase.

The ability to incorporate prior information is a desirable feature for model-based coronary artery reconstruction algorithms to improve results and reduce the number of the required cardiac cycles [100]. However, this aspect is not thoroughly investigated in the relevant literature. The method proposed in this chapter provides a convenient framework for the inclusion of prior information. In particular, we extend our preliminary work in Chapter 4 [191, 192], by introducing Bayesian priors on the means of the mixture components that describe the reconstruction, and mixture weights. The former penalises deviation from a linear spatial alignment of components in a local neighbourhood, whereas the latter effectively removes the redundant mixture components. Consequently, these priors regularise the reconstruction, and prevent overfitting of the parameters owing to the outliers, overall increasing the robustness of the method.

This chapter is structured as follows. In Section 6.2, we first explain X-ray image selection via retrospective ECG gating, and subsequent delineation of coronary centrelines from selected images. We then provide detailed formulation of our probabilistic reconstruction method, and an algorithmic summary of it. We describe experimental setup on both synthetic and real X-ray rotational angiography data in Section 6.3, and present results in Section 6.4. We discuss our results in Section 6.5, and compare our results with the recent literature. Finally, we conclude in Section 6.6.

6.2 Methods

Following the acquisition of X-ray coronary angiography images from different views, retrospective ECG gating is performed to select images that correspond to the same cardiac motion state of the coronary arteries (Chapter 3). Points describing the locations of coronary arteries in 2D X-ray images are extracted using a coronary artery segmentation algorithm (Section 6.2.1). The main idea of our method is to model coronary artery centrelines in 3D using a probabilistic mixture model with priors on some of the parameters. Segmented 2D centreline points from different X-ray views are considered to be projections of 3D coronary artery centreline points drawn from the mixture model. Thus, reconstruction is formulated as estimation of mixture model parameters (Section 6.2.2). Reconstructed 3D coronary centreline points are connected by computing a minimum spanning arborescence, and pruned if necessary (Section 6.2.3).

6.2.1 Segmentation of Coronary Artery Centrelines from X-ray Images

Initially, the coronary artery centrelines need to be segmented from the selected 2D X-ray images by a convenient segmentation algorithm such as those described in [96, 193]. The resulting segmentation may include some erroneous parts due to noise or other background structures such as catheter, spine and diaphragm. Similarly, it may also include some coronary artery branches that are not visible in other X-ray images due to the distribution of intra-arterial contrast medium over time. We refer to these noisy and inconsistent structures as outliers. The segmented centrelines are then converted to point sets for further processing by placing a point at the location of each pixel in the segmentation.

6.2.2 Probabilistic Mixture Model-based Reconstruction Method

Our main idea is to represent the 3D coronary artery centrelines probabilistically using a mixture of Student's t-distributions, thus formulating the reconstruction, as the problem of estimation of mixture model parameters, given segmented 2D centrelines from the X-ray images. Additionally, Bayesian priors are introduced on: i) the means of the t-distribution components to spatially regularise the resulting reconstruction, and ii) the mixture weights to avoid overfitting.

6.2.2.1 Probabilistic Modelling of the Data

Suppose there are F retrospectively gated X-ray images. Let $\boldsymbol{\mathcal{X}}^f = \{\boldsymbol{x}_n^f \in \mathbb{R}^2\}_{n=1}^{Nf}$ be the set of 2D centreline points extracted from the f^{th} X-ray image. Similarly, let $\boldsymbol{\mathcal{Y}} = \{\boldsymbol{y}_m \in \mathbb{R}^3\}_{m=1}^{M}$ be the set of 3D points describing the coronary artery centrelines to be reconstructed.

Our objective is to model 3D coronary centrelines using a mixture of Student's t-distributions. To this end, 3D points describing the centrelines are assumed to specify the means of the t-distributions. Moreover, the segmented 2D centreline points are considered to be generated by sampling from the mixture and then projecting onto the 2D X-ray images. Given these assumptions, a mixture model representation of t-distributions can be written as

$$P(\boldsymbol{x}_n^f|\boldsymbol{\mathcal{Y}}, \boldsymbol{\mathcal{Q}}) = \sum_{m=1}^{M} \pi_m \mathcal{S}(\boldsymbol{x}_n^f|\Theta^f(\boldsymbol{y}_m), \sigma^2, \nu_m), \tag{6.1}$$

where $\mathcal{Q} = \{\boldsymbol{\pi}, \sigma^2, \boldsymbol{\nu}\}$ denotes the parameters of the mixture model: $\boldsymbol{\pi}$ is the vector of mixture weights satisfying $\sum_m^M \pi_m = 1$, σ^2 is the isotropic variance, and $\boldsymbol{\nu}$ is the degrees of freedoms of the Student's t-distributions. Moreover, $\Theta^f : \mathbb{R}^3 \to \mathbb{R}^2$ is the projection function for the f^{th} X-ray image.

A multivariate t-distribution with mean $\boldsymbol{\mu}$, covariance $\boldsymbol{\Sigma}$, and degree of freedom ν has the following probability density function:

$$\mathcal{S}(\boldsymbol{x}|\boldsymbol{\mu}, \boldsymbol{\Sigma}, \nu) = \frac{\Gamma(\frac{\nu+d}{2})|\boldsymbol{\Sigma}|^{-\frac{1}{2}}}{(\pi\nu)^{\frac{d}{2}}\Gamma(\frac{\nu}{2})}\Big[1 + \frac{(\boldsymbol{x}-\boldsymbol{\mu})^T\boldsymbol{\Sigma}^{-\frac{1}{2}}(\boldsymbol{x}-\boldsymbol{\mu})}{\nu}\Big]^{-(\frac{\nu+d}{2})}, \tag{6.2}$$

where d is the dimension of the data, and Γ denotes the Gamma function. For the case $\nu = 1$, t-distribution reduces to Cauchy distribution, whereas in the limit $\nu \to \infty$, t-distribution becomes a Gaussian distribution with mean $\boldsymbol{\mu}$ and covariance $\boldsymbol{\Sigma}$ [165]. The density function in Eq. (6.2) can also be written as an infinite mixture of scaled Gaussians

$$\mathcal{S}(\boldsymbol{x}|\boldsymbol{\mu}, \boldsymbol{\Sigma}, \nu) = \int_0^\infty \mathcal{N}(\boldsymbol{x}|\boldsymbol{\mu}, \boldsymbol{\Sigma}/u)\mathcal{G}(u|\nu/2, \nu/2)du, \tag{6.3}$$

where $\mathcal{N}$ and $\mathcal{G}$ denote the Gaussian and Gamma distributions, respectively [194]. The t-distribution is known to be inherently robust compared to the Gaussian distribution because of the 'heavy' tails of the distribution (Fig. 6.1a). This robustness property is illustrated in Fig. 6.1b.

In Eq. (6.3), u can be regarded an implicit latent variable introduced for each observation [195]. In our formulation, these latent variables are denoted by $\boldsymbol{\mathcal{U}}^f = \{u_n^f \in \mathbb{R}\}_{n=1}^{N^f}$ for the 2D points in the f^{th} X-ray image. Similarly, let $\boldsymbol{\mathcal{Z}}^f = \{\boldsymbol{z}_n^f \in \mathbb{R}^M\}_{n=1}^{N^f}$ be the set of latent variables for the 2D points in the f^{th} X-ray image, where $\boldsymbol{z}_n^f$ is a binary 1-of-M vector, whose only non-zero element ($z_{nm}^f = 1$) indicates the model component generating the $\boldsymbol{x}_n^f$.

Assuming statistical independence between the 2D segmented points and the frames, we can write the complete data probability as

$$P(\mathbb{X}, \mathbb{Z}, \mathbb{U}|\boldsymbol{\mathcal{Y}}, \boldsymbol{\mathcal{Q}}) = \prod_{f=1}^{F}\prod_{n=1}^{N^f}\prod_{m=1}^{M}\Big[\pi_m\mathcal{N}\Big(\boldsymbol{x}_n^f|\Theta^f(\boldsymbol{y}_m), \frac{\sigma^2}{u_n^f}\Big)\mathcal{G}\Big(u_n^f|\frac{\nu_m}{2}, \frac{\nu_m}{2}\Big)\Big]^{z_{nm}^f}, \tag{6.4}$$

where $\mathbb{X} = \{\boldsymbol{\mathcal{X}}^f\}_{f=1}^F$, $\mathbb{Z} = \{\boldsymbol{\mathcal{Z}}^f\}_{f=1}^F$, and $\mathbb{U} = \{\boldsymbol{\mathcal{U}}^f\}_{f=1}^F$.

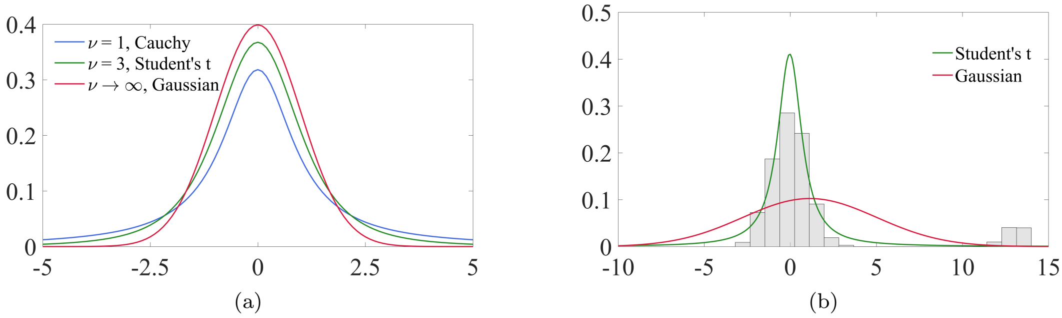

(a) (b)

Figure 6.1: Heavy tails of the Student's t-distribution and its influence on the robust parameter estimation: (a) Plot of Student's t-distribution for different degrees of freedom. The limit $\nu \to \infty$ corresponds to a Gaussian distribution with the same mean and covariance. (b) Maximum-likelihood estimations for data points including outliers are shown in green and red for Student's t-distribution and Gaussian distribution, respectively.

6.2.2.2 Prior on Means

The 3D points describing the coronary artery centrelines should be close to a straight line in a local neighbourhood. We introduce a Bayesian prior on $\boldsymbol{\mathcal{Y}}$ to enforce local linearity of these points, and consequently, to spatially regularise the reconstruction. To this end, a weighted covariance describing the local structure for each 3D point, $\boldsymbol{y}_m$, is defined as

$$\boldsymbol{C}_m = \frac{\sum_{k=1}^{M} \Phi(\boldsymbol{y}_m, \boldsymbol{y}_k)(\boldsymbol{y}_m - \boldsymbol{y}_k)(\boldsymbol{y}_m - \boldsymbol{y}_k)^T}{\sum_{k=1}^{M} \Phi(\boldsymbol{y}_m, \boldsymbol{y}_k)} \tag{6.5}$$

where Φ is a kernel function. In this work, it is given by an isotropic Gaussian with variance η^2,

$$\Phi(\boldsymbol{y}_m, \boldsymbol{y}_k) = \exp\left(\frac{-\|\boldsymbol{y}_m - \boldsymbol{y}_k\|^2}{\eta^2}\right). \tag{6.6}$$

Let $\boldsymbol{e}_{m1}$, $\boldsymbol{e}_{m2}$, and $\boldsymbol{e}_{m3}$ be the eigenvectors of $\boldsymbol{C}_m$ with corresponding eigenvalues $0 \leq \lambda_{m1} \leq \lambda_{m2} \leq \lambda_{m3}$. For vascular structures, the eigenvector with the largest eigenvalue, $\boldsymbol{e}_{m3}$, is expected to point along the longitudinal local orientation. Therefore, we design our local linearity prior to minimise the covariance projected onto the plane spanned by $\boldsymbol{e}_{m1}$ and $\boldsymbol{e}_{m2}$. The projected covariance of the points can be written as the sum of the corresponding eigenvalues,

$\lambda_1 + \lambda_2 = \texttt{tr}(\boldsymbol{W}_m \boldsymbol{C}_m)$, where $\boldsymbol{W}_m = \boldsymbol{e}_{m1}\boldsymbol{e}_{m1}^T + \boldsymbol{e}_{m2}\boldsymbol{e}_{m2}^T$, and `tr` denotes the trace of the matrix. Using this definition, the prior probability is written as

$$P(\boldsymbol{\mathcal{Y}}) = \frac{1}{\omega} \exp\left(\frac{-\beta}{2} \sum_{m=1}^{M} \texttt{tr}(\boldsymbol{W}_m \boldsymbol{C}_m) \right), \tag{6.7}$$

where ω is a normalisation factor, and β is a free parameter.

6.2.2.3 Prior on Mixture Weights

As explained in Chapter 4, the number of mixture model components is a critical parameter of our coronary artery representation. Particularly, the number of mixture model components describing the coronary artery centrelines should be specified in a way that under/overfitting of the probabilistic model is avoided. Intuitively, using an excessive number of components may result in increased flexibility of the model, and consequently overfitting of the probabilistic model. Overfitting is especially a significant problem in our case, since there can be more than one solution because of the ill-posedness of the reconstruction problem. To this end, we introduce a symmetric Dirichlet distribution [165] to enforce sparsity on the mixture weights of the model components [169]. The symmetric Dirichlet prior is written as

$$P(\boldsymbol{\pi}) = \frac{\Gamma(M(N_t(\alpha-1)+1))}{\Gamma(N_t(\alpha-1)+1))^M} \prod_{m=1}^{M} (\pi_m)^{N_t(\alpha-1)} \tag{6.8}$$

where $N_t = \sum_{f=1}^{F} N^f$ is the total number of segmented 2D points, Γ is the Gamma function, and α is the concentration parameter of the distribution. When $\alpha < 1$, π_m's approach zero, and the distribution imposes sparsity on the mixture weights. Sparsity can increase when α is close to $(1 - 1/M)$. To ease the selection of α parameter, we introduce an auxiliary variable $\zeta \in (0, 1)$ to control the sparsity level proportionally, i.e. $\alpha = (1 - 1/M)\zeta + (1 - \zeta)$. Under this formulation, in each parameter estimation step, the negligible mixture components are identified by solving a convex optimisation problem [196], and consequently removed.

6.2.2.4 Estimation of Mixture Model Parameters

Our goal is to maximise the posterior probability for the 3D points describing the coronary artery centreline with respect to mixture model parameters $\boldsymbol{\mathcal{Y}}$ and $\boldsymbol{\mathcal{Q}}$.

The formulation for the maximisation can be written as

$$\boldsymbol{\mathcal{Y}}^*, \boldsymbol{\mathcal{Q}}^* = \underset{\boldsymbol{\mathcal{Y}}, \boldsymbol{\mathcal{Q}}}{\operatorname{argmax}} \ln P(\boldsymbol{\mathcal{Y}}, \boldsymbol{\mathcal{Q}} | \mathbb{X}), \tag{6.9}$$

where logarithm term can be further decomposed as

$$\begin{aligned} \ln P(\boldsymbol{\mathcal{Y}}, \boldsymbol{\mathcal{Q}} | \mathbb{X}) = & \sum_{\mathbb{Z}, \mathbb{U}} q(\mathbb{Z}, \mathbb{U}) \ln \left(\frac{P(\mathbb{X}, \mathbb{Z}, \mathbb{U} | \boldsymbol{\mathcal{Y}}, \boldsymbol{\mathcal{Q}})}{q(\mathbb{Z}, \mathbb{U})} \right) \\ & - \sum_{\mathbb{Z}, \mathbb{U}} q(\mathbb{Z}, \mathbb{U}) \ln \left(\frac{P(\mathbb{Z}, \mathbb{U} | \mathbb{X}, \boldsymbol{\mathcal{Y}}, \boldsymbol{\mathcal{Q}})}{q(\mathbb{Z}, \mathbb{U})} \right) \\ & + \ln P(\boldsymbol{\mathcal{Y}}, \boldsymbol{\mathcal{Q}}) \\ & - \ln P(\mathbb{X}), \end{aligned} \tag{6.10}$$

where q denotes an arbitrary distribution. The final 3D reconstruction of the coronary artery centreline is given by the estimated mean values of the mixture model components, i.e. $\boldsymbol{\mathcal{Y}}^*$.

The MAP estimation of the mixture model parameters can be found using the expectation-maximization (EM) algorithm (Algorithm 1) [172][1]. A lower bound of the function in Eq. (6.9) can be obtained by setting the Kullback-Leibler divergence described by second term in Eq. (6.10) to zero, and ignoring the constant last term. The lower bound is given by

$$\boldsymbol{\mathcal{Y}}^*, \boldsymbol{\mathcal{Q}}^* = \underset{\boldsymbol{\mathcal{Y}}, \boldsymbol{\mathcal{Q}}}{\operatorname{argmax}} E_{\mathbb{Z}, \mathbb{U}} \{ \ln P(\mathbb{X}, \mathbb{Z}, \mathbb{U} | \boldsymbol{\mathcal{Y}}, \boldsymbol{\mathcal{Q}}) | \mathbb{X}, \hat{\boldsymbol{\mathcal{Y}}}, \hat{\boldsymbol{\mathcal{Q}}} \} + \ln P(\boldsymbol{\mathcal{Y}}) + \ln P(\boldsymbol{\pi}), \tag{6.11}$$

where a hat over the symbol, $(\hat{\cdot})$, identifies the mixture model parameters from the previous iteration of the EM algorithm. This lower bound is maximised with respect to $\boldsymbol{\mathcal{Y}}, \boldsymbol{\mathcal{Q}}$.

To compute the expectation of the complete data log-likelihood in Eq. (6.11), the expectations of the latent variables, given the data and the values of the model parameters from the previous iteration, are computed in the E-step of the

---

[1] In fact, we use the expectational-conditional-maximisation (ECM) algorithm [197]. However, due to the structure of the complete data log-likelihood in Eq. (6.17), it reduces to EM algorithm. For a detailed discussion, the reader is referred to [198].

EM algorithm [198] as follows:

$$\gamma^f_{nm} = E_{z^f_{nm}}\{z^f_{nm}|\boldsymbol{x}^f_n, \hat{\boldsymbol{\mathcal{Y}}}, \hat{\boldsymbol{\mathcal{Q}}}\} = \frac{\hat{\pi}_m \boldsymbol{\mathcal{S}}(\boldsymbol{x}^f_n|\Theta^f(\hat{\boldsymbol{y}}_m), \hat{\sigma}^2, \hat{\nu}_m)}{\sum_{m=1}^{M} \hat{\pi}_m \boldsymbol{\mathcal{S}}(\boldsymbol{x}^f_n|\Theta^f(\hat{\boldsymbol{y}}_m), \hat{\sigma}^2, \hat{\nu}_m)}, \tag{6.12}$$

$$\tau^f_{nm} = E_{u^f_n}\{u^f_n|z^f_{nm} = 1, \boldsymbol{x}^f_n, \hat{\boldsymbol{\mathcal{Y}}}, \hat{\boldsymbol{\mathcal{Q}}}\} = \frac{\hat{\nu}_m + 2}{\hat{\nu}_m + \|\boldsymbol{x}^f_n - \Theta^f(\hat{\boldsymbol{y}}_m)\|^2/\hat{\sigma}^2}, \tag{6.13}$$

$$E_{u^f_n}\{\ln u^f_n|z^f_{nm} = 1, \boldsymbol{x}^f_n, \hat{\boldsymbol{\mathcal{Y}}}, \hat{\boldsymbol{\mathcal{Q}}}\} = \Psi\left(\frac{\hat{\nu}_m + 2}{2}\right) - \ln\left(\frac{\hat{\nu}_m + 2}{2}\right) + \ln \tau^f_{nm}. \tag{6.14}$$

Using these expectations, one can write the expectation term in Eq. (6.11) as

$$\begin{aligned}
&E_{\mathbb{Z},\mathbb{U}}\{\ln P(\mathbb{X}, \mathbb{Z}, \mathbb{U}|\boldsymbol{\mathcal{Y}}, \boldsymbol{\mathcal{Q}})|\mathbb{X}, \hat{\boldsymbol{\mathcal{Y}}}, \hat{\boldsymbol{\mathcal{Q}}}\} \approx \qquad (6.15)\\
&\sum_{f=1}^{F}\sum_{n=1}^{N^f}\sum_{m=1}^{M} \gamma^f_{nm} \ln \pi_m \sum_{f=1}^{F}\sum_{n=1}^{N^f}\sum_{m=1}^{M} \gamma^f_{nm}\Big[- \ln \Gamma\left(\frac{\nu_m}{2}\right) + \frac{\nu}{2} \ln \frac{\nu}{2}\\
&+ \frac{\nu}{2}\left(\Psi\left(\frac{\hat{\nu}_m + 2}{2}\right) - \ln\left(\frac{\hat{\nu}_m + 2}{2}\right) + \ln \tau^f_{nm} - \tau^f_{nm}\right)\Big]\\
&+ \sum_{f=1}^{F}\sum_{n=1}^{N^f}\sum_{m=1}^{M} \gamma^f_{nm}\Big[- \ln 2\pi + \ln \sigma^{-2} - \frac{1}{2}\tau^f_{nm}\frac{\|\boldsymbol{x}^f_n - \Theta^f(\boldsymbol{y}_m)\|^2}{\sigma^2}\Big],
\end{aligned}$$

ignoring the terms that does not depend on $\boldsymbol{\mathcal{Y}}$, $\boldsymbol{\mathcal{Q}}$.

In the M-step of EM algorithm, the lower bound in Eq. (6.11) is maximised with respect to $\{\boldsymbol{\mathcal{Y}}, \boldsymbol{\pi}, \sigma^2, \boldsymbol{\nu}\}$. To compute $\boldsymbol{y}_m$'s, the derivative of Eq. (6.11) is taken with respect to $\boldsymbol{y}_m$ and set to zero, i.e.

$$\sum_{f=1}^{F}\sum_{n=1}^{N^f} \gamma^f_{nm}\tau^f_{nm}(\boldsymbol{x}^f_n - \Theta^f(\boldsymbol{y}_m))\frac{\partial \Theta^f(\boldsymbol{y}_m)}{\partial \boldsymbol{y}_m} + \beta \sum_{k=1}^{M}(\Phi_{mk}\boldsymbol{W}_m + \Phi_{km}\boldsymbol{W}_k)(\boldsymbol{y}_m - \boldsymbol{y}_k) = 0, \tag{6.16}$$

where $\Phi_{il} = \Phi(\boldsymbol{y}_i, \boldsymbol{y}_l)/\sum_{j=1}^{M}\Phi(\boldsymbol{y}_i, \boldsymbol{y}_j)$. The solution of Eq. (6.16) for $\boldsymbol{y}_m$ is approximated by fixing $\{\boldsymbol{W}_m\}_{m=1}^{M}$. The $\boldsymbol{y}_m$'s are sequentially computed, and $\{\boldsymbol{W}_m\}_{m=1}^{M}$ are updated after computation of each $\boldsymbol{y}_m$.

For a weak-perspective camera model, the Jacobian of the projection function in Eq. (6.16) does not depend on $\boldsymbol{y}_m$. On the other hand, the Jacobian is a function of $\boldsymbol{y}_m$ for the perspective camera model, necessitating numerical optimisation to compute $\boldsymbol{y}_m$ under perspective camera model. Therefore, we first obtain a closed-form solution for the weak-perspective model. and subsequently use it for numerical solution of Eq. (6.16), thus satisfying the perspective model constraints in our reconstruction. For weak-perspective camera model, Eq. (6.16) can be organised to obtain a closed form solution, which is given by

$$\begin{aligned}\left(\sum_{f=1}^{F}\sum_{n=1}^{N^f}\gamma_{nm}^{f}\tau_{nm}^{f}(\boldsymbol{Q}^f)^T\boldsymbol{Q}^f+\beta\sum_{k=1}^{M}(\Phi_{mk}\boldsymbol{W}_m+\Phi_{km}\boldsymbol{W}_k)\right)\boldsymbol{y}_m= & \qquad (6.17)\\ +\sum_{f=1}^{F}\sum_{n=1}^{N^f}\gamma_{nm}^{f}\tau_{nm}^{f}(\boldsymbol{Q}^f)^T\boldsymbol{x}_n^f+\beta\sum_{k=1}^{M}(\Phi_{mk}\boldsymbol{W}_m+\Phi_{km}\boldsymbol{W}_k)\boldsymbol{y}_k. &\end{aligned}$$

Similarly, the derivative of (Eq. 6.11) is taken with respect to π_m after introducing Lagrange multipliers to enforce the constraint and setting it to zero. Organising the terms, the mixture weights can be computed using

$$\bar{\pi}_m=\frac{(\alpha-1)+((\sum_{f=1}^{F}\sum_{n=1}^{N^f}\gamma_{nm}^{f})/N_t)}{M(\alpha-1)+1}. \qquad (6.18)$$

When $\alpha=1$, Eq. (6.18) reduces to the maximum-likelihood estimation of mixture weights. On the other hand, for $(1-1/M)\leq\alpha$, if $(\sum_{f=1}^{F}\sum_{n=1}^{N^f}\gamma_{nm}^{f})/N_t<1-\alpha$, then we obtain invalid negative mixture weights, i.e. $\widehat{\pi}_m<0$. To solve the problem, mixture weights that are estimated using Eq. (6.17) are updated via the following convex optimisation problem

$$\begin{aligned}\pi_1,\ldots,\pi_M=\underset{\pi_1,\ldots,\pi_M}{\operatorname{argmin}}\sum_{m=1}^{M}(\bar{\pi}_m-\pi_m)^2,&\\ s.t.\sum_{m=1}^{M}\pi_m=1\wedge 0\leq\pi_m\forall m,& \qquad (6.19)\end{aligned}$$

which is solved using the generalised sequential minimal optimiser proposed in [196]. Eq. (6.19) finds the orthonormal projection of $\bar{\boldsymbol{\pi}}$ on the space of eligible probabilities, and sets the negative probabilities to 0. Note that the number of zero mixture weights (sparsity) can increase when α is close to $(1-1/M)$. To ease the selection of α parameter, we introduce an auxiliary variable $\zeta\in(0,1)$ to control the sparsity level, i.e. $\alpha = (1 - 1/M)\zeta + (1 - \zeta)$. At the end of the M-step, the mixture components with zero mixture weights are identified and pruned out.

The derivative of Eq. (6.11) is taken with respect to σ, and set to zero in order to compute the σ^2 as

$$\sigma^2 = \frac{\frac{1}{2}\sum_{f=1}^{F}\sum_{n=1}^{N^f}\sum_{m=1}^{M}\gamma_{nm}^f\tau_{nm}^f\|\boldsymbol{x}_n^f - \Theta_f(\boldsymbol{y}_m)\|^2}{\sum_{f=1}^{F} N^f}. \tag{6.20}$$

Finally, the derivative of Eq. (6.11) is taken with respect to ν_m, and set to zero. Organising the terms, ν_m can be computed as the solution to the following nonlinear equation

$$\begin{aligned} &-\Psi\left(\frac{\nu_m}{2}\right) + \ln\left(\frac{\nu_m}{2}\right) + 1 + \Psi\left(\frac{\hat{\nu}_m}{2}\right) + \ln\left(\frac{\hat{\nu}_m}{2}\right) \\ &+ \frac{1}{\sum_{f=1}^{F}\sum_{n=1}^{N^f}\gamma_{nm}^f}\left(\sum_{f=1}^{F}\sum_{n=1}^{N^f}\gamma_{nm}^f(\ln\tau_{nm}^f - \tau_{nm}^f)\right) = 0. \end{aligned} \tag{6.21}$$

After each EM cycle, convergence is monitored by computing the Euclidean distance between the current and the previous values of the component means. EM algorithm stops when the distance for each mixture component is smaller than a threshold (t_{conv} in mm). The overall algorithm is given in Algorithm 2.

6.2.3 Reconstruction of the Coronary Trees

The previous step computes the 3D points representing the means of the mixture of the t-distributions. These points are further processed to obtain the 3D coronary artery centrelines. To this end, we compute the minimum spanning arborescence of a directed graph, whose vertices are the reconstructed points and edges are the possible connections between the neighbouring points. One of the reconstructed points is manually selected as the root of the graph. The graph is built by connecting the root to all the remaining points, and each point to its neighbours inside a 10 mm neighbourhood. The edge weights of the graph are determined by the Euclidean distance between the connecting points. Following the computation of minimum spanning arborescence using Edmonds algorithm [174], automatic pruning steps are applied to obtain the final coronary arterial tree. Specifically, short coronary branches are removed, and a cubic spline is fitted to each branch of the

Algorithm 2 3D Coronary artery centreline reconstruction algorithm

```
Input
  $\mathbb{X} = \{\boldsymbol{\mathcal{X}}^f\}_{f=1}^F$: 2D centreline points segmented from $F$ retrospectively gated X-ray images
  $\{\Theta^f\}_{f=1}^F$: Projection functions for $F$ retrospectively gated X-ray images
  $\boldsymbol{\mathcal{Y}}_{ini}, \boldsymbol{\mathcal{Q}}_{ini}$: Initial mixture model parameters
  $\beta, \eta, \zeta,$: Spatial regularisation parameter, standard deviation of the kernel function, and sparsity parameter
  $t_{conv}$: Convergence threshold
Output
  $\boldsymbol{\mathcal{Y}}^*, \boldsymbol{\mathcal{Q}}^*$: Estimates of mixture model parameters
MAP estimation via EM algorithm
  $\boldsymbol{\mathcal{Y}}^* \leftarrow \boldsymbol{\mathcal{Y}}_{ini}$, $\boldsymbol{\mathcal{Q}}^* \leftarrow \boldsymbol{\mathcal{Q}}_{ini}$
  Compute $\boldsymbol{W}_m \quad \forall m \in \{1 \dots M\}$
  repeat
      $\hat{\boldsymbol{\mathcal{Y}}} \leftarrow \boldsymbol{\mathcal{Y}}^*$, $\hat{\boldsymbol{\mathcal{Q}}} \leftarrow \boldsymbol{\mathcal{Q}}^*$
      Update $\gamma_{nm}^f$ and $\tau_{nm}^f$ (Eq. (6.12) and (6.13))
      for $m = 1 \dots M$ do
          Update $\boldsymbol{y}_m^*$ by solving Eq. (6.14)
          Update $\boldsymbol{W}_k \quad \forall k \in \{1 \dots M\}$.
      end for
      Update $(\sigma^2)^*$
      Update $\boldsymbol{\pi}^*$
      for $m = 1 \dots M$ do
          if $\pi_m^* = 0$ then
              Remove $m^{th}$ mixture model component
          end if
      end for
      Update $\boldsymbol{\nu}^*$
  until $||\boldsymbol{y}_m^* - \hat{\boldsymbol{y}}_m|| \leq t_{conv} \quad \forall m \in \{1 \dots M\}$
```

coronary arterial tree.

6.3 Experiments

6.3.1 Error Metrics

The reconstruction accuracy is measured in terms of centreline to centreline distance metrics, namely the 2D reprojection ($\mathrm{RPE}_{\mathrm{2D}}$) and the 3D space errors ($\mathrm{SE}_{\mathrm{3D}}$). The evaluation metrics are defined in terms of point-to-point correspondences between the reconstructed and ground truth 2D/3D centrelines. For each reconstructed point, a corresponding ground truth point is identified, which is selected as the closest point on 2D/3D ground truth. $\mathrm{RPE}_{\mathrm{2D}}/\mathrm{SE}_{\mathrm{3D}}$ is defined as the average of 2D/3D Euclidean distances between the 2D/3D reconstructed centrelines and their corresponding ground truth points.

6.3.2 Synthetic Data Experiments

Quantitative validation is carried out by means of a comprehensive phantom study. To this end, we generated two synthetic X-ray rotational angiography sequences using the left coronary artery geometry of 4D XCAT phantom [147]. Information related to image acquisition, namely number of images (117), frame rate (30 fps), angular coverage (60° RAO to 60° LAO with 25° CRA angulation), and the parameters defining the geometry model, corresponded to typical values in a clinical rotational angiography dataset. The generation process of the first sequence is the same as the one described in Chapter 4. In the first sequence (`CardiacSeq`), we simulated cardiac motion where we set the heart beat rate to 70 beats per minute. The 3D splines describing the 3D coronary artery centrelines for each time step of the sequence are projected onto 2D views. Synthetic 2D centreline segmentations were generated by sampling 2D points from the corresponding 2D splines every 1.0 mm. Instead of using a rectangular gating window as in Chapter 4, we performed ECG gating on this sequence using a nearest neighbour gating window, where the reference cardiac phase is selected as end-diastole. Effectively, a total of 5 images with corresponding 2D centreline segmentations (`CardiacSet`) were selected for reconstruction. Although this process selects projection images with equiangular increments due to the regular heart beat, this is not a requirement for our method, as the method can handle segmentations from arbitrary views. In the second sequence (`StaticSeq`), we employed the static geometry of the coronary arteries at end-diastole to generate the sequence. For the experiments involving the static sequence, we selected the images and the 2D centreline segmentations (`StaticSet`) that are acquired from the same views that are selected for the `CardiacSet`.

Having the synthetic data, we perform four sets of experiments assessing reconstruction using variable data qualities obtained with: different angular densities, noisy centreline segmentations, outliers in the segmented centrelines, and the artery motion.

6.3.2.1 Angular Density of X-ray Images

In this experiment, we selected a number of X-ray images and their corresponding 2D centreline segmentations from `StaticSeq` ($F \in \{3, 4, 5\}$) such that F images cover the full angular range with equal angular increments.

6.3.2.2 Noisy 2D Centreline Segmentations

The 2D centreline segmentations employed in the reconstruction inevitably include errors. This experiment is designed to understand the advantage of our probabilistic formulation and the priors in the presence of segmentation errors. For this purpose, we added zero mean Gaussian noise with standard deviations ranging from 0.25 mm to 1.00 mm to the 2D centreline segmentations of the `StaticSet`, and computed the reconstructions. The reconstruction experiments were repeated 10 times at each noise level.

6.3.2.3 Structured Outliers in 2D Centreline Segmentations

Some of the 2D segmentations may include extra branches with no corresponding points in other views. Furthermore, some parts of the 2D segmentations may not correspond to actual centreline structures. Instead, these parts are erroneously segmented from the background structures in X-ray images. In this experiment, we aim at understanding the behaviour of our method in such scenarios, where we have such outliers. To generate realistic outlier points, smooth random curves that mimics the shape of the 2D coronary artery centreline branches were generated and outliers points are sampled from these curves. To this end, random trajectories of particles having Brownian motion were generated and smoothed by fitting cubic Hermite splines. The outliers points were then sampled from these splines at 1.0 mm, which is the same sampling rate to generate the synthetic segmentations. These outlier points were added to each of the corresponding 2D centreline segmentations of the `StaticSet` (Fig. 6.5a). The number of additional outlier points was varied from 0% to 30% of the number of points in the 2D centreline segmentations. Similar to the previous experiment, the reconstructions were computed 10 times with different outlier points at each outlier level.

6.3.2.4 Residual Artery Motion

To examine the accuracy of our method under residual cardiac motion, we use the images from the `CardiacSeq`. This sequence was deliberately generated such that any image in the sequence is acquired at a unique cardiac phase, different to others. As a result, the X-ray images selected by ECG gating correspond to slightly different cardiac motion states. First, we reconstructed coronary arteries using the 2D segmentations of `CardiacSet`, which are selected using a nearest neighbour gating window. Following this benchmark reconstruction, we computed reconstructions with images selected using gating windows of size 10% and 20% of the cardiac cycle around end-diastole.

6.3.3 Clinical Data Experiments

To illustrate the clinical feasibility of our method, a set of experiments is performed using real X-ray rotational angiography data. The data were collected with a Philips Allura Xper C-Arm X-ray system (Philips Healthcare, Best, The Netherlands) at the Northern General Hospital (Sheffield, United Kingdom). The X-ray system is calibrated periodically to ensure accurate acquisition geometry parameters. The X-ray images were collected during hand injection of intravenous contrast agent. Patients were asked to hold their breaths during the acquisition. C-Arm rotation covered a range from RAO 60° to LAO 60° with 25° cranial or caudal angulation and the rotation was completed in approximately 4 s at 30 fps, resulting in 117 images per study. The X-ray images have a size of 960 × 960 pixels with an isotropic pixel spacing of 0.184 mm. A simultaneous ECG signal was also recorded during the acquisition, and a subset of images was selected via a retrospective ECG gating at end-diastolic or end-systolic cardiac phase for further processing. The number of gated images was 3-4 using nearest-neighbour gating window.

To extract coronary arteries from retrospectively gated X-ray angiography images, we employed a segmentation workflow, which consists of simple image processing algorithms, similar to the ones proposed in [64, 96]. Specifically, the X-ray images are smoothed with coherence enhancing diffusion filter [199], and then their vesselness [189] is computed. Directional non-maximum suppression is applied on the vesselness image followed by hysteresis thresholding. The resulting binary segmentations are connected using morphological operations, and the connected components smaller than a threshold are removed. The output of the segmentation workflow is inspected by an expert, and obvious errors (e.g. segmented parts of catheter or branch connections) are manually corrected. A total of 10 X-ray angiography studies (5 LCAs, 5 RCAs) were processed using the segmentation workflow.

We performed two experiments in total to qualitatively and quantitatively validate the proposed method.

6.3.3.1 Experiments without Outliers

Although the cumulative effect of heavy tails of t-distributions, sparsity and spatial regularisation priors renders the proposed method robust to outliers, the reconstructed centrelines can be further improved if better segmentations (free from obvious errors or missing parts) are provided. Moreover, clean segmentations facilitate a fair comparison of our results with the relevant literature, since the methods in the literature generally assume that accurate and clean segmentations are available. In this experiment, the 3D reconstruction was computed using the 2D segmentations which were obtained using the segmentation workflow described above, and further processed to remove all the outliers from 2D centreline segmentations.

6.3.3.2 Experiments with Outliers

Segmentation of the coronary arteries from X-ray angiography is prone to errors. The resulting segmentations can be degraded with the addition of erroneously segmented structures (outliers). In this experiment, the reconstruction was computed using the 2D segmentations from the segmentation workflow, which include outlier points. Specifically, we deliberately preserved some of the extra branches in the 2D segmentations, which are not visible in all the X-ray images due to contrast wash-in/out (Fig. 6.7b). The average number of outlier points for our clinical dataset was 22.7% of the number of total points in the 2D segmentations.

Table 6.1: Parameter settings for the experiments using synthetic and clinical data.

	Synthetic	Clinical
F	$3-5$	$3-4$
M	252	$\{84, 126, 168, 210\}$
$\boldsymbol{\mathcal{Y}}_{ini}$	Points from regular spatial grid	Points from regular spatial grid
σ_{ini}	60 mm	60 mm
$\boldsymbol{\pi}_{ini}$	$\pi_m = 1/M$ $\forall m \in \{1 \ldots M\}$	$\pi_m = 1/M$ $\forall m \in \{1 \ldots M\}$
$\boldsymbol{\nu}_{ini}$	3	3
β	[0.00 0.20]	$\{0.05, 0.10, 0.20\}$
ζ	[0.00 0.01]	$\{0.025, 0.050, 0.075\}$
η	5 mm	5 mm
t_{conv}	0.001 mm	0.01 mm

6.3.4 Initialisation

To initialise the number of mixture model components and corresponding mean values, we selected M points on a regular grid in spherical coordinates centred at the origin of the patient coordinate system (Fig. 6.5b). By changing the radial sampling rate of the grid, we can adjust the number of parameters and the initial mean values. The number of model components were selected empirically. We fixed M to 252 for the synthetic data experiments, whereas we tried different numbers of model components for the clinical data experiments. Moreover, the initial value of the component variance is set to a high value. Finally, the mixture weights are selected uniformly such that they sum to one.

In synthetic data experiments, we performed experiments with varying degrees of β and ζ to study the effect of spatial regularisation and sparsity, and reported the results. For the clinical data experiments, we conducted experiments with varying degrees of β, ζ and M, and then selected the reconstruction with the smallest average $\mathrm{RPE}_{\mathrm{2D}}$. The parameter settings for the experiments using synthetic and clinical data is summarised in Table 6.1.

6.4 Results

6.4.1 Results on Synthetic Data

The results of the experiments using different angular density of X-ray images, noisy centreline segmentations, centreline segmentations with outliers, and the artery motion (Section 6.3.2) are given below.

6.4.1.1 Angular Density of X-ray Images

Table 6.2 summarises the $\mathrm{SE}_{\mathrm{3D}}$ for the reconstructions obtained with different numbers of X-ray images covering the full angular span. The best reconstruction is achieved at $\zeta = 0.00$, $\beta = 0.05$ with 5 gated X-ray images and has an error of 0.085 mm. In general, the highest reconstruction accuracies were achieved with 4-5 gated X-ray images. These results indicate that the proposed method can work be successfully applied to typical X-ray rotational angiography data, with 3-5 gated X-ray images per cardiac phase.

Table 6.2: The effect of angular density of X-ray images on the reconstruction accuracy: 3D space Errors (mm) are shown for varying degrees of sparsity (ζ) and spatial regularisation (β).

# of	ζ		0.00			0.10	
images	β	0.00	0.05	0.20	0.00	0.05	0.20
3		0.200	0.230	0.141	0.202	0.196	0.139
4		0.110	0.100	0.128	0.103	0.099	0.116
5		0.112	0.085	0.152	0.088	0.090	0.155

The results also show that when the number of images is low, increasing both the sparsity level and the spatial regularisation improves the reconstruction accuracy, justifying the additional value of the prior information. However, when there are more than 3 X-ray images, increasing the spatial regularisation causes some artifacts, particularly in the regions where two branches are close to each other. Some results are shown in Fig. 6.2d to demonstrate the effect of spatial regularisation.

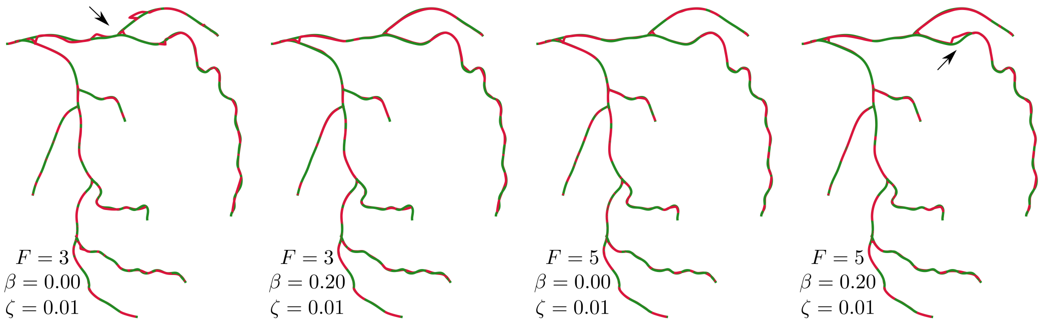

(a) (b) (c) (d)

Figure 6.2: The effect of angular density of X-ray images on the reconstruction: The ground truth centrelines are shown in green, whereas reconstructed centrelines are shown in red. (a)-(b) The spatial regularisation prior improves the reconstruction when the number of X-ray images is low. (c)-(d) However, with sufficient X-ray images, increasing spatial regularisation excessively may cause reconstruction artifacts.

6.4.1.2 Noisy 2D Centreline Segmentations

Fig. 6.3 shows the the $\mathrm{SE}_{3\mathrm{D}}$ for the reconstructions obtained when each of the points in the 2D centreline segmentations are degraded by zero mean Gaussian noise. The median error increases from 0.117 to 0.7334 mm (with $\zeta = 0.01$, $\beta = 0.01$), when we increase standard deviation of the noise from 0.00 to 1.00 mm. In particular, the reconstructions obtained with up to 0.50 mm noise are still comparable to baseline. This implies that the probabilistic formulation of the reconstruction can handle noisy centreline segmentations.

The results also demonstrate the effect of the spatial regularisation prior (β). With noise levels up to 0.50 mm standard deviation, increasing β excessively deteriorates the reconstructions, similar to the previous experiment. However, in the presence of noise with 1.00 mm standard deviation, increasing this term improves the resulting reconstructions as expected.

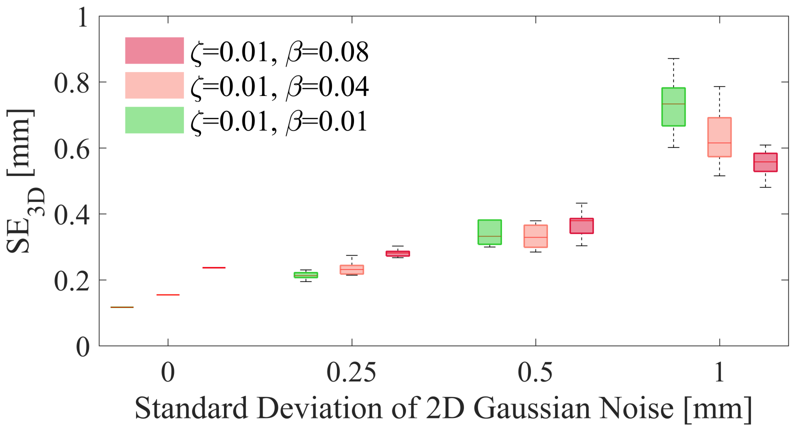

Figure 6.3: The effect noisy in 2D centreline segmentations on the 3D reconstruction accuracy: 3D space errors (mm) are calculated using reconstructions with varying levels of sparsity (ζ) and spatial regularisation (β) priors.

6.4.1.3 Structured Outliers in 2D Centreline Segmentations

Fig. 6.4 shows the $\mathrm{SE}_{3\mathrm{D}}$ for the reconstructions obtained when varying levels of additional outlier points were added to the 2D centreline segmentations. The median error only marginally increases from 0.119 to 0.241 mm (with $\zeta = 0.01$, $\beta = 0.20$), as we increase the outlier percentage from 0% to 30%. The results obtained without prior information ($\zeta = 0.00$, $\beta = 0.00$) signify that the heavy tails of the t-distributions behave as expected, providing robustness against outliers. Furthermore, the prior information complements the effect of the heavy-tails. Specifically, increasing the spatial regularisation consistently decreases the dispersion of the $\mathrm{SE}_{3\mathrm{D}}$ in all outlier levels. On the other hand, the positive effect of the sparsity prior can only be perceived when the outlier level is high.

In Fig. 6.4, a substantial increase in the dispersion of the error can be observed when the outlier percentage is increased to 30%. As we increase the outlier level, the reconstructed points may contain some scattered points due to overfitting (Fig. 6.5). This can be explained as follows: The possibility of finding consistent point correspondences between various projection frames increases when a large amount of outliers is present in the segmentations. As a result, some mixture model components are displaced towards those outliers. This situation can be rectified to some extent by increasing the sparsity level, since this term mainly

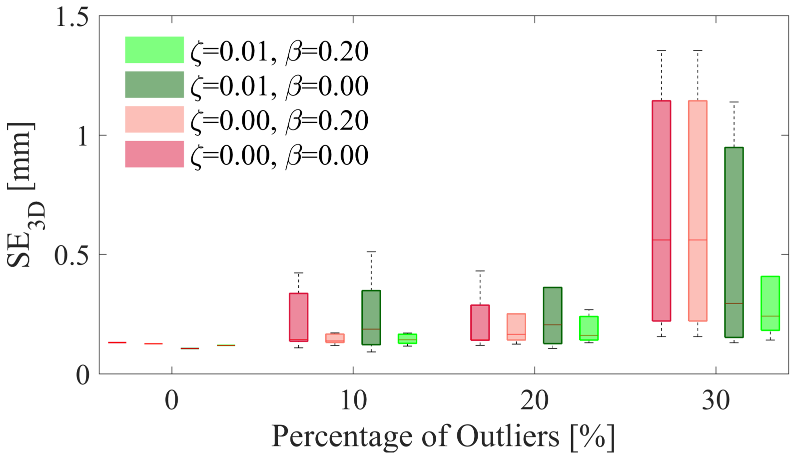

Figure 6.4: The effect of outliers in 2D centreline segmentations on the reconstruction accuracy: 3D space errors (mm) are calculated for varying degrees of additional outlier points, and with/without sparsity (ζ) and spatial regularisation (β) priors.

avoids overfitting by decreasing the number of model points and, consequently, the flexibility of the mixture model.

6.4.1.4 Residual Artery Motion

Fig. 6.6 shows the reconstruction errors when there is residual cardiac motion in the gated X-ray images. The reconstructions are computed using X-ray images selected by gating windows of size 0% (nearest neighbour), 10% and 20% of the cardiac cycle (with $\zeta = 0.01$, $\beta = 0.05$), and SE$_{3D}$ is computed by comparing reconstructions with the ground truth 3D centrelines at cardiac phases immediately above and below the reference cardiac phase.

The minimum SE$_{3D}$ for the reconstruction using nearest neighbour window is 0.114 mm, and achieved at the reference cardiac phase. Additionally, this result is close to the error for the corresponding reconstruction without cardiac motion (0.090 mm, Table 6.2). If 10% gating window is utilised, the error obtained at the reference phase increases to 0.161 mm. These errors suggest that the proposed method can compute an average model at the reference cardiac phase for small gating windows. As we further increase the width of the gating window to 20%,

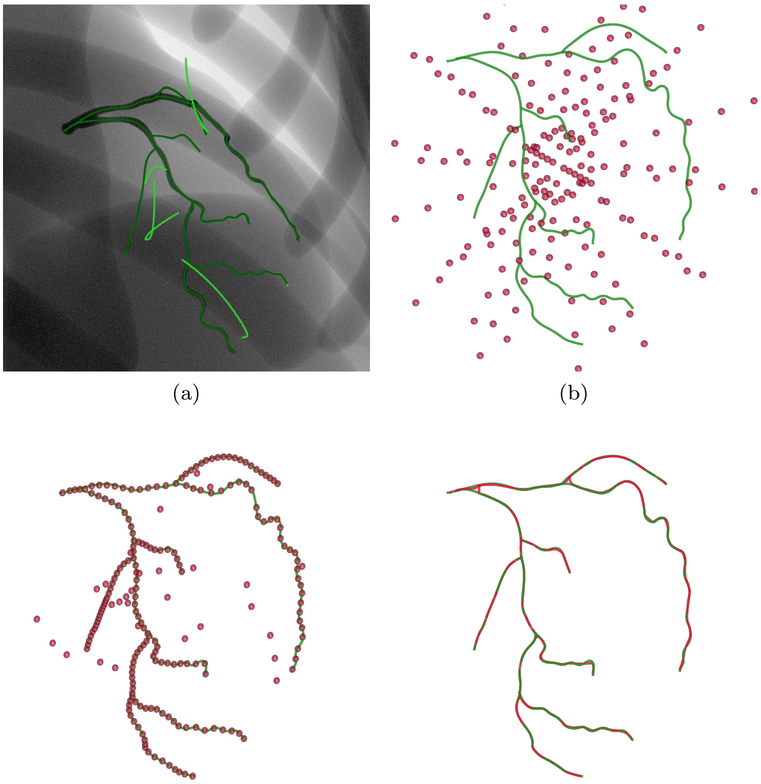

(a) (b)

(c) (d)

Figure 6.5: The effect of structured outliers in 2D centreline segmentations on the 3D reconstruction: (a) An example synthetic X-ray angiogram and the corresponding 2D segmentations (dark green) with outliers (light green). (b) Initialisation of the mixture model components. (c) Reconstructed points at 30% outlier level. (d) Pruned final reconstruction. The ground truth centrelines are shown in green, whereas reconstructed points or centrelines are shown in red.

our reconstruction method can no longer guarantee that the reconstruction at the reference cardiac phase is optimal.

6.4.2 Results on Clinical Data

The results of the experiments using real X-ray rotational angiography data without and with outliers (Section 6.3.3) are presented below.

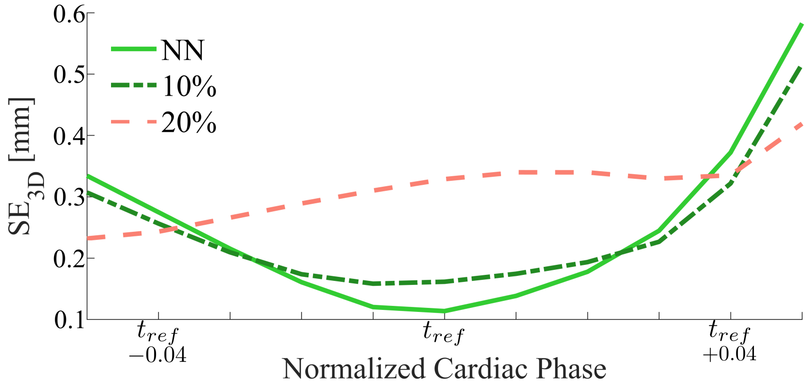

Figure 6.6: The effect of residual cardiac motion due to finite gating accuracy on the reconstruction accuracy: Coronary arteries are reconstructed using 2D centreline segmentations from X-ray images that are selected using gating windows covering 0% (Nearest Neighbour), 10% and 20% of the cardiac cycle ($\zeta = 0.01$, $\beta = 0.05$). The reconstructed coronary arteries are compared with the ground truth 3D centrelines at cardiac phases above and below the reference cardiac phase ($t_{ref} \in [0, 1)$).

6.4.2.1 Experiments without Outliers

The mean and standard deviation of the RPE$_{2D}$ values for the reconstructions of 10 coronary artery trees are given in Table 6.3. The proposed method achieved 0.428 mm mean error and 0.387 mm median error, whereas the minimum and maximum errors were 0.206 and 0.716 mm, respectively. Projections of the reconstructions onto X-ray images for the best and the worst cases are shown in Fig. 6.7a. For the best reconstruction, the projections perfectly fit the ground truth, whereas, for the worst case, there is a perceivable translation between the projections and the ground truth. This is possibly due to strong residual motion (breathing, patient movement), as investigated in Section 6.4.1.4. Nevertheless, the proposed method successfully generated an average model, and the overall shape of the artery was correctly reconstructed.

6.4.2.2 Experiments with Outliers

In the presence of the outliers, for the data set of 10 coronary artery trees, the method achieved 0.486 mm mean RPE$_{2D}$ with a standard deviation of 0.168 mm (cf. Table 6.3), and the median error of 0.431 mm. The cases with the minimum

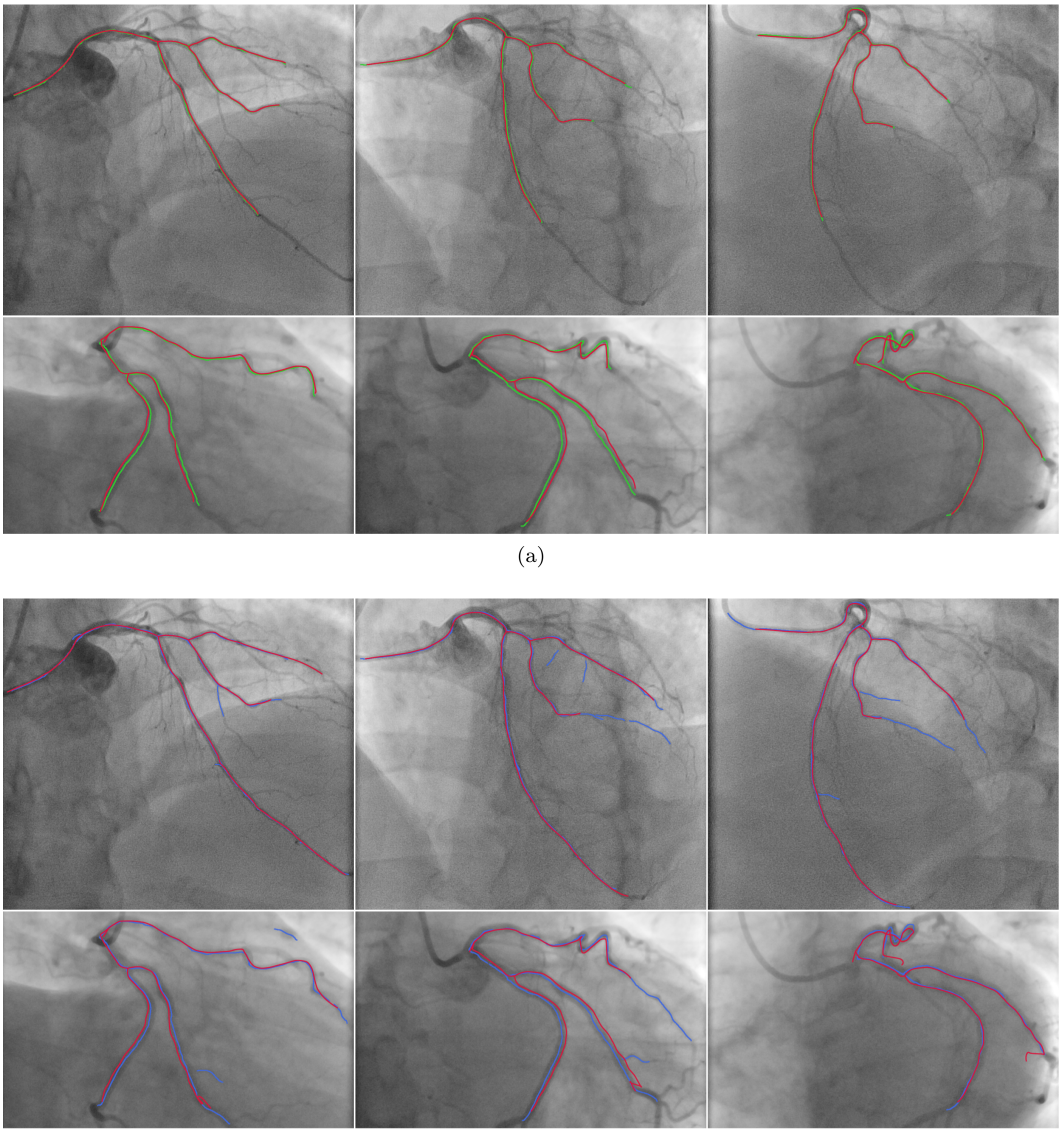

(a)

(b)

Figure 6.7: Projections of reconstructions onto X-ray images: The cases with the minimum and maximum reprojection errors are shown for the experiments (a) without/ (b) with outliers. (a) The ground truth centrelines are shown in green. (b) The input segmentations are shown in blue. In both (a) and (b), the projections of the reconstruction are delineated in red.

and maximum errors did not change with respect to the previous experiment. This time, the minimum and maximum $\mathrm{RPE}_{\mathrm{2D}}$ were 0.239 and 0.825 mm, respectively. Similar to the previous experiment, the projections of the reconstructions for the best and the worst reconstructions are shown in Fig. 6.7b. The $\mathrm{RPE}_{\mathrm{2D}}$ values obtained for the experiments without and with outliers does not change immensely, which verifies the method's robustness in the clinical dataset. However, for some arteries, reconstruction artifacts were noticeable at the distal end of some branches (Fig. 6.7b). This can be attributed to method's previously explained behaviour in the presence of a large number of outliers (Section 6.4.1.3).

One should note that the 2D reprojection error does not take the amount of overlap between the ground truth centrelines and the projections of the reconstructed centrelines [192]. Nonetheless, we did not observe any excessively pruned reconstructions in our experiments. The method was able to establish correspondences of 2D points as long as they are segmented from all views (Fig. 6.7b).

6.4.3 Comparison with the Literature

The proposed method is compared with the state-of-the-art model-based 3D coronary artery reconstruction methods. The results on the synthetic and clinical data, given in Table 6.3 for various methods, were obtained using different datasets due to lack of a standardised validation dataset. Nonetheless, they show the accuracies of the various techniques. Our method achieved superior accuracy on the synthetic data, and comparable results on the clinical data.

The methods in the literature differ in terms of the required level of interaction. Methods based on active contour model [80, 81] require clean 2D centreline segmentations from 2-5 X-ray images to define the external forces. These segmentations can typically be obtained by semi-automatic segmentation algorithms. In addition, these methods need manual initialisation of the active contour for each coronary branch. Multi-view stereo based reconstruction method described in [96] can work with automatically extracted centreline segmentations from 4-5 X-ray images. Specifically, this method estimates a depth value for each centreline point at a reference image given the segmentations for the other images. Therefore, it is important to manually correct any errors in the segmentation of the reference frame. Alternatively, method in [100] is based on back-projection of vesselness responses, and does not need centreline segmentations. However, this method requires 8-9 X-ray images to reduce the noise in the back-projection, and thus is appropriate for reconstruction from rotational angiography with high angular

Table 6.3: Comparison of the proposed method with the state-of-the-art model-based 3D coronary artery reconstruction methods. (See the text for further details.)

	Protocol				**Gating**	**Input**	**Results**			
							Synthetic	**Real**		
	Angio. Type	ECG	Cal.	Angular Span	# of images	Level of User Interaction	SE_{3D} (mm)	# of cases	RPE_{2D} (mm)	Time
[100]	Rotational	✓	✓	180°	8-9	Auto	0.200	17	-	4 sec
[96]	Rotational	✓	✓	100° RAO to 100° LAO, 0° CRA/CAU	4-5	Medium	0.390	11	1.183 ± 0.262	12 sec
[81]	Standard	✓	×	-	2	High	0.482	8	0.339 ± 0.013	-
[80]	Standard	✓	✓	-	2-5	High	0.570	6	0.368 ± 0.015	-
Proposed method	Rotational	✓	✓	60° RAO to 60° LAO, 25° CRA/CAU	3-4	Low	0.099	10	0.428 ± 0.168	5.5 min

span. Our method can work with automatically segmented coronary artery centrelines from 3-5 X-ray images, is robust to possible outliers in the segmentations, and requires minimal amount of interaction during the tree reconstruction.

6.5 Discussion

The experiments in the previous section demonstrated that the proposed method can successfully reconstruct coronary arteries from routinely acquired X-ray rotational angiography images. Our method was capable of reconstructing coronary artery shapes from automatically generated 2D segmentations, which can include inaccuracies/outliers. In particular, some branches may not be visible in all X-ray images due to contrast wash-in/out, or the segmentations may be noisy. Thanks to heavy tails of the t-distributions and the prior information, our method can overcome such segmentation artifacts. In addition to that, our method was shown to be relatively insensitive to residual cardiac motion between gated X-ray images, and can generate an average model, recovering the shape of the arteries at the desired cardiac phase.

In the proposed method, the model complexity is controlled by the number of components in the mixture model (M), and the parameters for the spatial (β) and sparsity (ζ) priors. In our experience, the range of values between 0.05 and 0.20 for β deliver satisfying results. We also observed that β should be kept small ($0.05 \leq$) for tortuous vessels, which agrees with the definition of the spatial regularisation prior. The other two parameters are interrelated, since ζ specifies M, by incorporating sparsity on the mixture weights. The initial value for M depends on the number and length of branches to reconstruct, and the values between 80 and 250 worked well for our dataset. We observed that starting with a moderate number of model points (approximately 150), and adjusting sparsity level yields superior reconstruction results. The range of values for ζ was between 0.025 and 0.050. One should note that the sparsity enforced by Dirichlet distribution in Eq. (6.8) quickly increases, even for the small change of α parameter towards zero. This range of ζ values offers a delicate balance between the sparsity and the level of details in the final reconstruction. Increasing this parameter further resulted in extremely sparse models that cannot capture anatomical details.

The additional value of the prior information was demonstrated experimentally.

In particular, we showed that these priors can become useful when the number of X-ray images is low. In such cases, prior information regularises the reconstruction problem, increasing the accuracy of final segmentations. Both of the priors defined in this chapter are generic, and can be incorporated into the Gaussian mixture model based framework of Chapter 4.

The proposed method provides a convenient framework for integration of prior information in terms of prior distributions defined over mixture model parameters. Therefore, it may be possible to include other information, such as ventricular epicardium surface constraints [33, 86] or coronary artery shape models [200, 201], by defining those as probability distributions. However, inter-patient variability and pathologies must be considered while incorporating such prior information. In this context, our spatial regularisation prior is generic, and can deal with different topologies.

Currently, the proposed method can reconstruct 3D centrelines of the coronary arterial trees. This typically constitutes the initial step in a model-based coronary artery reconstruction workflow. To enable quantitative analysis of the lumen, especially in the stenotic regions, 3D centreline reconstruction should be coupled with a vascular lumen reconstruction. Reconstruction of the lumen could also facilitate the study of hemodynamic parameters by means of computational fluid dynamics simulations, and could consequently facilitate the computation of clinically relevant physiological indices, such as fractional flow reserve [44,46]. The reconstruction of vascular lumen from X-ray projection images is well-studied in the literature, and there are some convenient methods (see Section 2.2.2.5). These methods extract diameter information from multiple X-ray images, and use the diameters to define a cross-sectional shape of the vessel around each of the reconstructed centreline points. These cross-sections are then converted into surface meshes. Incorporation the vascular lumen reconstruction into the current method will be the subject of our future work.

The average runtime of the method on clinical data sets was 5.5 min with our single-core CPU implementation. Therefore, the current implementation of the method only lends itself to offline processing of coronary artery reconstructions. This may be valuable for some clinical scenarios, however the ultimate goal is to have a robust, accurate and real-time coronary artery reconstruction method. Fortunately, the proposed reconstruction method can be accelerated, since the update equations for each t-distribution component can be run in parallel when the spatial regularisation term is ignored. We anticipate that a two step reconstruction can reduce the computational time, where in the first step an initial reconstruction is computed in parallel without spatial regularisation, and then refined with inclusion of the spatial regularisation term in the second step. In addition, we observed that the number of model points (M) has a significant impact on the computational time. This can be leveraged to devise a multi-resolution reconstruction strategy, similar to the one proposed in [167].

6.6 Conclusion

In this chapter, a novel probabilistic model based method is proposed to reconstruct coronary artery centrelines from retrospectively gated X-ray rotational angiography images. The target 3D coronary arteries are represented by a mixture of Student's t-distribution, and the reconstruction is formulated as estimation of mixture model parameters, given 2D coronary artery centreline segmentations from multiple X-ray images. Compared to existing forward-projection based modelling methods, the probabilistic formulation of the proposed method allows us to introduce regularisation terms in the form of Bayesian priors to cope with the ill-posedness. These regularisation terms and the heavy tails of the t-distribution components contribute to the robustness of the method in the presence of noise, errors in the 2D centreline segmentations, and residual cardiac motion between 2D X-ray images. Qualitative and quantitative results on synthetic and clinical data sets show that the proposed method is effective and sufficiently accurate. Incorporation of the vascular lumen reconstruction, and improvements in computation time will be the subjects of our future work.

Chapter 7

Conclusions

7.1 Conclusions

X-ray coronary angiography is still considered as the gold standard for diagnosis of coronary artery disease and guidance during its treatment. This imaging modality is fundamentally limited, since it can only represent complex and dynamic coronary artery trees with 2D X-ray projection images. Three-dimensional reconstructions of coronary arteries can obviate some of the limitations of 2D X-ray coronary angiography, namely artery overlap/foreshortening and lack of depth information. However, X-ray angiography related challenges (such as intensity inhomogeneity, artery overlap/foreshortening, and cardiac/respiratory motion) pose a serious challenge for the reconstruction problem. It was the goal of this thesis to develop robust algorithms to reconstruct 3D/3D+t coronary artery centrelines from X-ray rotational angiography, and assess their performance in realistic settings.

To identify the gaps in the literature, we carried out an exhaustive literature survey on the 3D/3D+t reconstruction of coronary arteries from X-ray angiography, as presented in Chapter 2. According to our review, two main reconstruction efforts can be distinguished, namely model-based and tomographic reconstruction. The main difference between these two different approaches is the final reconstruction output. Model-based reconstruction (modelling) attempt to compute a symbolic representation of coronary arteries, which consists of a 3D centreline and, occasionally, the vascular lumen. Tomographic reconstruction methods produces a volume of attenuation coefficients. The methodological aspects for both types of reconstruction approaches has been discussed in detail in Chapter 2.

Chapter 2 concludes with some important messages by listing a number of possible future directions. First, the time requirement for the reconstruction methods must be drastically reduced to allow for real-time processing. This can be achieved by taking advantage of the state-of-the-art parallel computing techniques. Second, research effort must be invested in developing new dynamic (3D+t) reconstruction algorithms to provide operational guidance. Finally, almost automatic methods must be devised to make 3D reconstruction technology an irreplaceable part of the cath-lab. In this thesis, we mainly focused on the last two directions. Specifically, we proposed i) a novel probabilistic model-based reconstruction framework (Chapter 4 and 6), and ii) a new model based 3D+t coronary arterial tree reconstruction method (Chapter 5).

Model-based reconstruction algorithms offer flexible and relatively simple technical solutions on the reconstruction problem. Most of the model-based reconstruction methods require accurate and clean centreline segmentations from 2D X-ray images as input. However, segmentation of coronary arteries suffers from the angiography related problems, namely inhomogeneous intensities, and artery overlap/foreshortening. As a result, this requirement may hinder the adoption of these methods in the clinical practice. To address this limitation, we presented a novel probabilistic model-based reconstruction framework in Chapter 4 and 6. In particular, we propose to represent 3D coronary artery centrelines by a probabilistic mixture model. To this end, centrelines are assumed to be represented by a set of points, whose spatial locations are assumed to specify means of some probability distribution function. The reconstruction is formulated as estimation of mixture model parameters using Expectation Maximisation algorithm. The main advantage of this probabilistic framework is that it can tolerate noisy and erroneously segmented parts (outliers), and therefore has the potential to reduce manual input.

In Chapter 4, a Gaussian mixture model is chosen as the 3D centreline model. To gain robustness against the outliers, a uniform distribution component is added to the mixture model. Despite its effectiveness in reconstruction and its robustness against random outliers, the method suffers from overfitting in certain scenarios. More precisely, the number of mixture model components play a critical role, making it necessary to find an optimal value for it. The effect of overfitting becomes more evident when there is residual motion in the gated X-ray images. Moreover, an estimation of the outlier level is required to adjust the parameter that controls the weight of the outlier distribution component. Incorrect parameter adjustment can cause a failure of the reconstruction algorithm.

In Chapter 6, a mixture of Student's t-distributions is employed to model 3D coronary artery centrelines. The main motivation behind this selection is the heavy tails of t-distributions. Specifically, a Student's t-distribution has heavier tails compared to a Gaussian distribution. Its robustness can be controlled in a parametric fashion, eliminating the necessity of identifying the outliers and tackling with them separately. By using t-distribution, we can avoid setting the parameter controlling the weight of outlier distribution, and indirectly estimate it from the data. Additionally, we incorporated prior information into the reconstruction, since the overfitting is known to be avoided by introducing prior information. More importantly, the incorporation of prior information into model-based coronary artery reconstruction has been overlooked in the relevant literature, partly because of unsuitable models. Our probabilistic framework offers a convenient framework for addition of prior information in terms of probability distributions. In the proposed method, the prior information enables us to spatially regularise the reconstruction, and remove unnecessary mixture model components. Our experiments demonstrated that the cumulative effect of t-distributions and the prior information reduces the number of required X-ray images for reconstruction, and the manual interaction required to segment those images.

In Chapter 5, a new method to reconstruct 3D+t centreline points from rotational angiography is devised. The main assumption is that the coronary arteries are attached to the ventricular epicardium and moves together with the epicardial surface. Therefore, a spatiotemporal model of the ventricular epicardium could potentially describe the 3D+t structure of the coronary arteries if the locations of the coronary arteries on the model can be estimated. To this end, we employed a spatiotemporal statistical shape model of the left ventricular epicardium. Given 2D+t centreline points (i.e. points tracked over the sequence of X-ray images), 3D+t reconstruction is formulated as a 2D+t/3D+t Gaussian mixture model based registration between the tracked points and the projections of the points describing the bilinear model. Using a modified EM algorithm, we succeeded in estimating the arterial locations on the bilinear model, the rigid transformation between the artery and model coordinates, and the bilinear model parameters. To ease the estimation of arterial locations, we have taken advantage of prior knowledge on the anatomy of the heart. Moreover, we learned the distributions of the bilinear model parameters from a training data, and used it as a prior information to regularise parameter estimation. Our experimentation showed that the method can cope with missing and noisy tracking information.

7.2 Outlook and Future Work

There are several potential ways to improve the methods proposed in this thesis, and several future directions to investigate in the topic of coronary artery reconstruction from X-ray angiography.

Incorporation of other prior information: For model-based reconstruction, we have showed various ways to take advantage of our prior knowledge about the structure of the coronary arteries. Incorporation of prior information can help us to reduce the number of X-ray images required, by imposing more constraints on the ill-posed reconstruction problem. Following that, we can optimise our imaging protocols such that we effectively reduce the X-ray exposure of the patient and the operator. There are two promising directions to achieve this goal.

First one is due to the surface constraints of the coronary arteries. Utilisation of this type of prior information has already been investigated in the context of 2D/3D registration [33] and 3D+t reconstruction (Chapter 5), nevertheless requires more attention. There are two main challenges with this approach. First, the correspondence establishment between the surface and the arteries is not well-defined, since only a small subset of surface points correspond to the arteries. This necessitates some stronger prior information about the distribution of arterial locations on the surface model, which can be obtained from a large training data [201]. Second, the coronary arteries might not be attached to the epicardial surface, especially around the ostium region as indicated by the experiments in Chapter 5.

Second one is the utilisation of shape models of the coronary arteries. Although it is a difficult task to generate a statistical shape model of tree-shaped structures due to diverse topological variations amongst the data, there are recent intriguing attempts to approach this problem [200, 201].

Reconstruction using other features: As an alternative to the 2D coronary artery segmentations, other features that might be easier to extract could be utilised, such as 2D vesselness responses [188, 189]. Specifically, the probabilistic reconstruction framework presented in this thesis can be adapted to work with vesselness responses. Instead of treating centrelines as the data points drawn from the mixture model, one can directly consider the pixels of the vesselness responses as weighted data points, and compute reconstructions using a weighted data mixture model [202]. This way, dependency to the centreline segmentations could be eliminated, making the method fully automatic. However, due to the noise in the vesselness responses, we expect that such a method may require more X-ray images to obtain satisfactory reconstructions.

3D+t reconstruction: Our probabilistic model-based reconstruction framework can be extended in two different ways to compute 3D+t reconstructions. First, the existing literature on non-rigid point set registration [158, 159, 162] can be exploited to devise new 3D+t reconstruction strategies. We anticipate that the motion coherence theory [159,160] can be adapted to estimate the motion between different cardiac phases in a 2D/3D setting. Second, there is a recent interest in the non-rigid structure from motion, which is defined as the recovery of time-varying shape and motion of a non-rigid structure. Although most of these methods deal with orthographic projection, some recent methods discuss the use of perspective projections [203], which is similar to our reconstruction problem. As an alternative to existing 3D+t reconstruction algorithms, one could potentially describe the trajectory of a coronary artery centreline point by some linear basis functions [203, 204] to regularise motion estimation.

Development of clinical software tools: Although there is a large amount of research evidence supporting the additional value of 3D reconstructions in the clinical practice, 3D reconstruction technology is still not commonly used. This is partly because the time and user interaction requirements of some of the reconstruction algorithms do not match the clinical requirements. On the other hand, the lack of clinical software tools that can be operated by clinicians contributes to the slow clinical translation. New research should be devoted to improve virtual FFR estimation tools [43] and develop virtual stenting tools [154] to see the impact of reconstruction technology in the treatment of CAD. In this way, a feedback mechanism between clinical and engineering research can be maintained to develop the future artery visualisation technologies.

Bibliography

[1] M. Nichols, N. Townsend, P. Scarborough, and M. Rayner, "Cardiovascular disease in Europe: epidemiological update," *Eur. Heart J.*, vol. 34, no. 39, pp. 3028–34, 2013.

[2] A. S. Go, D. Mozaffarian, V. L. Roger, E. J. Benjamin, J. D. Berry, M. J. Blaha, S. Dai, E. S. Ford, C. S. Fox, S. Franco, H. J. Fullerton, C. Gillespie, S. M. Hailpern, J. a. Heit, V. J. Howard, M. D. Huffman, S. E. Judd, B. M. Kissela, S. J. Kittner, D. T. Lackland, J. H. Lichtman, L. D. Lisabeth, R. H. Mackey, D. J. Magid, G. M. Marcus, A. Marelli, D. B. Matchar, D. K. McGuire, E. R. Mohler, C. S. Moy, M. E. Mussolino, R. W. Neumar, G. Nichol, D. K. Pandey, N. P. Paynter, M. J. Reeves, P. D. Sorlie, J. Stein, A. Towfighi, T. N. Turan, S. S. Virani, N. D. Wong, D. Woo, and M. B. Turner, "Heart disease and stroke Statistics - 2014 update: A report from the American Heart Association," *Circulation*, vol. 129, no. 3, pp. e28–e292, 2014.

[3] M. Kachelriess, S. Ulzheimer, and W. A. Kalender, "ECG-correlated imaging of the heart with subsecond multislice spiral CT," *IEEE Trans. Med. Imaging*, vol. 19, no. 9, pp. 888–901, 2000.

[4] G. Shechter, G. Naveh, A. Altman, R. M. Proksa, and M. Grass, "Cardiac image reconstruction on a 16-slice CT scanner using a retrospectively ECG-gated multicycle 3D back-projection algorithm," in *Proc. SPIE*, vol. 5032, 2003, pp. 1820–1828.

[5] D. B. Mark, D. S. Berman, M. J. Budoff, J. J. Carr, T. C. Gerber, H. S. Hecht, M. A. Hlatky, J. M. Hodgson, M. S. Lauer, J. M. Miller, R. L. Morin, D. Mukherjee, M. Poon, G. D. Rubin, and R. S. Schwartz,

"ACCF/ACR/AHA/NASCI/SAIP/SCAI/SCCT 2010 expert consensus document on coronary computed tomographic angiography: a report of the American College of Cardiology Foundation Task Force on Expert Consensus Documents," *J. Am. Coll. Cardiol.*, vol. 55, no. 23, pp. 2663–99, 2010.

[6] M. Stuber and R. G. Weiss, "Coronary magnetic resonance angiography," *J. Magn. Reson. Imaging*, vol. 26, no. 2, pp. 219–234, 2007.

[7] F. M. Sones and E. K. Shirey, "Cine coronary arteriography." *Mod. Concepts Cardiovasc. Dis.*, vol. 31, pp. 735–8, 1962.

[8] A. J. P. Klein and J. A. Garcia, "Rotational coronary angiography," *Cardiol. Clin.*, vol. 27, no. 3, pp. 395–405, 2009.

[9] H. Hetterich, T. Redel, G. Lauritsch, C. Rohkohl, and J. Rieber, "New X-ray imaging modalities and their integration with intravascular imaging and interventions," *Int. J. Cardiovasc. Imaging*, vol. 26, no. 7, pp. 797–808, 2010.

[10] P. J. Scanlon, D. P. Faxon, A.-M. Audet, B. Carabello, G. J. Dehmer, K. A. Eagle, R. D. Legako, D. F. Leon, J. A. Murray, S. E. Nissen, C. J. Pepine, R. M. Watson, J. L. Ritchie, R. J. Gibbons, M. D. Cheitlin, T. J. Gardner, A. Garson, R. O. Russell, T. J. Ryan, and S. C. Smith, "ACC/AHA guidelines for coronary angiography: Executive summary and recommendations : A report of the American College of Cardiology/American Heart Association Task Force on Practice Guidelines (Committee on Coronary Angiography) Developed in collaboration," *Circulation*, vol. 99, no. 17, pp. 2345–2357, 1999.

[11] N. E. Green, S.-Y. J. Chen, J. C. Messenger, B. M. Groves, and J. D. Carroll, "Three-dimensional vascular angiography," *Curr. Probl. Cardiol.*, vol. 29, no. 3, pp. 104–42, 2004.

[12] J. C. Messenger and I. P. Casserly, "Advances in contrast media and contrast injectors," *Cardiol. Clin.*, vol. 27, no. 3, pp. 407–15, 2009.

[13] P. A. McCullough, "Contrast-induced acute kidney injury," *J. Am. Coll. Cardiol.*, vol. 51, no. 15, pp. 1419–28, 2008.

[14] G. Tommasini, A. Camerini, A. Gatti, G. Derchi, A. Bruzzone, and C. Vecchio, “Panoramic coronary angiography,” *J. Am. Coll. Cardiol.*, vol. 31, no. 4, pp. 871–877, 1998.

[15] A. J. Klein, J. A. Garcia, P. A. Hudson, M. S. Kim, J. C. Messenger, I. P. Casserly, O. Wink, B. Hattler, T. T. Tsai, S. Y. J. Chen, A. Hansgen, and J. D. Carroll, “Safety and efficacy of dual-axis rotational coronary angiography vs. standard coronary angiography,” *Catheter. Cardiovasc. Interv.*, vol. 77, no. 6, pp. 820–827, 2011.

[16] L. Unzué Vallejo, J. L. Delcán Domínguez, A. Alegría Barrero, J. Medina Peralta, F. J. Rodríguez Rodrigo, and J. L. Rodríguez-López, “Coronary lesions quantification with dual-axis rotational coronary angiography,” *Cardiovasc. Revascularization Med.*, vol. 14, no. 1, pp. 37–40, 2013.

[17] J. Garcia, B. Movassaghi, I. Casserly, A. Klein, S.-Y. James Chen, J. Messenger, A. Hansgen, O. Wink, B. Groves, and J. Carroll, “Determination of optimal viewing regions for X-ray coronary angiography based on a quantitative analysis of 3D reconstructed models,” *Int. J. Cardiovasc. Imaging*, vol. 25, no. 5, pp. 455–462, 2009.

[18] S. J. Chen and D. Schäfer, “Three-dimensional coronary visualization, Part 1: modeling,” *Cardiol. Clin.*, vol. 27, no. 3, pp. 433–52, 2009.

[19] J. D. Carroll, E. P. Carroll, and S. J. Chen, “Coronary angiography: the need for improvement and the barriers to adoption of new technology,” *Cardiol. Clin.*, vol. 27, no. 3, pp. 373–83, 2009.

[20] R. Cardenes, A. Novikov, J. Gunn, R. Hose, and A. F. Frangi, “3D reconstruction of coronary arteries from rotational X-ray angiography,” in *Proc. IEEE Int. Symp. Biomed. Imaging*, 2012, pp. 618–621.

[21] R. R. Gollapudi, R. Valencia, S. S. Lee, G. B. Wong, P. S. Teirstein, and M. J. Price, “Utility of three-dimensional reconstruction of coronary angiography to guide percutaneous coronary intervention,” *Catheter. Cardiovasc. Interv.*, vol. 69, no. 4, pp. 479–482, 2007.

[22] M. H. Eng, P. A. Hudson, A. J. Klein, S. J. Chen, M. S. Kim, B. M. Groves, J. C. Messenger, O. Wink, J. D. Carroll, and J. A. Garcia, “Impact of

three dimensional in-room imaging (3DCA) in the facilitation of percutaneous coronary interventions," *J. Cardiol. Vasc. Med.*, vol. 1, no. 1, pp. 1–5, 2013.

[23] L. Mauri, A. J. O'Malley, J. J. Popma, J. W. Moses, M. B. Leon, D. R. Holmes, P. S. Teirstein, D. E. Cutlip, D. Donahoe, and R. E. Kuntz, "Comparison of thrombosis and restenosis risk from stent length of sirolimus-eluting stents versus bare metal stents," *Am. J. Cardiol.*, vol. 95, no. 10, pp. 1140–5, 2005.

[24] R. Moreno, C. Fernández, R. Hernández, F. Alfonso, D. J. Angiolillo, M. Sabaté, J. Escaned, C. Bañuelos, A. Fernández-Ortiz, and C. Macaya, "Drug-eluting stent thrombosis: results from a pooled analysis including 10 randomized studies," *J. Am. Coll. Cardiol.*, vol. 45, no. 6, pp. 954–9, 2005.

[25] I. Pantos, E. P. Efstathopoulos, and D. G. Katritsis, "Two and three-dimensional quantitative coronary angiography," *Cardiol. Clin.*, vol. 27, no. 3, pp. 491–502, 2009.

[26] D. Dvir, A. Assali, and R. Kornowski, "Percutaneous coronary intervention for chronic total occlusion: Novel 3-dimensional imaging and quantitative analysis," *Catheter. Cardiovasc. Interv.*, vol. 71, no. 6, pp. 784–789, 2008.

[27] J. A. Garcia, J. Chen, A. Hansgen, O. Wink, B. Movassaghi, and J. C. Messenger, "Rotational angiography (RA) and three-dimensional imaging (3-DRA): an available clinical tool," *Int. J. Cardiovasc. Imaging*, vol. 23, no. 1, pp. 9–13, 2007.

[28] P. Agostoni, G. Biondi-Zoccai, G. Van Langenhove, K. Cornelis, P. Vermeersch, C. Convens, C. Vassanelli, P. Van Den Heuvel, F. Van Den Branden, and S. Verheye, "Comparison of assessment of native coronary arteries by standard versus three-dimensional coronary angiography," *Am. J. Cardiol.*, vol. 102, no. 3, pp. 272–9, 2008.

[29] J. Lee, S. Chang, S. Kim, Y. Lee, J. Ryu, J. Choi, K. Kim, and J. Park, "Assessment of three dimensional quantitative coronary analysis by using rotational angiography for measurement of vessel length and diameter," *Int. J. Cardiovasc. Imaging*, vol. 28, no. 7, pp. 1627–1634, 2012.

[30] D. Meerkin, H. Marom, O. Cohen-Biton, and S. Einav, "Three-dimensional vessel analyses provide more accurate length estimations than the gold standard QCA," *J. Interv. Cardiol.*, vol. 23, no. 2, pp. 152–159, 2010.

[31] A. M. Neubauer, J. A. Garcia, J. C. Messenger, E. Hansis, M. S. Kim, A. J. Klein, G. A. Schoonenberg, M. Grass, and J. D. Carroll, "Clinical feasibility of a fully automated 3D reconstruction of rotational coronary X-Ray angiograms," *Circ. Cardiovasc. Interv.*, vol. 3, no. 1, pp. 71–79, 2010.

[32] D. Rivest-Hénault, H. Sundar, and M. Cheriet, "Nonrigid 2D/3D registration of coronary artery models with live fluoroscopy for guidance of cardiac interventions," *IEEE Trans. Med. Imaging*, vol. 31, no. 8, pp. 1557–72, 2012.

[33] N. Baka, C. T. Metz, C. Schultz, L. Neefjes, R. J. van Geuns, B. P. F. Lelieveldt, W. J. Niessen, T. van Walsum, and M. de Bruijne, "Statistical coronary motion models for 2D+t/3D registration of X-ray coronary angiography and CTA," *Med. Image Anal.*, vol. 17, no. 6, pp. 698–709, 2013.

[34] G. Dibildox, N. Baka, M. Punt, J.-P. Aben, C. Schultz, W. Niessen, and T. van Walsum, "3D/3D registration of coronary CTA and biplane XA reconstructions for improved image guidance," *Med. Phys.*, vol. 41, no. 9, p. 091909, 2014.

[35] N. Bruining, S. de Winter, and P. W. Serruys, "Intravascular ultrasound registration/integration with coronary angiography," *Cardiol. Clin.*, vol. 27, no. 3, pp. 531–540, 2009.

[36] S. Tu, L. Xu, J. Ligthart, B. Xu, K. Witberg, Z. Sun, G. Koning, J. Reiber, and E. Regar, "In vivo comparison of arterial lumen dimensions assessed by co-registered three-dimensional (3D) quantitative coronary angiography, intravascular ultrasound and optical coherence tomography," *Int. J. Cardiovasc. Imaging*, vol. 28, no. 6, pp. 1315–1327, 2012.

[37] C. A. Taylor and D. A. Steinman, "Image-based modeling of blood flow and vessel wall dynamics: Applications, methods and future Directions," *Ann. Biomed. Eng.*, vol. 38, no. 3, pp. 1188–1203, 2010.

[38] J.-M. Zhang, L. Zhong, B. Su, M. Wan, J. S. Yap, J. P. L. Tham, L. P. Chua, D. N. Ghista, and R. S. Tan, "Perspective on CFD studies of coronary

artery disease lesions and hemodynamics: A review," *Int. J. Numer. Method. Biomed. Eng.*, vol. 30, no. 6, pp. 659–680, 2014.

[39] M. J. Kern, A. Lerman, J.-W. Bech, B. De Bruyne, E. Eeckhout, W. F. Fearon, S. T. Higano, M. J. Lim, M. Meuwissen, J. J. Piek, N. H. J. Pijls, M. Siebes, and J. A. E. Spaan, "Physiological assessment of coronary artery disease in the cardiac catheterization laboratory: a scientific statement from the American Heart Association Committee on Diagnostic and Interventional Cardiac Catheterization, Council on Clinical Cardiology," *Circulation*, vol. 114, no. 12, pp. 1321–41, 2006.

[40] N. H. J. Pijls, P. van Schaardenburgh, G. Manoharan, E. Boersma, J.-W. Bech, M. van't Veer, F. Bär, J. Hoorntje, J. Koolen, W. Wijns, and B. de Bruyne, "Percutaneous coronary intervention of functionally nonsignificant stenosis: 5-year follow-up of the DEFER Study," *J. Am. Coll. Cardiol.*, vol. 49, no. 21, pp. 2105–11, 2007.

[41] P. A. L. Tonino, B. De Bruyne, N. H. J. Pijls, U. Siebert, F. Ikeno, M. van 't Veer, V. Klauss, G. Manoharan, T. Engstrø m, K. G. Oldroyd, P. N. Ver Lee, P. A. MacCarthy, and W. F. Fearon, "Fractional flow reserve versus angiography for guiding percutaneous coronary intervention," *N. Engl. J. Med.*, vol. 360, no. 3, pp. 213–224, 2009.

[42] N. P. Johnson, R. L. Kirkeeide, and K. L. Gould, "Coronary anatomy to predict physiology: fundamental limits," *Circ. Cardiovasc. Imaging*, vol. 6, no. 5, pp. 817–32, 2013.

[43] P. D. Morris, F. N. van de Vosse, P. V. Lawford, D. R. Hose, and J. P. Gunn, ""Virtual" (computed) fractional flow reserve: Current challenges and limitations," *JACC. Cardiovasc. Interv.*, vol. 8, no. 8, pp. 1009–17, 2015.

[44] P. D. Morris, D. Ryan, A. C. Morton, R. Lycett, P. V. Lawford, D. R. Hose, and J. P. Gunn, "Virtual fractional flow reserve from coronary angiography: modeling the significance of coronary lesions: results from the VIRTU-1 (VIRTUal Fractional Flow Reserve From Coronary Angiography) study," *JACC. Cardiovasc. Interv.*, vol. 6, no. 2, pp. 149–57, 2013.

[45] M. I. Papafaklis, T. Muramatsu, Y. Ishibashi, L. S. Lakkas, S. Nakatani, C. V. Bourantas, J. Ligthart, Y. Onuma, M. Echavarria-Pinto, G. Tsirka, A. Kotsia, D. N. Nikas, O. Mogabgab, R.-J. van Geuns, K. K. Naka, D. I. Fotiadis, E. S. Brilakis, H. M. Garcia-Garcia, J. Escaned, F. Zijlstra, L. K. Michalis, and P. W. Serruys, "Fast virtual functional assessment of intermediate coronary lesions using routine angiographic data and blood flow simulation in humans: comparison with pressure wire - fractional flow reserve," *EuroIntervention*, vol. 10, no. 5, pp. 574–83, 2014.

[46] S. Tu, E. Barbato, Z. Köszegi, J. Yang, Z. Sun, N. R. Holm, B. Tar, Y. Li, D. Rusinaru, W. Wijns, and J. H. C. Reiber, "Fractional flow reserve calculation from 3-dimensional quantitative coronary angiography and TIMI frame count: a fast computer model to quantify the functional significance of moderately obstructed coronary arteries," *JACC. Cardiovasc. Interv.*, vol. 7, no. 7, pp. 768–77, 2014.

[47] P. T. Campbell and E. Mahmud, "Prospective, online, interactive survey comparing visual lesion estimation to quantitative coronary angiography," *J. Am. Coll. Cardiol.*, vol. 64, no. 11, p. B25, 2014.

[48] J. Ligthart, K. Witberg, A. Karanasos, S. Tu, and J. Reiber, "Can co-registration influence the accuracy of stent placement? A retrospective observational study," in *EUROPCR*, W. Wijns, J. Fajadet, and P. W. Serruys, Eds., 2014.

[49] L. Calmac, R. Niculescu, E. Badila, E. Weiss, D. Zamfir, L. Itu, L. Lazar, M. Carp, A. Itu, C. Suciu, T. Passerini, P. Sharma, B. Georgescu, and D. Comaniciu, "Image-Based computation of instantaneous wave-free ratio from routine coronary angiography - Initial validation by invasively measured coronary pressures," *J. Am. Coll. Cardiol.*, vol. 66, no. 15, pp. B17–B18, 2015.

[50] A. J. Lansky and C. Pietras, "Fractional flow reserve from 3-dimensional quantitative coronary angiography: fresh light through an old window," *JACC. Cardiovasc. Interv.*, vol. 7, no. 7, pp. 778–80, 2014.

[51] G. Schoonenberg, A. Neubauer, and M. Grass, "Three-dimensional coronary visualization, Part 2: 3D reconstruction," *Cardiol. Clin.*, vol. 27, no. 3, pp. 453–65, 2009.

[52] R. Hartley and A. Zisserman, *Multiple view geometry in computer vision*, 2nd ed. Cambridge University Press, 2004.

[53] G. Shechter, F. Devernay, E. Coste-Manière, A. Quyyumi, and E. R. McVeigh, "Three-dimensional motion tracking of coronary arteries in biplane cineangiograms," *IEEE Trans. Med. Imaging*, vol. 22, no. 4, pp. 493–503, 2003.

[54] C. Cañero, P. Radeva, R. Toledo, J. Villanueva, and J. Mauri, "3D curve reconstruction by biplane snakes," in *Proc. IEEE Int. Conf. Pattern Recognit.*, vol. 4, 2000, pp. 563–566.

[55] N. Strobel, O. Meissner, J. Boese, T. Brunner, B. Heigl, M. Hoheisel, G. Lauritsch, M. Nagel, M. Pfister, E.-P. Rührnschopf, B. Scholz, B. Schreiber, M. Spahn, M. Zellerhoff, and K. Klingenbeck-Regn, "3D imaging with flat-detector C-Arm systems," in *Multislice CT*, ser. Medical Radiology, 2009, pp. 33–51.

[56] K. Wiesent, K. Barth, N. Navab, P. Durlak, T. Brunner, O. Schuetz, and W. Seissler, "Enhanced 3-D-reconstruction algorithm for C-arm systems suitable for interventional procedures," *IEEE Trans. Med. Imaging*, vol. 19, no. 5, pp. 391–403, 2000.

[57] A. Rougée, C. Picard, D. Saint-Félix, Y. Trousset, T. Moll, and M. Amiel, "Three-dimensional coronary arteriography," *Int. J. Card. Imaging*, vol. 10, no. 1, pp. 67–70, 1994.

[58] R. Koppe, E. Klotz, J. D. Beek, and H. Aerts, "3D vessel reconstruction based on rotational angiography," in *Proc. Comput. Assist. Radiol. Surg.*, 1995, pp. 17–22.

[59] R. Fahrig, A. J. Fox, S. Lownie, and D. W. Holdsworth, "Use of a C-arm system to generate true three-dimensional computed rotational angiograms: preliminary in vitro and in vivo results," *Am. J. Neuroradiol.*, vol. 18, no. 8, pp. 1507–14, 1997.

[60] G. Shechter, J. R. Resar, and E. R. McVeigh, "Displacement and velocity of the coronary arteries: cardiac and respiratory motion," *IEEE Trans. Med. Imaging*, vol. 25, no. 3, pp. 369–375, 2006.

[61] L. Husmann, S. Leschka, L. Desbiolles, T. Schepis, O. Gaemperli, B. Seifert, P. Cattin, T. Frauenfelder, T. G. Flohr, B. Marincek, P. A. Kaufmann, and H. Alkadhi, "Coronary artery motion and cardiac phases: dependency on heart rate – implications for CT image reconstruction," *Radiology*, vol. 245, no. 2, pp. 567–76, 2007.

[62] C. Rohkohl, M. Prümmer, R. Fahrig, G. Lauritsch, and J. Hornegger, "Cardiac C-arm CT: image-based gating," in *Proc. SPIE*, vol. 6913, 2008, pp. 69 131G–69 131G–12.

[63] C. Rohkohl, G. Lauritsch, M. Prümmer, and J. Hornegger, "Interventional 4-D motion estimation and reconstruction of cardiac vasculature without motion periodicity assumption," in *Proc. Med. Image Comput. Comput. Assist. Interv.*, ser. LNCS, vol. 5761, 2009, pp. 132–139.

[64] C. Blondel, G. Malandain, R. Vaillant, and N. Ayache, "Reconstruction of coronary arteries from a single rotational X-ray projection sequence," *IEEE Trans. Med. Imaging*, vol. 25, no. 5, pp. 653–663, 2006.

[65] G. C. Lehmann, D. W. Holdsworth, and M. Drangova, "Angle-independent measure of motion for image-based gating in 3D coronary angiography," *Med. Phys.*, vol. 33, no. 5, pp. 1311–20, 2006.

[66] D. Schäfer, J. Borgert, V. Rasche, and M. Grass, "Motion-compensated and gated cone beam filtered back-projection for 3-D rotational X-ray angiography," *IEEE Trans. Med. Imaging*, vol. 25, no. 7, pp. 898–906, 2006.

[67] V. Rasche, B. Movassaghi, and M. Grass, "Automatic gating window selection for gated three-dimensional coronary X-ray angiography," in *Proc. Comput. Assist. Radiol. Surg.*, vol. 1268, 2004, pp. 1050–1054.

[68] V. Rasche, B. Movassaghi, M. Grass, D. Schäfer, and A. Buecker, "Automatic selection of the optimal cardiac phase for gated three-dimensional coronary x-ray angiography," *Acad. Radiol.*, vol. 13, no. 5, pp. 630–40, 2006.

[69] E. Hansis, D. Schäfer, O. Dössel, and M. Grass, "Automatic optimum phase point selection based on centerline consistency for 3D rotational coronary angiography," *Int. J. Comput. Assist. Radiol. Surg.*, vol. 3, no. 3-4, pp. 355–361, 2008.

[70] V. Rasche, B. Movassaghi, M. Grass, D. Schäfer, H. P. Kühl, R. W. Günther, and A. Bücker, "Three-dimensional X-ray coronary angiography in the porcine model: A feasibility study," *Acad. Radiol.*, vol. 13, no. 5, pp. 644–51, 2006.

[71] C. Rohkohl, G. Lauritsch, A. Nottling, M. Prummer, and J. Hornegger, "C-arm CT: Reconstruction of dynamic high contrast objects applied to the coronary sinus," in *IEEE Nucl. Sci. Symp. Conf. Rec.*, 2008, pp. 5113–5120.

[72] C. Schwemmer, C. Rohkohl, G. Lauritsch, K. Müller, and J. Hornegger, "Residual motion compensation in ECG-gated interventional cardiac vasculature reconstruction," *Phys. Med. Biol.*, vol. 58, no. 11, p. 3717, 2013.

[73] M. Unberath, K. Mentl, O. Taubmann, S. Achenbach, R. Fahrig, J. Hornegger, and A. Maier, "Torsional heart motion in cone-beam computed tomography reconstruction," in *Int. Meet. Fully Three-Dimensional Image Reconstr. Radiol. Nucl. Med.*, M. King, S. Glick, and K. Mueller, Eds., 2015, pp. 651–654.

[74] M. Kass, A. Witkin, and D. Terzopoulos, "Snakes: Active contour models," *Int. J. Comput. Vis.*, vol. 1, no. 4, pp. 321–331, 1988.

[75] C. Xu and J. L. Prince, "Snakes, shapes, and gradient vector flow," *IEEE Trans. Image Process.*, vol. 7, no. 3, pp. 359–69, 1998.

[76] ——, "Generalized gradient vector flow external forces for active contours," *Signal Processing*, vol. 71, no. 2, pp. 131–139, 1998.

[77] L. Cohen and I. Cohen, "Finite-element methods for active contour models and balloons for 2-D and 3-D images," *IEEE Trans. Pattern Anal. Mach. Intell.*, vol. 15, no. 11, pp. 1131–1147, 1993.

[78] C. Cañero, F. Vilariño, J. Mauri, and P. Radeva, "Predictive (un)distortion model and 3-D reconstruction by biplane snakes," *IEEE Trans. Med. Imaging*, vol. 21, no. 9, pp. 1188–201, 2002.

[79] W. Cong, J. Yang, Y. Liu, and Y. Wang, "Energy back-projective composition for 3-D coronary artery reconstruction," *Proc. IEEE Eng. Med. Biol. Soc.*, vol. 2013, pp. 5151–4, 2013.

[80] W. Cong, J. Yang, D. Ai, Y. Chen, Y. Liu, and Y. Wang, "Quantitative analysis of deformable model-based 3-D reconstruction of coronary artery from multiple angiograms," *IEEE Trans. Biomed. Eng.*, vol. 62, no. 8, pp. 2079–90, 2015.

[81] J. Yang, W. Cong, Y. Chen, J. Fan, Y. Liu, and Y. Wang, "External force back-projective composition and globally deformable optimization for 3-D coronary artery reconstruction," *Phys. Med. Biol.*, vol. 59, no. 4, pp. 975–1003, 2014.

[82] Z. Hui and M. Friedman, "Tracking 3-D coronary artery motion with biplane angiography," in *Proc. IEEE Int. Symp. Biomed. Imaging*, 2002, pp. 605–608.

[83] S. Zheng, T. Meiying, and S. Jian, "Sequential reconstruction of vessel skeletons from X-ray coronary angiographic sequences," *Comput. Med. Imaging Graph.*, vol. 34, no. 5, pp. 333–45, 2010.

[84] L. Sarry and J. Y. Boire, "Three-dimensional tracking of coronary arteries from biplane angiographic sequences using parametrically deformable models," *IEEE Trans. Med. Imaging*, vol. 20, no. 12, pp. 1341–51, 2001.

[85] A. Keil, J. Vogel, G. Lauritsch, and N. Navab, "Dynamic cone beam reconstruction using a new level set formulation," in *Proc. Med. Image Comput. Comput. Assist. Interv.*, ser. LNCS, vol. 5762, 2009, pp. 389–397.

[86] S. Çimen, C. Hoogendoorn, P. Morris, J. Gunn, and A. Frangi, "Reconstruction of coronary trees from 3DRA using a 3D+t statistical cardiac prior," in *Proc. Med. Image Comput. Comput. Assist. Interv.*, ser. LNCS, P. Golland, N. Hata, C. Barillot, J. Hornegger, and R. Howe, Eds., vol. 8674, 2014, pp. 619–626.

[87] K. Hoffmann, A. Sen, L. Lan, K.-G. Chua, J. Esthappan, and M. Mazzucco, "A system for determination of 3D vessel tree centerlines from biplane images," *Int. J. Card. Imaging*, vol. 16, no. 5, pp. 315–330, 2000.

[88] S. J. Chen and J. D. Carroll, "3-D reconstruction of coronary arterial tree to optimize angiographic visualization," *IEEE Trans. Med. Imaging*, vol. 19, no. 4, pp. 318–336, 2000.

[89] S. Y. J. Chen and J. D. Carroll, "Kinematic and deformation analysis of 4-D coronary arterial trees reconstructed from cine angiograms," *IEEE Trans. Med. Imaging*, vol. 22, no. 6, pp. 710–721, 2003.

[90] F. Mourgues, F. Devernay, G. Malandain, and E. Coste-Manière, "3D+t modeling of coronary artery tree from standard non simultaneous angiograms," in *Proc. Med. Image Comput. Comput. Assist. Interv.*, ser. LNCS, vol. 2208, 2001, pp. 1320–1322.

[91] P. Fallavollita and F. Cheriet, "Optimal 3D reconstruction of coronary arteries for 3D clinical assessment," *Comput. Med. Imaging Graph.*, vol. 32, no. 6, pp. 476–487, 2008.

[92] J. Yang, Y. Wang, Y. Liu, S. Tang, and W. Chen, "Novel approach for 3-d reconstruction of coronary arteries from two uncalibrated angiographic images," *IEEE Trans. Image Process.*, vol. 18, no. 7, pp. 1563–72, 2009.

[93] B. Movassaghi, V. Rasche, M. Grass, M. A. Viergever, and W. J. Niessen, "A quantitative analysis of 3-D coronary modeling from two or more projection images," *IEEE Trans. Med. Imaging*, vol. 23, no. 12, pp. 1517–1531, 2004.

[94] A. Andriotis, A. Zifan, M. Gavaises, P. Liatsis, I. Pantos, A. Theodorakakos, E. P. Efstathopoulos, and D. Katritsis, "A new method of three-dimensional coronary artery reconstruction from X-ray angiography: Validation against a virtual phantom and multislice computed tomography," *Catheter. Cardiovasc. Interv.*, vol. 71, no. 1, pp. 28–43, 2008.

[95] H. Sakoe and S. Chiba, "Dynamic programming algorithm optimization for spoken word recognition," *IEEE Trans. Acoust.*, vol. 26, no. 1, pp. 43–49, 1978.

[96] R. Liao, D. Luc, Y. Sun, and K. Kirchberg, "3-D reconstruction of the coronary artery tree from multiple views of a rotational X-ray angiography," *Int. J. Cardiovasc. Imaging*, vol. 26, no. 7, pp. 733–749, 2010.

[97] X. Liu, F. Hou, A. Hao, and H. Qin, "A parallelized 4D reconstruction algorithm for vascular structures and motions based on energy optimization," *Vis. Comput.*, vol. 31, no. 11, pp. 1431–46, 2014.

[98] R. Szeliski, R. Zabih, D. Scharstein, O. Veksler, V. Kolmogorov, A. Agarwala, M. Tappen, and C. Rother, "A comparative study of energy minimization methods for Markov random fields with smoothness-based priors," *IEEE Trans. Pattern Anal. Mach. Intell.*, vol. 30, no. 6, pp. 1068–80, 2008.

[99] A. Law and F. Chan, "3D reconstruction of coronary artery using biplane angiography," in *Proc. IEEE Eng. Med. Biol. Soc.*, vol. 1, 2003, pp. 533–536.

[100] U. Jandt, D. Schäfer, M. Grass, and V. Rasche, "Automatic generation of 3D coronary artery centerlines using rotational X-ray angiography," *Med. Image Anal.*, vol. 13, no. 6, pp. 846–58, 2009.

[101] J. Li and L. D. Cohen, "Reconstruction of 3D tubular structures from cone-beam projections," in *Proc. IEEE Int. Symp. Biomed. Imaging*, 2011, pp. 1162–1166.

[102] U. Jandt, D. Schäfer, M. Grass, and V. Rasche, "Automatic generation of time resolved motion vector fields of coronary arteries and 4D surface extraction using rotational x-ray angiography," *Phys. Med. Biol.*, vol. 54, no. 1, pp. 45–64, 2009.

[103] S. Bouattour, R. Arndt, and D. Paulus, "4D reconstruction of coronary arteries from monoplane angiograms," in *Proc. Comput. Anal. Images Patterns*, ser. LNCS, vol. 3691, 2005, pp. 724–731.

[104] Y. Tsin, K. Kirchberg, G. Lauritsch, and C. Xu, "A deformation tracking approach to 4D coronary artery tree reconstruction," in *Proc. Med. Image Comput. Comput. Assist. Interv.*, ser. LNCS, vol. 5762, 2009, pp. 68–75.

[105] A. Bousse Ast, J. Zhou, G. Yang, J.-J. Bellanger, and C. Toumoulin, "Motion compensated tomography reconstruction of coronary arteries in rotational angiography," *IEEE Trans. Biomed. Eng.*, vol. 56, no. 4, pp. 1254–1257, 2009.

[106] J. H. C. Reiber, S. Tu, J. C. Tuinenburg, G. Koning, J. P. Janssen, and J. Dijkstra, “QCA, IVUS and OCT in interventional cardiology in 2011,” *Cardiovasc. Diagn. Ther.*, vol. 1, no. 1, pp. 57–70, 2011.

[107] K. Toutouzas, Y. S. Chatzizisis, M. Riga, A. Giannopoulos, A. P. Antoniadis, S. Tu, Y. Fujino, D. Mitsouras, C. Doulaverakis, I. Tsampoulatidis, V. G. Koutkias, K. Bouki, Y. Li, I. Chouvarda, G. Cheimariotis, N. Maglaveras, I. Kompatsiaris, S. Nakamura, J. H. Reiber, F. Rybicki, H. Karvounis, C. Stefanadis, D. Tousoulis, and G. D. Giannoglou, “Accurate and reproducible reconstruction of coronary arteries and endothelial shear stress calculation using 3D OCT: Comparative study to 3D IVUS and 3D QCA,” *Atherosclerosis*, vol. 240, no. 2, pp. 510–519, 2015.

[108] A. Wahle, P. M. Prause, S. C. DeJong, and M. Sonka, “Geometrically correct 3-D reconstruction of intravascular ultrasound images by fusion with biplane angiography–methods and validation,” *IEEE Trans. Med. Imaging*, vol. 18, no. 8, pp. 686–699, 1999.

[109] S. Tu, G. Koning, W. Jukema, and J. H. C. Reiber, “Assessment of obstruction length and optimal viewing angle from biplane X-ray angiograms,” *Int. J. Cardiovasc. Imaging*, vol. 26, no. 1, pp. 5–17, 2010.

[110] C. V. Bourantas, F. G. Kalatzis, M. I. Papafaklis, D. I. Fotiadis, A. C. Tweddel, I. C. Kourtis, C. S. Katsouras, and L. K. Michalis, “ANGIOCARE: An automated system for fast three-dimensional coronary reconstruction by integrating angiographic and intracoronary ultrasound data,” *Catheter. Cardiovasc. Interv.*, vol. 72, no. 2, pp. 166–175, 2008.

[111] S. Tu, N. R. Holm, G. Koning, Z. Huang, and J. H. C. Reiber, “Fusion of 3D QCA and IVUS/OCT,” *Int. J. Cardiovasc. Imaging*, vol. 27, no. 2, pp. 197–207, 2011.

[112] C. Doulaverakis, I. Tsampoulatidis, A. P. Antoniadis, Y. S. Chatzizisis, A. Giannopoulos, I. Kompatsiaris, and G. D. Giannoglou, “IVUSAngio tool: a publicly available software for fast and accurate 3D reconstruction of coronary arteries,” *Comput. Biol. Med.*, vol. 43, no. 11, pp. 1793–803, 2013.

[113] E. Hansis, D. Schäfer, O. Dössel, and M. Grass, "Projection-based motion compensation for gated coronary artery reconstruction from rotational x-ray angiograms," *Phys. Med. Biol.*, vol. 53, no. 14, pp. 3807–3820, 2008.

[114] G. A. F. Schoonenberg, J. A. Garcia, and J. D. Carroll, "Left coronary artery thrombus characterized by a fully automatic three-dimensional gated reconstruction," *Catheter. Cardiovasc. Interv.*, vol. 74, no. 1, pp. 97–100, 2009.

[115] H. K. Tuy, "An Inversion Formula for Cone-Beam Reconstruction," *SIAM J. Appl. Math.*, vol. 43, no. 3, pp. pp. 546–552, 1983.

[116] B. D. Smith, "Image reconstruction from cone-beam projections: necessary and sufficient conditions and reconstruction methods," *IEEE Trans. Med. Imaging*, vol. 4, no. 1, pp. 14–25, 1985.

[117] L. A. Feldkamp, L. C. Davis, and J. W. Kress, "Practical cone-beam algorithm," *J. Opt. Soc. Am.*, vol. 1, no. 6, p. 612, 1984.

[118] J. Hsieh, B. Nett, Z. Yu, K. Sauer, J.-B. Thibault, and C. Bouman, "Recent advances in CT image reconstruction," *Curr. Radiol. Rep.*, vol. 1, no. 1, pp. 39–51, 2013.

[119] E. Hansis, H. Schomberg, K. Erhard, O. Dössel, and M. Grass, "Four-dimensional cardiac reconstruction from rotational x-ray sequences: first results for 4D coronary angiography," in *Proc. SPIE*, vol. 7258, 2009, pp. 72 580B–72 580B–11.

[120] C. Blondel, R. Vaillant, G. Malandain, and N. Ayache, "3D tomographic reconstruction of coronary arteries using a precomputed 4D motion field," *Phys. Med. Biol.*, vol. 49, no. 11, pp. 2197–2208, 2004.

[121] E. Hansis, D. Schäfer, O. Dössel, and M. Grass, "Evaluation of iterative sparse object reconstruction from few projections for 3-D rotational coronary angiography," *IEEE Trans. Med. Imaging*, vol. 27, no. 11, pp. 1548–1555, 2008.

[122] E. Hansis, O. Dossel, and M. Grass, "Motion-compensated iterative sparse data reconstruction for interventional 3-D coronary artery imaging," in *IEEE Nucl. Sci. Symp. Conf. Rec.*, 2008, pp. 4280–4284.

[123] J. Zhou, A. Bousse, G. Yang, J.-J. Bellanger, L. Luo, C. Toumoulin, and J.-L. Coatrieux, "A blob-based tomographic reconstruction of 3D coronary trees from rotational x-ray angiography," in *Proc. SPIE*, vol. 6913, 2008, pp. 69 132N–69 132N–12.

[124] Y. Hu, L. Xie, J. C. Nunes, J. J. Bellanger, M. Bedossa, and C. Toumoulin, "ECG gated tomographic reconstruction for 3-D rotational coronary angiography," in *Proc. IEEE Eng. Med. Biol. Soc.*, 2010, pp. 3614–3617.

[125] Y. Hu, M. Jung, A. Oukili, G. Yang, J.-C. Nunes, J. Fehrenbach, G. Peyre, M. Bedossa, L. Luo, C. Toumoulin, and L. D. Cohen, "Sparse reconstruction from a limited projection number of the coronary artery tree in X-ray rotational imaging," in *Proc. IEEE Int. Symp. Biomed. Imaging*, 2012, pp. 804–807.

[126] F. Xu and K. Mueller, "A comparative study of popular interpolation and integration methods for use in computed tomography," in *Proc. IEEE Int. Symp. Biomed. Imaging*, 2006, pp. 1252–1255.

[127] B. Movassaghi, M. Grass, D. Schaefer, V. Rasche, O. Wink, G. Schoonenberg, J. Y. Chen, J. A. Garcia, B. M. Groves, J. C. Messenger, and J. D. Carroll, "4D coronary artery reconstruction based on retrospectively gated rotational angiography: first in-human results," in *Proc. SPIE*, vol. 6509, 2007, pp. 65 090P–65 090P–6.

[128] C. Schwemmer, C. Rohkohl, G. Lauritsch, K. Müller, and J. Hornegger, "Opening windows - Increasing window size in motion-compensated ECG-gated cardiac vasculature reconstruction," in *Int. Meet. Fully Three-Dimensional Image Reconstr. Radiol. Nucl. Med.*, J. Qi and R. Leahy, Eds., 2013, pp. 50–53.

[129] M. Li, H. Yang, and H. Kudo, "An accurate iterative reconstruction algorithm for sparse objects: application to 3D blood vessel reconstruction from a limited number of projections," *Phys. Med. Biol.*, vol. 47, no. 15, pp. 2599–2609, 2002.

[130] M. Li, H. Kudo, J. Hu, and R. H. Johnson, "Improved iterative algorithm for sparse object reconstruction and its performance evaluation with micro-CT data," *IEEE Trans. Nucl. Sci.*, vol. 51, no. 3, pp. 659–666, 2004.

[131] B. Liu, F. Zhou, and X. Bai, "Improved C-arm cardiac cone beam CT based on alternate reconstruction and segmentation," *Biomed. Signal Process. Control*, vol. 13, pp. 113–122, 2014.

[132] H. Wu, C. Rohkohl, and J. Hornegger, "Total variation regularization method for 3D rotational coronary angiography," in *Proc. Bild. für die Medizin*, ser. Informatik aktuell, 2011, pp. 434–438.

[133] B. Movassaghi, V. Rasche, R. Florent, M. Viergever, and W. Niessen, "3D coronary reconstruction from calibrated motion-compensated 2D projections," in *Proc. Comput. Assist. Radiol. Surg.*, vol. 1256, 2003, pp. 1079–1084.

[134] C. Rohkohl, G. Lauritsch, M. Prümmer, J. Boese, and J. Hornegger, "Towards 4-D cardiac reconstruction without ECG and motion periodicity using C-arm CT," in *Int. Meet. Fully Three-Dimensional Image Reconstr. Radiol. Nucl. Med.*, 2009, pp. 323–326.

[135] C. Rohkohl, G. Lauritsch, L. Biller, M. Prümmer, J. Boese, and J. Hornegger, "Interventional 4D motion estimation and reconstruction of cardiac vasculature without motion periodicity assumption," *Med. Image Anal.*, vol. 14, no. 5, pp. 687–694, 2010.

[136] C. Rohkohl, G. Lauritsch, L. Biller, and J. Hornegger, "ECG-gated interventional cardiac reconstruction for non-periodic motion," in *Proc. Med. Image Comput. Comput. Assist. Interv.*, ser. LNCS, vol. 6361, 2010, pp. 151–158.

[137] E. Hansis, J. D. Carroll, D. Schäfer, O. Dössel, and M. Grass, "High-quality 3-D coronary artery imaging on an interventional C-arm x-ray system." *Med. Phys.*, vol. 37, no. 4, pp. 1601–9, 2010.

[138] H. Erdogan and J. A. Fessler, "Ordered subsets algorithms for transmission tomography," *Phys. Med. Biol.*, vol. 44, no. 11, pp. 2835–51, 1999.

[139] A. R. de Pierro and M. E. Beleza Yamagishi, "Fast EM-like methods for maximum "a posteriori" estimates in emission tomography," *IEEE Trans. Med. Imaging*, vol. 20, no. 4, pp. 280–8, 2001.

[140] P. Soille, *Morphological image analysis: principles and applications*, 2nd ed. Springer-Verlag New York, 2004.

[141] W. Holub, C. Rohkohl, D. Schuldhaus, M. Prümmer, G. Lauritsch, and J. Hornegger, "4D motion animation of coronary arteries from rotational angiography," in *Proc. SPIE*, vol. 7964, 2011, pp. 79 641S–79 641S–10.

[142] Radiology Support Devices, "Lung/chest phantom," 2006. [Online]. Available: http://rsdphantoms.com/rd_lung.htm

[143] C. Lorenz, J. von Berg, T. Bulow, S. Renisch, and S. Wergandt, "Modeling the coronary artery tree," in *Proc. Shape Model. Appl.*, 2004, pp. 354–399.

[144] J. T. Dodge, B. G. Brown, E. L. Bolson, and H. T. Dodge, "Lumen diameter of normal human coronary arteries. Influence of age, sex, anatomic variation, and left ventricular hypertrophy or dilation," *Circulation*, vol. 86, no. 1, pp. 232–246, 1992.

[145] G. Yang, A. Bousse, C. Toumoulin, and H. Shu, "Simulation environment for the evaluation of 3D coronary tree reconstruction algorithms in rotational angiography," *Proc. IEEE Eng. Med. Biol. Soc.*, pp. 4484–7, 2007.

[146] G. Yang, Y. Hu, X. Huang, H. Shu, and C. Toumoulin, "Simulation environment of X-ray rotational angiography using 3D+t coronary tree model," *Proc. IEEE Eng. Med. Biol. Soc.*, pp. 629–32, 2012.

[147] W. P. Segars, G. Sturgeon, S. Mendonca, J. Grimes, and B. M. W. Tsui, "4D XCAT phantom for multimodality imaging research," *Med. Phys.*, vol. 37, no. 9, pp. 4902–15, 2010.

[148] G. S. K. Fung, W. P. Segars, G. T. Gullberg, and B. M. W. Tsui, "Development of a model of the coronary arterial tree for the 4D XCAT phantom," *Phys. Med. Biol.*, vol. 56, no. 17, pp. 5651–63, 2011.

[149] C. Rohkohl, G. Lauritsch, A. Keil, and J. Hornegger, “CAVAREV–an open platform for evaluating 3D and 4D cardiac vasculature reconstruction,” *Phys. Med. Biol.*, vol. 55, no. 10, pp. 2905–15, 2010.

[150] C. Schwemmer, C. Forman, J. Wetzl, A. Maier, and J. Hornegger, “CoroEval: a multi-platform, multi-modality tool for the evaluation of 3D coronary vessel reconstructions,” *Phys. Med. Biol.*, vol. 59, no. 17, pp. 5163–5174, 2014.

[151] N. E. Green, S.-Y. J. Chen, A. R. Hansgen, J. C. Messenger, B. M. Groves, and J. D. Carroll, “Angiographic views used for percutaneous coronary interventions: A three-dimensional analysis of physician-determined vs. computer-generated views,” *Catheter. Cardiovasc. Interv.*, vol. 64, no. 4, pp. 451–459, 2005.

[152] V. Rasche, M. Mansour, V. Reddy, J. Singh, A. Qureshi, R. Manzke, S. Sokka, and J. Ruskin, “Fusion of three-dimensional X-ray angiography and three-dimensional echocardiography,” *Int. J. Comput. Assist. Radiol. Surg.*, vol. 2, no. 5, pp. 293–303, 2008.

[153] D. A. Langan, B. E. H. Claus, O. Al Assad, Y. Trousset, C. Riddell, G. Avignon, S. B. Solomon, H. Lai, and X. Wang, “Interventional C-arm tomosynthesis for vascular imaging: initial results,” in *Proc. SPIE*, vol. 9412, 2015, pp. 94 125N–94 125N–8.

[154] I. Larrabide, M. Kim, L. Augsburger, M. C. Villa-Uriol, D. Rüfenacht, and A. F. Frangi, “Fast virtual deployment of self-expandable stents: method and in vitro evaluation for intracranial aneurysmal stenting,” *Med. Image Anal.*, vol. 16, no. 3, pp. 721–30, 2012.

[155] F. M’hiri, L. Duong, C. Desrosiers, and M. Cheriet, “Vesselwalker: Coronary arteries segmentation using random walks and hessian-based vesselness filter,” in *Proc. IEEE Int. Symp. Biomed. Imaging*, 2013, pp. 918–921.

[156] P. Besl and N. D. McKay, “A method for registration of 3-D shapes,” *IEEE Trans. Pattern Anal. Mach. Intell.*, vol. 14, no. 2, pp. 239–256, 1992.

[157] H. Chui and A. Rangarajan, “A feature registration framework using mixture models,” in *IEEE Workshop MMBIA*, 2000, pp. 190–197.

[158] ——, “A new point matching algorithm for non-rigid registration,” *Comput. Vis. Image Underst.*, vol. 89, no. 2, pp. 114–141, 2003.

[159] A. Myronenko and Xubo Song, “Point set registration: Coherent point drift,” *IEEE Trans. Pattern Anal. Mach. Intell.*, vol. 32, no. 12, pp. 2262–2275, 2010.

[160] A. L. Yuille and N. M. Grzywacz, “A mathematical analysis of the motion coherence theory,” *Int. J. Comput. Vis.*, vol. 3, no. 2, pp. 155–175, 1989.

[161] R. Horaud, F. Forbes, M. Yguel, G. Dewaele, and Jian Zhang, “Rigid and Articulated Point Registration with Expectation Conditional Maximization,” *IEEE Trans. Pattern Anal. Mach. Intell.*, vol. 33, no. 3, pp. 587–602, 2011.

[162] Bing Jian and B. C. Vemuri, “Robust point set registration using Gaussian mixture models,” *IEEE Trans. Pattern Anal. Mach. Intell.*, vol. 33, no. 8, pp. 1633–1645, 2011.

[163] T. Chen, B. C. Vemuri, A. Rangarajan, and S. J. Eisenschenk, “Group-Wise Point-Set Registration Using a Novel CDF-Based Havrda-Charv{á}t Divergence,” *Int. J. Comput. Vis.*, vol. 86, no. 1, p. 111, 2009.

[164] N. J. Tustison, S. P. Awate, Gang Song, T. S. Cook, and J. C. Gee, “Point Set Registration Using HavrdaCharvatTsallis Entropy Measures,” *IEEE Trans. Med. Imaging*, vol. 30, no. 2, pp. 451–460, 2011.

[165] C. M. Bishop, *Pattern recognition and machine learning.* Secaucus, NJ, USA: Springer-Verlag New York, Inc., 2006.

[166] G. Wang, Z. Wang, Y. Chen, and W. Zhao, “A robust non-rigid point set registration method based on asymmetric gaussian representation,” *Comput. Vis. Image Underst.*, vol. 141, pp. 67–80, 2015.

[167] N. Ravikumar, A. Gooya, S. Çimen, A. F. Frangi, and Z. A. Taylor, “A multi-resolution t-mixture model approach to robust group-wise alignment of shapes,” in *Proc. Med. Image Comput. Comput. Assist. Interv.*, S. Ourselin, L. Joskowicz, M. R. Sabuncu, G. Unal, and W. Wells, Eds., vol. 9902, 2016, pp. 142–149.

[168] H. Hufnagel, X. Pennec, J. Ehrhardt, N. Ayache, and H. Handels, "Generation of a statistical shape model with probabilistic point correspondences and the expectation maximization- iterative closest point algorithm," *Int. J. Comput. Assist. Radiol. Surg.*, vol. 2, no. 5, pp. 265–273, 2008.

[169] A. Gooya, C. Davatzikos, and A. F. Frangi, "A Bayesian approach to sparse model selection in statistical shape models," *SIAM J. Imaging Sci.*, vol. 8, no. 2, pp. 858–887, 2015.

[170] A. Rasoulian, R. Rohling, and P. Abolmaesumi, "Group-Wise Registration of Point Sets for Statistical Shape Models," *IEEE Trans. Med. Imaging*, vol. 31, no. 11, pp. 2025–2034, 2012.

[171] N. Baka, B. P. F. Lelieveldt, C. Schultz, W. Niessen, and T. van Walsum, "Respiratory motion estimation in x-ray angiography for improved guidance during coronary interventions," *Phys. Med. Biol.*, vol. 60, no. 9, pp. 3617–3637, 2015.

[172] A. P. Dempster, N. M. Laird, and D. B. Rubin, "Maximum likelihood from incomplete data via the EM algorithm," *J. R. Stat. Soc. Ser. B*, vol. 39, no. 1, pp. 1–38, 1977.

[173] F. Benmansour, E. Türetken, and P. Fua, "Tubular Geodesics using Oriented Flux: An ITK Implementation," *Insight Journal*, no. Online, 2013. [Online]. Available: http://hdl.handle.net/10380/3398

[174] R. E. Tarjan, "Finding optimum branchings," *Networks*, vol. 7, no. 1, pp. 25–35, 1977.

[175] M. Grech, J. Debono, R. G. Xuereb, A. Fenech, and V. Grech, "A comparison between dual axis rotational coronary angiography and conventional coronary angiography," *Catheter. Cardiovasc. Interv.*, vol. 80, no. 4, pp. 576–580, 2012.

[176] J. Montagnat and H. Delingette, "4D deformable models with temporal constraints: application to 4D cardiac image segmentation," *Med. Image Anal.*, vol. 9, no. 1, pp. 87–100, 2005.

[177] D. Perperidis, R. H. Mohiaddin, and D. Rueckert, "Spatio-temporal free-form registration of cardiac MR image sequences," *Med. Image Anal.*, vol. 9, no. 5, pp. 441–56, 2005.

[178] C. Hoogendoorn, F. Sukno, S. Ordás, and A. Frangi, "Bilinear models for spatio-temporal point distribution analysis," *Int. J. Comput. Vis.*, vol. 85, no. 3, pp. 237–252, 2009.

[179] J. B. Tenenbaum and W. T. Freeman, "Separating style and content with bilinear models," *Neural Comput.*, vol. 12, no. 6, pp. 1247–1283, 2000.

[180] C. Hoogendoorn, N. Duchateau, D. Sánchez-Quintana, T. Whitmarsh, F. M. Sukno, M. De Craene, K. Lekadir, and A. F. Frangi, "A high-resolution atlas and statistical model of the human heart from multislice CT," *IEEE Trans. Med. Imaging*, vol. 32, no. 1, pp. 28–44, 2013.

[181] B. W. Silverman, *Density estimation for statistics and data analysis.* CRC Press, 1986.

[182] M. Groher, D. Zikic, and N. Navab, "Deformable 2D-3D registration of vascular structures in a one view scenario," *IEEE Trans. Med. Imaging*, vol. 28, no. 6, pp. 847–60, 2009.

[183] C. Goodall, "Procrustes methods in the statistical analysis of shape," *J. R. Stat. Soc. Ser. B*, vol. 53, no. 2, pp. pp. 285–339, 1991.

[184] I. Akhter, T. Simon, S. Khan, I. Matthews, and Y. Sheikh, "Bilinear spatiotemporal basis models," *ACM Trans. Graph.*, vol. 31, no. 2, pp. 1–12, 2012.

[185] N. Townsend, M. Nichols, P. Scarborough, and M. Rayner, "Cardiovascular disease in Europe epidemiological update 2015," *Eur. Heart J.*, vol. 36, no. 40, pp. 2696–2705, 2015.

[186] D. Mozaffarian, E. J. Benjamin, A. S. Go, D. K. Arnett, M. J. Blaha, M. Cushman, S. de Ferranti, J.-P. Després, H. J. Fullerton, V. J. Howard, M. D. Huffman, S. E. Judd, B. M. Kissela, D. T. Lackland, J. H. Lichtman, L. D. Lisabeth, S. Liu, R. H. Mackey, D. B. Matchar, D. K. McGuire, E. R. Mohler, C. S. Moy, P. Muntner, M. E. Mussolino, K. Nasir, R. W. Neumar,

G. Nichol, L. Palaniappan, D. K. Pandey, M. J. Reeves, C. J. Rodriguez, P. D. Sorlie, J. Stein, A. Towfighi, T. N. Turan, S. S. Virani, J. Z. Willey, D. Woo, R. W. Yeh, and M. B. Turner, "Heart disease and stroke statistics-2015 update: A report from the American Heart Association," *Circulation*, vol. 131, no. 4, pp. e29–322, 2014.

[187] S. Çimen, A. Gooya, M. Grass, and A. F. Frangi, "Reconstruction of coronary arteries from X-ray angiography: A review," *Med. Image Anal.*, vol. 32, pp. 46–68, 2016.

[188] A. F. Frangi, W. J. Niessen, K. L. Vincken, and M. A. Viergever, "Multiscale vessel enhancement filtering," in *Proc. Med. Image Comput. Comput. Assist. Interv.*, ser. LNCS, W. M. Wells, A. Colchester, and S. Delp, Eds., vol. 1496, 1998, pp. 130–137.

[189] M. W. K. Law and A. C. S. Chung, "Three dimensional curvilinear structure detection using optimally oriented flux," in *Proc. Eur. Conf. Comput. Vis.*, 2008, pp. 368–382.

[190] Z. Hui and M. Friedman, "Tracking 3-D coronary artery motion with biplane angiography," in *Proc. IEEE Int. Symp. Biomed. Imaging*, 2002, pp. 605–608.

[191] S. Çimen, A. Gooya, and A. F. Frangi, "Reconstruction of Coronary Artery Centrelines from X-ray Rotational Angiography using a Probabilistic Mixture Model," in *Proc. SPIE*, vol. 9784, 2016, pp. 97 843A–97 843A–7.

[192] S. Çimen, A. Gooya, N. Ravikumar, Z. A. Taylor, and A. F. Frangi, "Reconstruction of coronary artery centrelines from X-Ray angiography using a mixture of Student's t-distributions," in *Proc. Med. Image Comput. Comput. Assist. Interv.*, S. Ourselin, L. Joskowicz, M. R. Sabuncu, G. Unal, and W. Wells, Eds., vol. 9902, 2016, pp. 291–299.

[193] M. Schneider and H. Sundar, "Automatic global vessel segmentation and catheter removal using local geometry information and vector field integration," in *Proc. IEEE Int. Symp. Biomed. Imaging*, 2010, pp. 45–48.

[194] M. Svensén and C. M. Bishop, "Robust Bayesian mixture modelling," *Neurocomputing*, vol. 64, pp. 235–252, 2005.

[195] C. Liu and D. B. Rubin, “ML estimation of the t distribution using EM and its extensions, ECM and ECME,” *Stat. Sin.*, vol. 5, no. 1, pp. 19–39, 1995.

[196] S. S. Keerthi and E. G. Gilbert, “Convergence of a generalized SMO algorithm for SVM classifier design,” *Mach. Learn.*, vol. 46, no. 1, pp. 351–360, 2002.

[197] X. L. Meng and D. B. Rubin, “Maximum likelihood estimation via the ECM algorithm: A general framework,” *Biometrika*, vol. 80, no. 2, pp. 267–278, 1993.

[198] D. Peel and G. J. McLachlan, “Robust mixture modelling using the t distribution,” *Stat. Comput.*, vol. 10, no. 4, pp. 339–348, 2000.

[199] J. Weickert, “Coherence-enhancing diffusion filtering,” *Int. J. Comput. Vis.*, vol. 31, no. 2, pp. 111–127, 1999.

[200] A. Feragen, P. Lo, M. de Bruijne, M. Nielsen, and F. Lauze, “Toward a theory of statistical tree-shape analysis,” *IEEE Trans. Pattern Anal. Mach. Intell.*, vol. 35, no. 8, pp. 2008–2021, 2013.

[201] M. A. Gülsün, G. Funka-Lea, Y. Zheng, and M. Eckert, “CTA coronary labeling through efficient geodesics between trees using anatomy priors,” in *Proc. Med. Image Comput. Comput. Assist. Interv.*, P. Golland, N. Hata, C. Barillot, J. Hornegger, and R. Howe, Eds., Cham, 2014, pp. 521–528.

[202] I. D. Gebru, X. Alameda-Pineda, F. Forbes, and R. Horaud, “EM Algorithms for Weighted-Data Clustering with Application to Audio-Visual Scene Analysis,” *arXiv*, 2015.

[203] H. S. Park, T. Shiratori, I. Matthews, and Y. Sheikh, “3D trajectory reconstruction under perspective projection,” *Int. J. Comput. Vis.*, vol. 115, no. 2, pp. 115–135, 2015.

[204] I. Akhter, Y. Sheikh, S. Khan, and T. Kanade, “Trajectory space: A dual representation for nonrigid structure from motion,” *IEEE Trans. Pattern Anal. Mach. Intell.*, vol. 33, no. 7, pp. 1442–1456, 2011.